On the Sigma-Model Structure of Type IIA Supergravity Action in Doubled Field Approach[¶]

A. J. Nurmagambetov

Akhiezer Institute for Theoretical Physics, NSC Kharkov Institute of Physics and Technology, Kharkov, 61108 Ukraine
e-mail: ajn@kipt.kharkov.ua
Received December 9, 2003; in final form, January 16, 2004

In this letter, we describe how to string together the doubled field approach by Cremmer, Julia, Lü, and Pope with the Pasti–Sorokin–Tonin technique to construct the sigma-model-like action for type IIA supergravity. The relation of the results with those obtained in the context of searching for superstring/M-theory hidden symmetry group is discussed. © 2004 MAIK "Nauka/Interperiodica".

PACS numbers: 04.65.+e; 04.50.+h; 11.25.Yb; 11.25.Mj

The essential step towards making phenomenological sense of a higher-dimensional theory is to find the relevant scheme of reducing the extra dimensions and of confining the Standard Model fields on a four-dimensional spacetime submanifold. The idea of viewing this submanifold as a three-brane embedded into a five-dimensional space [1] has been proved to be useful in searching for the solution to some longstanding problems of phenomenology like the hierarchy problem and the value of cosmological constant. To shed some light on the stringy origin of this brane-world picture [2], one needs to deal with a domain wall coupling to ten-dimensional bulk fields that enter the low-energy effective action of a superstring theory. Constructing such a coupling, one should have in mind that, as a superbrane, the domain wall is the source of antisymmetric tensor field of supergravity multiplet and, as the higher brane with the dimension of worldvolume greater than five, it couples to the conventional supergravity tensor fields as well as to their duals. Moreover, the requirement of quantum consistency of a theory forces one to take into account other higher branes as a latent source of new local anomalies. Hence, coupling the higher branes to higher-dimensional maximal supergravity backgrounds and studying the issue of anomaly cancellations deserve to have a formulation for supergravities whose dynamics is managed by the standard and the dual fields entering the theory in a duality-symmetric way.

Another problem that is important from the phenomenological point of view is to identify the underlying symmetry group of superstring/M theory in which the Standard Model group have to be embedded. Recently, it was emphasized that the duality-symmetric structure of maximal supergravities becomes important in searching for such a hidden symmetry group [3–10].

There are different routes to recover duality-symmetric structure. For instance, one can be purely interested in dynamics of different subsectors of duality-symmetric theory doubling the fields on-shell, i.e., at the level of fields' equations of motion [11]. After the doubling, applying a method akin to the nonlinear realization technique, one can find an elegant representation of the scalars' and antisymmetric tensors' duality relations and equations of motion in the form of a twisted self-duality condition and zero-curvature condition. Or one can construct a supersymmetric pseudo-action [2] supported by on-shell duality relations between the doubled fields, and these relations have to be imposed by hand. There also is universal formulation, which is off-shell and produces the duality relations as equations of motion [12–15]. This formulation is based on the ground of the PST technique [16]. But neither the pseudoaction approach nor PST formalism, which are just the extensions of standard supergravity actions, say anything about the hidden symmetry structure of maximal supergravities. On the contrary, the doubled field approach of [11] is a higher-dimensional remnant of G/H coset structure of scalar group manifolds that appear after toroidal reduction of $D = 11$ supergravity with subsequent dualization of the higher rank tensor fields [17]. In general, the group of invariance of equations of motion is more restrictive than the group of invariance of the action. Therefore, the step toward recovering the true hidden symmetry group of superstring/M theory is the construction of relevant low-energy effective actions. Since the dynamics of scalars mentioned so far is described by G/H sigma-model action, one can also expect the sigma-model-like structure of the doubled field action.

As a by-product of studies performed in [15], the doubled field formalism of [11] dealing with the non-gravitational subsector of $D = 11$ supergravity has been extended to the off-shell supersymmetric formulation

---

[¶] This article was submitted by the author in English.

of duality-symmetric $D = 11$ supergravity [12]. It has also been claimed that the sigma-model-like structure of the doubled gauge field action in $D = 11$ has a generic form that remains the same also for the doubled field formulations of type IIA and type IIB supergravities, as well as for lower-dimensional maximal supergravities considered in [11]. This point roughly seems to be clear, at least for the sequence of maximal supergravities coming from $D = 11$ supergravity, since all of them are related to each other via dimensional reduction. However, there is no rigorously defined procedure of dimensional reduction for the sigma-model-like action. And having the duality-symmetric gauge field structure in $D = 11$ is not enough to recover complete duality-symmetric structure of $D = 10$ type IIA supergravity, since one shall double the fields coming from the reduction of gravity sector. Hence, the explicit supersymmetric sigma-model structure of low-dimensional maximal supergravities has to be shown in a case-by-case manner. The aim of the present paper is to fill the gap for type IIA supergravity and to demonstrate how the generic form of the $D = 11$ doubled field sigma-model action [15] is accommodated to describe its ten-dimensional counterpart.

Let us get started with recalling in brief the doubled field formulation of $D = 11$ supergravity [11] and its extension at the level of proper action [15]. From the Lagrangian of $D = 11$ supergravity [18] (see [15] for a comprehensive list of our conventions),

$$\mathscr{L} = -\sqrt{g}R + \frac{i}{3!}\overline{\Psi} \wedge D\left[\frac{1}{2}(\omega + \overline{\omega})\right]\Psi\Gamma^{abc} \wedge \Sigma_{abc}$$

$$-\frac{1}{48}\sqrt{g}F_{mnpq}F^{mnpq} - \frac{1}{6}A^{(3)} \wedge F^{(4)} \wedge F^{(4)} \qquad (1)$$

$$-\frac{1}{2}(C^{(7)} + *C^{(4)}) \wedge (F^{(4)} + (F^{(4)} - C^{(4)})),$$

with $F^{(4)} = dA^{(3)}$, $C^{(4)} = -1/4\overline{\Psi} \wedge \Gamma^{(2)} \wedge \Psi$, $C^{(7)} = i/4\overline{\Psi} \wedge \Gamma^{(5)} \wedge \Psi$, $\Gamma^{(n)} = 1/n! dx^{m_n} \wedge \cdots \wedge dx^{m_1}\Gamma^{(n)}_{m_1...m_n}$, we get the second-order equation of motion for the $A^{(3)}$ gauge field

$$d\left(*(F^{(4)} - C^{(4)}) - \frac{1}{2}A^{(3)} \wedge F^{(4)} - C^{(7)}\right) = 0 \qquad (2)$$

that can be presented as the Bianchi identity for the dual field $A^{(6)}$:

$$dF^{(7)} = \frac{1}{2}F^{(4)} \wedge F^{(4)}, \quad F^{(7)} = dA^{(6)} + \frac{1}{2}A^{(3)} \wedge F^{(4)}. \quad (3)$$

Now, forget for a while the dynamical origin of $F^{(7)} = dA^{(6)} + \frac{1}{2}A^{(3)} \wedge F^{(4)}$ and introduce it as an indepen-

dent partner of $F^{(4)}$. These field strengths are invariant under the local gauge transformations

$$\delta A^{(3)} = \Lambda^{(3)}, \quad \delta A^{(6)} = \Lambda^{(6)} - \frac{1}{2}\Lambda^{(3)} \wedge A^{(3)} \qquad (4)$$

with closed forms $\Lambda^{(3)}$, $\Lambda^{(6)}$ associated with the so-called large gauge transformations [19]. Because of the presence of "bare" $A^{(3)}$ in $F^{(7)}$ and, therefore, in $\delta A^{(6)}$ that is traced back to the presence of the Chern–Simons term in the Lagrangian (3), the large gauge transformations are non-Abelian:

$$[\delta_{\Lambda_1^{(3)}}, \delta_{\Lambda_2^{(3)}}] = \delta_{\Lambda^{(6)}}, \quad [\delta_{\Lambda^{(3)}}, \delta_{\Lambda^{(6)}}] = [\delta_{\Lambda_1^{(6)}}, \delta_{\Lambda_2^{(6)}}] = 0. (5)$$

These relations can be associated with a superalgebra generated by a "Grassmann-odd" generator t_3 and a commuting generator t_6

$$\{t_3, t_3\} = -t_6, \quad [t_3, t_6] = [t_6, t_6] = 0 \qquad (6)$$

after that one can realize an element of the supergroup

$$\mathscr{A} = e^{t_3 A^{(3)}} e^{t_6 A^{(6)}} \qquad (7)$$

and introduce the Cartan form

$$\mathscr{G} = d\mathscr{A}\mathscr{A}^{-1} = F^{(4)}t_3 + F^{(7)}t_6, \qquad (8)$$

which by definition satisfies the Maurer–Cartan equation, sometimes called the zero-curvature condition,

$$d\mathscr{G} + \mathscr{G} \wedge \mathscr{G} = 0. \qquad (9)$$

To impose the duality relation between *a priori* independent field strengths and arriving therefore at the standard number of degrees of freedom, one introduces the pseudoinvolution operator $\mathscr{S}$ which interchanges the generators t_3 and t_6:

$$\mathscr{S}t_3 = t_6, \quad \mathscr{S}t_6 = t_3, \quad \mathscr{S}^2 = 1. \qquad (10)$$

Using $\mathscr{S}$ and the Hodge operator, one can immediately check that the condition

$$*(\mathscr{G} + \mathscr{C}) = \mathscr{S}(\mathscr{G} + \mathscr{C}), \qquad (11)$$

where we have introduced the superalgebra valued element $\mathscr{C} = -C^{(4)}t_3 + C^{(7)}t_6$, correctly reproduces the duality relations between the field strengths and, therefore, reduces the tensors' degrees of freedom to the correct number. Moreover, when this condition holds, the Maurer–Cartan equation amounts to second-order equations of motion for $F^{(4)}$ and $F^{(7)}$.

Applying the PST technique, the twisted self-duality condition is reproduced from the following action [15]:

$$S = S_{EH} + S_\Psi - Tr \int_{\mathscr{M}^{11}} \left[\frac{1}{4}*\mathscr{G} \wedge \mathscr{G}\right.$$

$$+ \frac{1}{2}\left(\mathcal{G} + \frac{1}{2}\mathcal{C}\right) \wedge (\mathcal{S} - *)\mathcal{C} - \frac{1}{12}\mathcal{G} \wedge \mathcal{S}\mathcal{G} \tag{12}$$

$$- \frac{1}{4}*i_v(\mathcal{S} - *)\mathcal{G} \wedge i_v(\mathcal{S} - *)\mathcal{G}\Big],$$

where S_{EH} and S_Ψ stand for the Einstein–Hilbert and the Rarita–Schwinger actions and

$$v = \frac{da(x)}{\sqrt{-(\partial a)^2}} \tag{13}$$

is the one-form constructed out the PST scalar auxiliary field (cf. [16]) which ensures the covariance of the action and

$$\mathrm{Tr}(t_3 t_3) = -\mathrm{Tr}(t_6 t_6) = -1, \quad \mathrm{Tr}(t_3 t_6) = 0. \tag{14}$$

As usual, we have denoted by i_v the inner product of the vector field v_m with a form.

It is an instructive exercise to rewrite the sigma-model action (12) to the standard for $D = 11$ supergravity form. After some manipulations taking into account the definitions of $\mathcal{G}$ and S, one can arrive at

$$S = S_{CJS} + \int_{\mathcal{M}^{11}} \frac{1}{2} i_v \mathcal{F}^{(4)} \wedge *i_v \mathcal{F}^{(4)} \tag{15}$$

with S_{CJS} being the standard action by Cremmer, Julia, and Scherk [18] and $\mathcal{F}^{(4)} = (F^{(4)} - C^{(4)}) - *(F^{(7)} + C^{(7)})$. This is the action for the duality-symmetric $D = 11$ supergravity [12] from which one can dynamically derive the duality condition $\mathcal{F}^{(4)} = 0$. Apparently, on the shell of the duality condition $\mathcal{F}^{(4)} = 0$, action (15) coincides with the Cremmer–Julia–Scherk action.

Let us now turn to the type IIA supergravity, which can be obtained from $D = 11$ supergravity by dimensional reduction. The corresponding Lagrangian has the following form [20–22]:

$$\mathcal{L} = -\sqrt{-g}R - \frac{i}{3!}\overline{\psi} \wedge D\Big[\frac{1}{2}(\omega + \overline{\omega})\Big]\psi \wedge \Gamma^{abc}\Sigma_{abc}$$

$$- \frac{i}{2}\overline{\lambda}\Gamma^a D\Big[\frac{1}{2}(\omega + \overline{\omega})\Big]\lambda \wedge \Sigma_a$$

$$+ (-)^{n+1} \sum_{n=1}^{4} \Big[\frac{1}{2}e^{(-)^{n+1}\theta(n-1)\frac{(5-n)}{2}\phi} F^{(n)} \wedge *F^{(n)} \tag{16}$$

$$+ (-)^n\Big(C^{(10-n)} - e^{(-)^{n+1}\theta(n-1)\frac{(5-n)}{2}\phi} *C^{(n)}\Big)$$

$$\times \wedge\Big(F^{(n)} - \frac{1}{2}C^{(n)}\Big)\Big] + \frac{1}{2}B^{(2)} \wedge dA^{(3)} \wedge dA^{(3)} + \mathcal{O}(f^4).$$

Here, we have denoted $F^{(1)} = d\phi$; $F^{(3)} = dB^{(2)}$ is the field strength of the NS 2-form field $B^{(2)}$ and the RR field strengths are defined as

$$\mathbf{F} = d\mathbf{A} - F^{(3)} \wedge \mathbf{A} \tag{17}$$

considering the formal sum $\mathbf{A} = \sum_{n=0}^{3} A^{(2n+1)}$ and extracting the relevant combinations. θ stands for the usual step function taking the one in the case of a positive argument. The last term of (16) denotes the quartic fermion terms, which are not involved in the gravitino, dilaton, dilatino, and antisymmetric tensor gauge fields supercovariantization. The explicit form of the fermion bilinears $C^{(n)}$ can be read off [15].

Extracting the dual field strengths by use of equations of motion, one arrives at

$$F^{(7)} = dB^{(6)} - A^{(1)}F^{(6)} + \frac{1}{2}A^{(3)}dA^{(3)},$$

$$F^{(9)} = dA^{(8)} - \frac{3}{4}F^{(8)}A^{(1)} + \frac{1}{2}B^{(2)}dB^{(6)} - \frac{1}{4}F^{(6)}A^{(3)}, \tag{18}$$

while the RR field strengths $F^{(6)}$ and $F^{(8)}$ are defined as in (17).

Instead of repeating the analysis of large gauge transformations, constructing the associated superalgebra and introducing the Cartan form via nonlinear realization of the supergroup element as it has been done before, we will proceed further in a slightly different way.

Following [11], close inspection of the Bianchi identities for the dual field strengths shows that they can be obtained from the zero-curvature condition for the Cartan form

$$\mathcal{G} = \frac{1}{2}d\phi t_0 + \sum_{n=2}^{4} e^{(-)^{n+1}\frac{(5-n)}{4}\phi} F^{(n)} t_{n-1}$$

$$- \sum_{n=6}^{8} e^{(-)^{n+1}\frac{(5-n)}{4}\phi} F^{(n)} t_{n-1} - \frac{1}{2}F^{(9)} t_8,$$

taking into account the following superalgebra of generators:

$$[t_0, t_1] = \frac{3}{2}t_1, \quad [t_0, t_2] = -t_2, \quad [t_0, t_3] = \frac{1}{2}t_3,$$

$$[t_0, t_5] = -\frac{1}{2}t_5, \quad [t_0, t_6] = t_6, \quad [t_0, t_7] = -\frac{3}{2}t_7;$$

$$[t_1, t_2] = -t_3, \quad \{t_1, t_5\} = t_6, \quad [t_2, t_3] = t_5, \tag{19}$$

$$[t_2, t_5] = -t_7, \quad \{t_3, t_3\} = t_6, \quad \{t_1, t_7\} = \frac{3}{8}t_8,$$

$$[t_2, t_6] = \frac{1}{4}t_8, \quad \{t_3, t_5\} = \frac{1}{8}t_8.$$

Loosely speaking, most of the superalgebra can be recovered by extraction of the relevant Bianchi identities for dual field strengths from zero-curvature condition (11). The rest of the algebra is restored from the graded Jacobi identities. Since we have required the zero-curvature condition, we can always present the Cartan form as $\mathscr{G} = d\mathscr{A}\mathscr{A}^{-1}$ for the supergroup element $\mathscr{A}$, the explicit expression for which can be read off [11].

To present the type IIA supergravity action in a sigma-model-like form, one needs to write the former in the generating for such a representation following expression

$$S = S_{EH} + S_\psi + S_\lambda$$

$$+ (-)^{n+1} \int\limits_{\mathcal{M}^{10}} \sum_{n=1}^{4} \left[\frac{1}{4} e^{(-)^{n+1}\theta(n-1)\frac{(5-n)}{2}\phi} F^{(n)} \wedge *F^{(n)} \right.$$

$$+ \frac{(-)^n}{2} \left(C^{(10-n)} - e^{(-)^{n+1}\theta(n-1)\frac{(5-n)}{2}\phi} *C^{(n)} \right)$$

$$\left. \times \wedge \left(F^{(n)} - \frac{1}{2}C^{(n)} \right) \right]$$

$$+ \int\limits_{\mathcal{M}^{10}} \sum_{n=6}^{9} \left[\frac{1}{4} e^{(-)^{n+1}\theta(9-n)\frac{(5-n)}{2}\phi} F^{(n)} \wedge *F^{(n)} \right.$$

$$+ \frac{(-)^{n+1}}{2} \left(C^{(10-n)} - e^{(-)^{n+1}\theta(9-n)\frac{(5-n)}{2}\phi} *C^{(n)} \right)$$

$$\left. \times \wedge \left(F^{(n)} + \frac{1}{2}C^{(n)} \right) \right]$$

$$+ (-)^{n+1} \int\limits_{\mathcal{M}^{10}} \frac{1}{4} \sum_{n=1}^{4} e^{(-)^{n+1}\theta(n-1)\frac{(5-n)}{2}\phi} i_v \mathscr{F}^{(n)} \wedge *i_v \mathscr{F}^{(n)}$$

$$- \int\limits_{\mathcal{M}^{10}} \frac{1}{4} \sum_{n=6}^{4} e^{(-)^{n+1}\theta(9-n)\frac{(5-n)}{2}\phi} i_v \mathscr{F}^{(n)} \wedge *i_v \mathscr{F}^{(n)}$$

$$+ \frac{1}{2} \int\limits_{\mathcal{M}^{10}} \sum_{n=1}^{4} \frac{1}{3^{\left[\frac{n+1}{4}\right]}} F^{(10-n)} \wedge F^{(n)} + \mathbb{O}(f^4), \tag{20}$$

where S_{EH}, S_ψ, and S_λ stand for the kinetic terms of graviton, gravitino, and dilatino, and $[(n+1)/4]$ denotes the integer part of the number $(n+1)/4$. Here, we have denoted by $\mathscr{F}^{(n)}$ the duality relations between the fields and their dual partners:

$$\mathscr{F}^{(n)} = \hat{F}^{(n)} + e^{(-)^n\theta(n-1)\theta(9-n)\frac{(5-n)}{2}\phi} *\hat{F}^{10-n}, \tag{21}$$

$$n = 1, \ldots, 4, 6, \ldots, 9,$$

with $\hat{F}^{(n)} = F^{(n)} - C^{(n)}$ for $n < 5$ and $\hat{F}^{(n)} = F^{(n)} + C^{(n)}$ for $n > 5$.

Defining the traces between the same generators as

$$\text{Tr}(t_0 t_0) = -\text{Tr}(t_8 t_8) = -4, \quad \text{Tr}(t_1 t_1) = \text{Tr}(t_7 t_7) = -1,$$
$$\text{Tr}(t_2 t_2) = -\text{Tr}(t_6 t_6) = -1, \quad \text{Tr}(t_3 t_3) = \text{Tr}(t_5 t_5) = -1, \tag{22}$$

and setting other traces to zero, it is a matter to check that Eq. (20) is presented as

$$S = S_{EH} + S_\psi + S_\lambda$$

$$- \text{Tr} \int\limits_{\mathcal{M}^{10}} \left[(-)^{\theta(5-n)} \left\{ \frac{1}{2} *\mathscr{G} \wedge \mathscr{G} - \frac{1}{2}(\mathscr{S} - *)\mathscr{C} \wedge \left(\mathscr{G} + \frac{1}{2}\mathscr{C} \right) \right\} \right.$$

$$\left. - \frac{1}{4} *i_v(\mathscr{S} - *)\mathscr{G} \wedge i_v(\mathscr{S} - *)\mathscr{G} \right] \tag{23}$$

$$- \frac{1}{4}\text{Tr} \int\limits_{\mathcal{M}^{10}} \frac{1}{3^{\left[\frac{\min(n,h)+1}{4}\right]}} (-)^n \mathscr{G} \wedge \mathscr{S}\mathscr{G} + \mathbb{O}(f^4).$$

The presence of the coefficient with the theta function in front of the second integral over a ten-dimensional manifold which, after evaluating the traces from (22), becomes proportional in particular to the sum of $F^{(n)} \wedge *F^{(n)}$ manages the sign flips in the dilaton and gauge fields' kinetic terms, and the coefficient in the last term of (23) gives the correct signs and coefficients to obtain the last term of (20). To recover the structure of the supercovariant terms for the $F^{(n)}$s, we have introduced the superalgebra valued element

$$\mathscr{C} = -\frac{1}{2}C^{(1)}t_0 - \sum_{n=2}^{4} e^{(-)^{n+1}\frac{(5-n)}{4}\phi} C^{(n)}t_{n-1}$$

$$- \sum_{n=6}^{8} e^{(-)^{n+1}\frac{(5-n)}{4}\phi} C^{(n)}t_{n-1} - \frac{1}{2}C^{(9)}t_8.$$

The twisted self-duality condition

$$*(\mathscr{G} + \mathscr{C}) = \mathscr{S}(\mathscr{G} + \mathscr{C}) \tag{24}$$

with the pseudoinvolution $\mathscr{S}$ exchanging the generators

$$\mathscr{S}t_n = t_{8-n}, \quad n = 0, \ldots, 3, 5, \ldots, 8; \quad \mathscr{S}^2 = 1 \tag{25}$$

is reproduced from action (23) as an equation of motion. As soon as Eq. (24) holds, the zero-curvature condition encodes the second-order equations of motion for fields and their duals.

Therefore, we have found the explicit form of the sigma-model representation of the type IIA duality-symmetric supergravity action and have demonstrated that the form of this representation obtained previously for the $D = 11$ duality-symmetric supergravity [15] is generic and needs just slight modifications to accom-

modate the structure of type IIA supergravity. The main difference between eleven- and ten-dimensional cases is the structure of quartic fermion terms. In the former case, the terms of this type can be absorbed into the corresponding supercovariant quantities, while in the latter case, there are additional quartic fermion terms which do not involve into the supercovariantization (cf. [20–22]).

In conclusion, let us discuss the relation of the results with those obtained in the context of searching for the superstring/M-theory hidden symmetry group [4–10]. It was realized long ago [3] that the global symmetry groups of toroidally compacted up to four spacetime dimensions $D = 11$ supergravity fall into the class of exceptional groups E_n with $n \leq 7$. Discovering the exceptional geometry of $D = 3$ maximal supergravity [8] gave more evidence in favor of previously conjectured [10] (and references therein), [5] E_{10} hidden symmetry group of "small tension limit" of M theory [9] compacting to one dimension. Recently, it was demonstrated that the bosonic sector of $D = 11$ supergravity can be reformulated as a nonlinear realization of E_{11}/F_{11} coset space with maximal noncompact group F_{11} containing $SO(1, 10)$ as a subgroup [6]. To realize such a formulation and to require that representatives of such a coset space belong to the Borel subgroup of E_{11}, one is forced to involve dual partners for graviton and 3-index antisymmetric tensor gauge field from the beginning, and the action obtained is expected that of a sigma-model. Additional strong arguments in favor of the E_{11} M-theory hidden symmetry group conjecture [6] follow from careful analysis of group structure relevant to realize nonlinearly the bosonic sector of type IIA supergravity. The approach based on the nonlinear realization is rigorous and consistent but possesses the real drawback of absence of fermions in the game. On the contrary, though the doubled gauge field approach looks artificial, it allows one to take fermions into account. Similarly, the aforementioned approaches seem to be tightly related to each other, and the puzzle for both approaches is to construct duality-symmetric action for graviton and its dual partner. The necessity of making this step can be viewed, for instance, under the derivation of duality-symmetric action for $D = 10$ type IIA supergravity [15]. As was mentioned above, the Kaluza–Klein reduction of the duality-symmetric with respect to the 3- and 6-index photons $D = 11$ supergravity cannot provide the duality-symmetric structure of type IIA supergravity in the subsector of fields coming from the reduction of the metric tensor. This fact forces to make additional efforts to recover complete duality-symmetric formulation of $D = 10$ type IIA supergravity. On the other hand, having a formulation for $D = 11$ supergravity which is completely duality-symmetric with respect to all the fields including the graviton, the complete duality-symmetric structure of $D = 10$ type IIA theory could be recovered in a straightforward way. The search for the extension of a duality-symmetric

formulation with graviton field will shed light on the relation between the doubled field and nonlinear realization approaches and will be helpful in overcoming the drawbacks of the latter.

REFERENCES

1. L. Randall and R. Sundrum, Phys. Rev. Lett. **83**, 3370 (1999).

2. E. Bergshoeff, R. Kallosh, T. Ortin, *et al.*, Class. Quantum Grav. **18**, 3359 (2001).

3. E. Cremmer and B. Julia, Nucl. Phys. B **159**, 141 (1979).

4. B. Julia, in *Lectures in Applied Mathematics* (AMS–SIAM, 1985), Vol. 21, p. 335.

5. S. Mizoguchi, Nucl. Phys. B **528**, 238 (1998).

6. P. C. West, J. High Energy Phys. **0008**, 007 (2000); Class. Quantum Grav. **18**, 4443 (2001); M. R. Gaberdiel, D. I. Olive, and P. C. West, Nucl. Phys. B **645**, 403 (2002); P. C. West, Class. Quantum Grav. **20**, 2393 (2003); F. Englert, L. Houart, A. Taormina, and P. C. West, J. High Energy Phys. **0309**, 020 (2003).

7. F. Englert and L. Houart, hep-th/0311255.

8. K. Koepsell, H. Nicolai, and H. Samtleben, Class. Quantum Grav. **17**, 3689 (2000).

9. T. Damour, M. Henneaux, and H. Nicolai, Phys. Rev. Lett. **89**, 221601 (2002).

10. B. Julia, hep-th/9805083; hep-th/0002035.

11. E. Cremmer, B. Julia, H. Lü, and C. N. Pope, Nucl. Phys. B **535**, 242 (1998).

12. I. Bandos, N. Berkovits, and D. Sorokin, Nucl. Phys. B **522**, 214 (1998).

13. G. Dall'Agata, K. Lechner, and D. P. Sorokin, Class. Quantum Grav. **14**, L195 (1997).

14. G. Dall'Agata, K. Lechner, and M. Tonin, J. High Energy Phys. **9807**, 017 (1998).

15. I. A. Bandos, A. J. Nurmagambetov, and D. P. Sorokin, hep-th/0307153.

16. P. Pasti, D. P. Sorokin, and M. Tonin, Phys. Lett. B **352**, 59 (1995); Phys. Rev. D **52**, 4277 (1995); Phys. Rev. D **55**, 6292 (1997).

17. E. Cremmer, B. Julia, H. Lü, and C. N. Pope, Nucl. Phys. B **523**, 73 (1998).

18. E. Cremmer, B. Julia, and J. Scherk, Phys. Lett. B **76B**, 409 (1978).

19. I. V. Lavrinenko, H. Lü, C. N. Pope, and K. S. Stelle, Nucl. Phys. B **555**, 201 (1999).

20. F. Gianni and M. Pernici, Phys. Rev. D **30**, 325 (1984).

21. I. C. G. Campbell and P. C. West, Nucl. Phys. B **243**, 112 (1984).

22. M. Huq and M. Namazie, Class. Quantum Grav. **2**, 293 (1985).

Nonexponential ^{125m}Te Radioactive Decay

S. K. Godovikov

*Skobel'tsyn Research Institute of Nuclear Physics, Moscow State University,
Vorob'evy gory, Moscow, 119992 Russia*
Received November 13, 2003; in final form, January 26, 2004

Nonexponential decay of isomeric ^{125m}Te nuclei having intermediate Mössbauer levels and surrounded by their own decay products is observed and studied. A collective decay model is suggested for the nuclear systems of this type. © 2004 MAIK "Nauka/Interperiodica".

PACS numbers: 23.20.Lv; 21.10.Tg; 76.80.+y

Attempts to control radioactive decay using the own γ radiation of a nucleus have been undertaken since the discovery of the fundamental laws of radioactivity. For example, it was claimed in Eddington's book [1] published in 1926 that radium decay is a spontaneous event if the radium atom is an isolated system, but this decay can be stimulated by the gamma-radiation field of frequency coinciding with the frequency of gamma rays emitted in radium decay. Unfortunately, this simple idea has not found experimental confirmation and practical implementation in the 20th century. The main difficulty likely consists in the fact that the recoil energy of the nuclei emitting γ-ray quanta strongly reduces the nuclear resonance Q factor and the probability of formation of a cooperative γ-radiation field. The discovery of recoilless Mössbauer emission lines in 1958 has given impetus to many new expectations, up to the generation of a coherent γ-radiation beam, similar to optical lasers. However, these expectations have not been borne out. The reason consists in the strong self-absorption in a source of soft (several tens of keV) radiation, as a result of which the generation threshold can by no means be achieved for γ-ray quanta. Nevertheless, the potentialities of using Mössbauer radiation with the aim of controlling the radioactive decay process are still far from being exhausted. Starting in 1998, certain progress in this direction was achieved in the use of nuclei of long-lived (hundreds of days) isomers having intermediate Mössbauer levels and surrounded by many products of their decay [2–4]. This work reports the results of studying the ^{125m}Te isomer following this scheme.

Statement of the problem. The ^{125m}Te-decay scheme is presented in Fig. 1. The energy of the isomeric level equals 145.0 keV, its decay period is $T_{1/2} = 58$ days, the energy of the intermediate Mössbauer level is 35.6 keV, and $T_{1/2} = 1.4 \times 10^{-9}$ s. The conversion ratios α are equal to 366 and 12.5, respectively. With the aim of making the decay nonspontaneous, an individual ^{125m}Te nucleus is surrounded by many stable

^{125}Te nuclei that can easily be excited by the 35.6-keV radiation, giving rise to many emission and reemission events induced by a single γ-ray quantum in the system of stable nuclei. In addition, closely spaced ^{125m}Te and ^{125}Te nuclei can form a system in which the wave emitted from the radioactive nucleus and the wave reemitted from the stable nucleus counterpropagate. Under these conditions, the interference pattern can arise on the basis of standing waves, whose antinodes (with a lifetime of ~10^{-9} s) may coincide with the positions of as yet undecayed isomeric nuclei. A high concentration of the stable and sharply resonant nuclei, a rather high concentration of isomeric nuclei, and the ease of coupling between both of them are favorable to the appearance of a collective nuclear system in which the individual decay events are no longer spontaneous and independent from each other, while the decay equation becomes nonlinear.

It should be noted that the isomeric and intermediate levels with an almost multiple energy ratio (4.07) can, in principle, interact through the dynamic oscillation synchronization effect (nuclear Huygens effect [5, 6]). The nonideal multiplicity does not hamper the partial excitation of the upper level, because the effect is some-
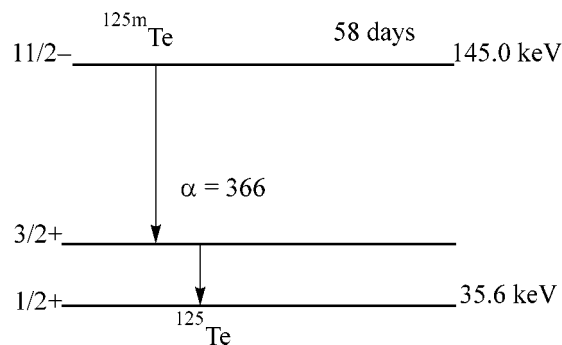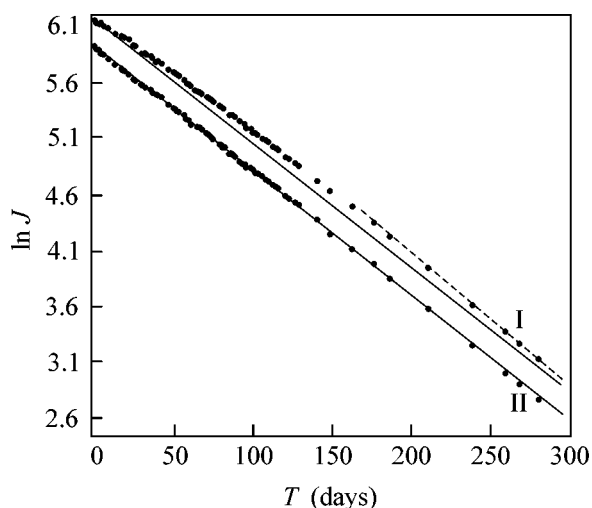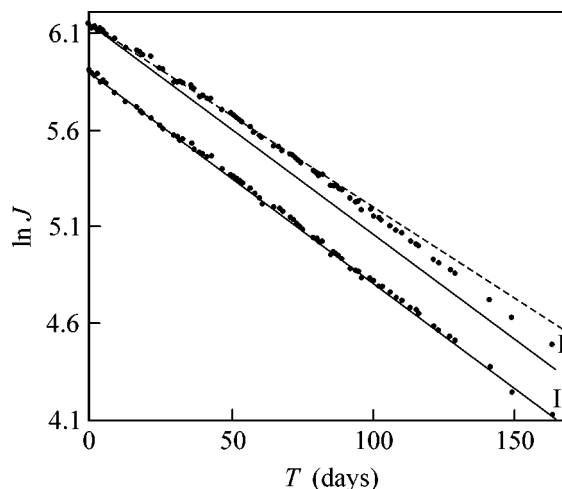

Fig. 1. Decay scheme for the ^{125m}Te isotope.

Fig. 2. Decay curves for sources I and II over the period of 0–281 days. The solid lines are for the normal decay law ($T_{1/2} = 62$ days) and the dashed line is the exponential approximation for the interval of 177–281 days.

Fig. 3. Decay curves of sources I and II over the period of 0–163 days. The solid lines are for the normal decay law ($T_{1/2} = 62$ days) and the dashed line is the exponential approximation for the interval of 0–80 days.

what smeared in energy [6], so that no autocorrection of oscillation frequency is required for this specific resonance to show up.

Experimental. The ^{125m}Te isomer was produced in a reactor by the irradiation of the stable ^{124}Te isotope in a neutron flux of 10^{13} 1/(s cm^2) for several days. Then, it was subjected to a chemical procedure consisting in the preparation of Mg_3TeO_6 compound on the basis of this isotope. Magnesium orthotellurate represents the modern chemical form of the Mössbauer ^{125m}Te sources, because it possesses a high Mössbauer probability and a sufficiently narrow emission line at 293 K. The chemical oxidation reactions of metallic tellurium and the synthesis of the compound were carried out in liquid media at $T = 293$ K. The control Mössbauer measurements of the source and the X-ray structural measurements confirmed its identity with the expected parameters and its chemical formula. In line with the purposes of this study, two sources (I and II) of approximately equal activity (~8 μCi) but with strongly different contents of the stable Mössbauer ^{125}Te isotope were fabricated from the same material. In source I, for one radioactive ^{125m}Te nucleus, there were 2×10^5 ^{125}Te nuclei. Source II was fabricated mainly from the ^{124}Te isotope and did not contain ^{125}Te in any detectable amount. Source II was a control (reference) source, and source I was the studied source.

The experimental part of the problem consisted of measuring and comparing the decay curves of sources I and II, with the aim of proving their distinction or identity.

The scintillation detection type was chosen. A 1-mm-thick NaJ(Tl) crystal was used to detect Mössbauer emission and the satellite X-ray lines (27.4 and

31.1 keV) that identically reflected the decay of the upper isomeric 145-keV level. A Philips 150 AVP/SF photomultiplier was used. Measurement time ranged from 10 min to 1 h. Subsequent to source I, source II was immediately examined, or vice versa. Measurements were performed with the same detector, the same source–detector separation (13 cm), and the same parameters of energy window. The X-ray and Mössbauer radiations formed a single well-defined peak centered at ~30 keV in the amplitude spectrum. The operation mode with the time scan over 256 channels, but with an immovable source, was similar to that used in measuring Mössbauer spectra. The number J of pulses detected per 1 s in one channel was the measured parameter. Measurements were carried out for ~300 days, which is equal to ~$5T_{1/2}$ for this isotope. The electronic parameters of the nuclear spectrometric path were characterized by a high stability, which was studied over ~7 years. The daily control measurements of the decay curves for the standard sources, several hours a day for many months, invariably gave the standard literature data for $T_{1/2}$.

Experimental results. The measured data are presented in Figs. 2 and 3 in the ln$J$–t(days) coordinates, and errors are within the circle size. The full measurement cycle (0–281 days) is presented in Fig. 2, and measurements by $t = 163$ day are presented in Fig. 3.

The data processing for source II shows that it behaves in a standard way and satisfies the exponential decay with $T_{1/2} = 62 \pm 1$ days (Figs. 2, 3), which is quite close to the commonly accepted value. By contrast, the decay of source I was highly anomalous and, on the whole, could not be processed according to the exponential law. The portions of retarded decay (by $t \approx$ 80 day), normal behavior (80–177 days), and acceler-

Decay parameters of the ^{125m}Te sources

Time interval (days)	Source no.	Decay constant λ (1/day)	Decay period $T_{1/2}$ (days)
0–80	I	9.36×10^{-3}	74 ± 1
177–281	I	11.95×10^{-3}	58 ± 1
0–281	II	11.18×10^{-3}	62 ± 1

ated decay (177–281 days) are clearly seen in the curve. If these portions of the complex curve are approximated by the exponential law, i.e., by the straight line, then the curve processing procedure gives the partial values of the decay constants λ and $T_{1/2}$ (table). The corresponding approximated regions for source I are indicated by the dashed lines in Figs. 2 and 3. The solid lines correspond to the normal decay law characteristic of source II ($T_{1/2} = 62$ days). The region $80 < t < 177$ days for source I is the transition region from the retardation to the acceleration and defies any satisfactory description.

Discussion. Earlier [2–4], it was shown that the decay of radioactive systems of the type presented above is described by the nonlinear differential equation of the form

$$dN/dt = -\lambda(N - AN^3), \qquad (1)$$

where N is the number of radioactive nuclei at time t, λ is the decay constant, and A is some proportionality coefficient. The expression AN^3 results from the pair interaction and appears in the traditional decay equation because it is responsible for the internuclear interaction and equal to the number of retarded nuclei [4]. In a three-level decay scheme of the type shown in Fig. 1,
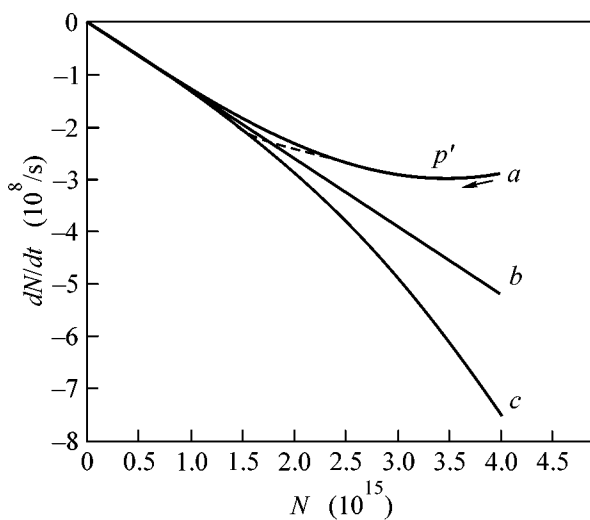
Fig. 4. Graphical representation of the decay equations in the phase plane "rate dN/dt–coordinate N." Curves a, b, and c correspond, respectively, to Eq. (1), $dN/dt = -\lambda N$, and Eq. (4), and the dashed line corresponds to Eq. (3).

the mechanism of this retardation is as follows. The strong collective interaction in the nuclear system produces the level associated with an energy of 35.6 keV, which is excited for a rather long time. The isomeric level, which, in this case, belongs to the system and not to an individual nucleus, starts to face difficulties in the decay to the intermediate level because it is excited for a time. This leads to the retarded decay of some of the nuclei. The number of these nuclei can be estimated from our experimental data. The initial number of the ^{125m}Te nuclei in source I was $N_0 = 2.37 \times 10^{15}$. With $T_{1/2} = 62$ days, they must be 0.384×10^{15} in number by the 163rd day, while their actual number is 0.453×10^{15} (data in Figs. 2, 3). Therefore, 6.9×10^{13} nuclei, or ~18% of the normal amount at the 163rd day, are retarded. It also follows that $A = 2.8 \times 10^{-32}$.

Equation (1) is graphically represented in Fig. 4 in the phase-plane coordinates (curve a). The extreme point p' at

$$N = \pm\sqrt{1/3A} \qquad (2)$$

is a highly characteristic feature of this equation. The positive value of N corresponds to $dN/dt = -\lambda \times 2/3\sqrt{1/3A} < 0$. The negative value of N has the physical meaning of the number of retarded nuclei, which vary with time as $dN/dt = +\lambda \times 2/3\sqrt{1/3A} > 0$. This means that the extremum is a bifurcation point. After this point is passed from right to left (shown by arrow), a new quality is introduced into the system, namely, the possibility of the appearance of "new" nuclei that, after retardation, show a tendency to acceleration. Since the decay retardation and acceleration mechanisms are similar, Eq. (1) for this region of N variation should be modified as

$$dN/dt = -\lambda(N - AN^3 + BN^3), \qquad (3)$$

where $B = B(t)$ is a function of time. At the beginning of the measurement cycle, $B(t) = 0$, whereupon it increases monotonically up to $B = 2A$, where Eq. (3) takes the form

$$dN/dt = -\lambda(N + AN^3). \qquad (4)$$

Equation (4) corresponds to the accelerated decay and is represented in Fig. 4 by curve c. Curves a and c in Fig. 4 are situated, respectively, above and below the normal decay line $dN/dt = -\lambda N$ (Fig. 4, curve b). The parameter B is time-dependent because the collective decay retardation mechanism gradually weakens as N decreases. In the three-level energy scheme of the nuclear ensemble, the upper isomeric level is inversely supersaturated and the intermediate level is deexcited for a rather long time. Under these conditions, an alternative decay branch appears, for which $dN/dt > 0$, so that the decay becomes, on the whole, accelerated, similar to Eqs. (3) and (4). As applied to the conditions of our experiment, Eq. (3) is graphically represented in

Fig. 4 by the dashed line intersecting normal line *b* at a certain point to smoothly match curves *a* and *c*. In principle, Eq. (4) has no extreme point, signifying that the decay retardation processes fully disappears at a sufficiently large *t* and the decay acquires a nonalternative character and becomes accelerated. At $t \gg T_{1/2}$, curves *a*, *b*, and *c* in Fig. 4 virtually merge.

The decay parameters of retarded nuclei can be derived from the experiment. Indeed, their amount decreases from 6.9×10^{13} at $t = 163$ days to 0.95×10^{13} at $t = 281$ days. This gives $T_{1/2} = 41 \pm 1$ days. Therefore, the decay is markedly accelerated, and the spread of $T_{1/2}$ values for the given nuclear system is between 74 and 41 days, with the normal being 62 days.

Equations (1) and (4) have analytic nonexponential solutions given by

$$N = [1/(A - \exp(2\lambda t)C)]^{1/2}, \quad C = (AN_0^2 - 1)/N_0^2, \quad (5)$$

and

$$N = [1/(C^* \exp(2\lambda t) - A)]^{1/2}, \quad C^* = (AN_0^2 + 1)/N_0^2. \quad (6)$$

At $t \gg T_{1/2}$, Eqs. (5) and (6) take the standard form $N = N_0 \exp(-\lambda t)$.

Thus, the main characteristics of the observed nonexponential ^{125m}Te decay can be explained within the framework of the suggested model of collective interaction between Mössbauer nuclei. The variations in the decay constant can likely be considerably enhanced. To this end, it is necessary to profoundly increase the nuclear concentration in the source, as a result of which, according to Eqs. (1) and (4), both the decay retardation and the decay acceleration should be more pronounced. The same result should be obtained by cooling the source (down to 4.2 K), because the recoilless γ-ray-quantum-emission factor increases with lowering temperature.

Note in conclusion that the results of this work have no relevance to the Mössbauer experiments with synchrotron radiation [7], where the dynamic and quantum beats in the decay curve for the nuclear level were observed on the nanosecond time scale. The same is true for the results of [8], where small anomalies in the β-decay rate of some isotopes were associated with cosmic factors. Works on a search for the influence of electromagnetic zero-point oscillations on the decay of Mössbauer levels in the presence of a distant (at several cm) resonance screen [9, 10] are also not associated with the subject of this work, if only for the reason that the theory of this assumed phenomenon [10] predicts the spontaneous monotonic exponential character of decay. In addition, the screen in terms of [10] is absent in this work.

REFERENCES

1. A. Eddington, *The Internal Constitution of the Stars* (Cambridge Univ. Press, Cambridge, 1926), Chap. 11, Sect. 211.

2. S. K. Godovikov, Laser Phys. **10**, 1293 (2000).

3. S. K. Godovikov, Izv. Ross. Akad. Nauk, Ser. Fiz. **65**, 1063 (2001).

4. S. K. Godovikov, Pis'ma Zh. Éksp. Teor. Fiz. **75**, 595 (2002) [JETP Lett. **75**, 499 (2002)].

5. S. K. Godovikov, Pis'ma Zh. Éksp. Teor. Fiz. **68**, 599 (1998) [JETP Lett. **68**, 629 (1998)].

6. O. I. Sumbaev, Izv. Ross. Akad. Nauk, Ser. Fiz. **62**, 6 (1998).

7. G. V. Smirnov, Izv. Ross. Akad. Nauk, Ser. Fiz. **67**, 984 (2003).

8. Yu. A. Baurov, A. A. Konradov, V. F. Kushniruk, *et al.*, Mod. Phys. Lett. A **16**, 2089 (2001).

9. V. G. Alpatov, Yu. D. Bayukov, A. V. Davydov, *et al.*, in *Abstracts of 53rd International Workshop on Nuclear Spectroscopy and the Structure of Atomic Nucleus, Moscow, 2003* (S.-Peterb. Gos. Univ., St. Petersburg, 2003), p. 243.

10. V. I. Vysotskii, Phys. Rev. C **58**, 337 (1998).

Translated by V. Sakun

On the Phenomenon of Oscillatory Decay of the ^{125m}Te Isomer

A. A. Opalenko[1],*, V. I. Vysotskiĭ[2], and A. A. Kornilova[1]

[1] *Moscow State University, Vorob'evy gory, Moscow, 119899 Russia*
*e-mail: tellur125@mail.ru
[2] *Shevchenko National University, Vladimirskaya ul. 64, Kiev, 01033 Ukraine*
Received June 23, 2003; in final form, February 2, 2004

The radioactive decay curve of the ^{125m}Te nucleus is measured in the environment of stable ^{125}Te nuclei representing a Mössbauer resonant screen. Thorough analysis shows that the decay of the ^{125m}Te nucleus corresponds to the standard exponential law with half-life $T_{1/2} \approx 58$ days without oscillations. © *2004 MAIK "Nauka/Interperiodica".*

PACS numbers: 23.20.Lv; 29.30.Kv; 76.80.+y

The control of the spontaneous decay of excited and radioactive nuclei is one of the most interesting problems of fundamental and applied nuclear physics. The use of a system of identical nuclei in the ground state (Mössbauer resonant screen) is one of the most promising methods of such a control of spontaneous decay.

The problem of the direct influence of the resonant screen on the spontaneous-decay rate of γ-radioactive nuclei and the qualitative theory of this influence (due to a change in the spectrum of the electromagnetic vacuum modes surrounding excited nuclei) were likely first considered in 1984 in [1]. In that work, the possibility of controlling the lifetime of ^{119m}Sn nuclei using a resonant screen of unexcited ^{119}Sn isotope was analyzed as an example. The theory of influence of an arbitrary system of unexcited atoms and nuclei on the characteristics of spontaneous γ decay was proposed in [2]. Experiments on the control of the parameters of nuclear decay of the ^{57}Fe and ^{119}Sn isotopes using a resonant screen were performed in [3, 4]. The resonant screen was found to change the total half-life of the Mössbauer levels of these nuclei by 0.5–2%.

Among other experimental results in this direction, works [5–7] deserve attention. It was found in [5] that, as the temperature decreased from 295 to 80 K, the radioactive decay rate of impurity ^{123m}Te atoms in the MgO matrix increased due to an increase in the Mössbauer factor: $\Delta\lambda/\lambda = 0.01$. In [6], a decrease to $\Delta\lambda/\lambda = -(0.11\text{–}0.32)\%$ in the decay rate of the ^{119m}Sn isomer (a parent nucleus for the 23.8-keV Mössbauer level) was observed in the presence of the internal screen. Nonexponential (oscillatory) radioactive-decay curves were observed in [7] for the ^{119m}Sn isomer and ^{125}Sb nucleus, which is a parent nucleus for the 35.6-keV Mössbauer level of ^{125m}Te.

Taking into account that the anomalous spontaneous decay was studied in [7] for the ^{125m}Te Mössbauer transition with energy $E_\gamma = 35.6$ keV, it was expedient to study only the ^{125m}Te $\longrightarrow$ ^{125}Te transition with $T_{1/2} = 58$ days rather than the total decay of the mother nucleus ^{125}Sb $\longrightarrow$ ^{125m}Te $\longrightarrow$ ^{125}Te with $T_{1/2} = 2.7$ yr.

The source under investigation was a magnesium tellurate powder prepared from tellurium enriched to 85% with the stable ^{124}Te isotope. The source was activated to 10 mCi (corresponding to the presence of 10^{15} ^{125m}Te nuclei) in a reactor by thermal neutrons. However, about 9% of the Te isotope remained in the raw material enriched with the ^{124}Te isotope. This corresponded to the presence of 10^{20} ^{125}Te nuclei in the form of magnesium tellurate in the source. It follows from these estimates that for each ^{125m}Te nucleus there were about 10^5 ^{125}Te nuclei. This relation satisfies the condition for internal "active screen" [6].

Figure 1a shows the radiation spectrum obtained for the ^{125m}Te isotope on a scintillation detector with a thin NaJ(T1) crystal. The high peak corresponds to the superposition of several tellurium radiation lines: x-ray lines (27.4-keV K_α and 31.2-keV K_β lines) and the 35.6-keV γ line of Mössbauer transition. The low peak is a characteristic escape peak for 35.6-keV γ rays. It corresponds to the mechanism of escape of the characteristic iodine K_α radiation beyond the scintillator in the course of γ-ray absorption: $E_{esc} = E_\gamma - E_{K_\alpha} = 7$ keV. The intensity ratio of these two peaks is caused by the high internal conversion coefficient ($N_e/N_\gamma = 300$) for the isomeric ^{125m}Te level.

The total amplitude spectrum was decomposed into two Gaussian peaks, N_x and N_γ. The time dependence of the intensity of the N_x peak is shown in Fig. 2, where the upper line corresponds to the simplest source–detector experimental scheme. The lower line characterizes the variation of N_x intensity in the presence of an additional resonance magnesium tellurate absorber on the source surface. In other words, this line corresponds to a mod-

ified source–resonant absorber–detector experimental scheme. The additional resonant absorber makes the scheme more ideal, because it compensates the insufficiency of the internal screen for the nuclei lying on the source surface.

According to these data, both lines change identically and correspond to the exponential decay with a half-life of about 58 days, characteristic of the ^{125m}Te isotope. It is seen that the additional resonant screen for surface nuclei does not affect the decay character (to within the experimental accuracy). Both decay curves are strictly monotonic and show no oscillations. It is impossible to determine the exact half-life in our experiment, because we determine the total x-ray intensity from tellurium, while our source may contain the ^{127}Te, ^{129m}Te, and ^{131}Te radioactive isotopes. The matter is that the tellurium used for irradiation contains (according to the certificate) the ^{124}Te (85.4%), ^{125}Te (9.6%), ^{126}Te (2.9%), ^{128}Te (1%), and ^{130}Te (1%) isotopes. The ^{127}Te isotope can contribute to the N_x peak with a half-life of 109 days. The ^{129m}Te isotope, with a half-life of 34 days, contributes to the N_x peak from its x radiation and unresolved from it 27.8-keV γ radiation. However, the contribution of these isotopes is rather small: the cross section for the thermal-neutron activation of ^{124}Te $\sigma_n = 7$ b, whereas for ^{126}Te, ^{128}Te, and ^{130}Te it is equal to 1, 0.2, and 0.02 b, respectively.

The time dependence of the N_γ-peak intensity is shown in Fig. 3. This dependence was monotonic for the first 40 days, whereupon mysterious oscillations appeared on both curves. The explanation of these oscillations proved to be very simple: during these days, both peaks were arbitrarily shifted from their initial positions (see Fig. 1b). These shifts were caused by the instability of the detection path because of a change in the ambient temperature, fluctuations of feeding voltage, aging of electronics in the detection system, etc.

As a result, the left peak, which is immediately adjacent to the left detection edge, is very sensitive to fluctuations; small changes in its position lead to considerable changes in the peak area (when this peak is shifted to the left, it falls outside the discriminator window, leading to a decrease in intensity; when this peak is shifted to the right, the peak part corresponding to the noise region is detected, leading to an increase in intensity). As a result, these changes are detected as changes in the spontaneous decay rate, although they have no relevance to this rate.

In contrast, the changes in the position of the N_x peak do not affect its intensity, because the entire area of the Gaussian peak is detected. Indeed, this peak is far from both the left and the right detection edges and is well separated from the neighboring peak.

Therefore, all oscillations observed in the spontaneous-decay curve for the ^{125m}Te nucleus are certain to be errors of the measurement procedure! In addition, any

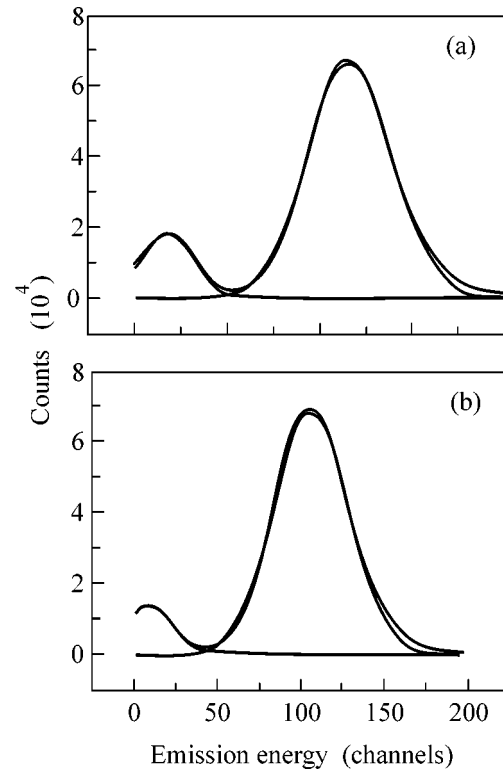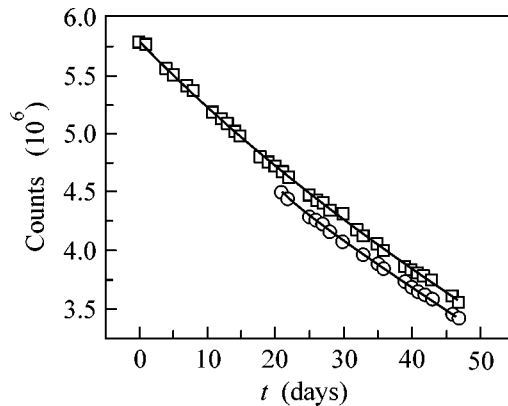**Fig. 1.** Emission spectrum of the ^{125m}Te isomer in the (a) stable and (b) unstable regimes.

Fig. 2. Decay curve: x peak.

conclusion about a change in the radioactive decay rate of the ^{125m}Te isomer drawn from the detection of the x-ray peak is groundless. This requires the detection of 35.6-keV γ-ray quanta, which is possible only with a semiconductor detector. In this work, our purpose was to analyze the shape of the radioactive decay rate.

In [7], the Mössbauer measurement procedure was used with a narrow discriminator window and scanning over the analyzer channels. This procedure is appropri-

OPALENKO *et al.*
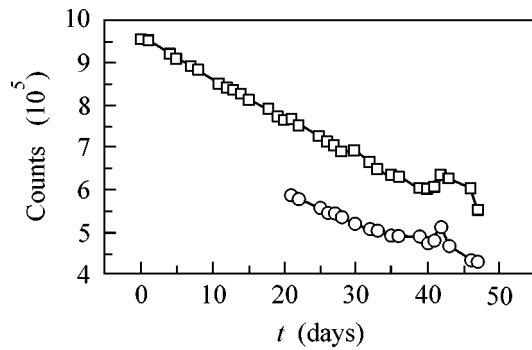
Fig. 3. Decay curve: γ peak.

ate for the Mössbauer spectra, where the absolute intensity is of minor importance. At the same time, to measure the absolute intensity (and spontaneous-decay dynamics), it is necessary either to use a spectrometric system with the stabilization of peak position or to detect the entire spectrum and process only well-separated peaks.

REFERENCES

1. V. I. Vysotskiǐ, V. I. Vorontsov, and R. N. Kuz'min, Pis'ma Zh. Tekh. Fiz. **10**, 300 (1984) [Sov. Tech. Phys. Lett. **10**, 126 (1984)].
2. V. I. Vysotskiǐ, Phys. Rev. C **58**, 337 (1998).
3. V. I. Vysotskiǐ, V. P. Bugrov, A. A. Kornilova, *et al.*, Hyperfine Interact. **107**, 277 (1997).
4. V. I. Vysotskiǐ, A. A. Kornilova, A. A. Sorokin, *et al.*, Laser Phys. **11**, 442 (2001).
5. V. F. Masterov, S. I. Bondarevskiǐ, V. V. Eremin, *et al.*, Fiz. Tverd. Tela (St. Petersburg) **40**, 1832 (1998) [Phys. Solid State **40**, 1661 (1998)].
6. S. K. Godovikov, Laser Phys. **10**, 1293 (2000).
7. S. K. Godovikov, Pis'ma Zh. Éksp. Teor. Fiz. **75**, 595 (2002) [JETP Lett. **75**, 499 (2002)].

Translated by R. Tyapaev

Coulomb Broadening of Nonlinear Resonances
in a Field of Intense Standing Wave

O. V. Belaĭ and D. A. Shapiro*

Institute of Automatics and Electrometry, Siberian Division, Russian Academy of Sciences,
Universitetskiĭ pr. 1, Novosibirsk, 630090 Russia
*e-mail: shapiro@iae.nsk.su
Received January 13, 2004; in final form, January 26, 2004

The problem of probe-field spectrum is considered for a three-level ion placed in a field of an intense standing light wave. The ion interaction with plasma and the velocity-changing Coulomb scattering are taken into account within the weak-collision model. The system of kinetic equations for the density matrix is solved by the expansion in spatial harmonics and eigenfunctions of the collision operator. The profile of nonlinear addition to the probe-wave absorption is determined for various values of the effective ion–ion collision frequencies and various amplitudes and frequencies of standing wave. It is shown that the broadening of the central nonlinear structure in the spectrum is caused by the Coulomb dephasing effect. The computational results are in qualitative agreement with the available experimental data. © 2004 MAIK "Nauka/Interperiodica".

PACS numbers: 34.50.-s; 42.50.-p

The behavior of a two-level atomic system in a field of an intense standing wave does not reduce to the individual interaction with each of the two counterpropagating traveling waves. The traveling waves can be considered independent only in the limit of a weakly saturating field, while, with an increase in the field amplitude, one should take into account the higher spatial harmonics (HSHs). Even harmonics manifest themselves in level populations, and odd harmonics are manifested in coherence (nondiagonal element of the atomic density matrix). In the coherence velocity distribution, so-called $1/n$ resonances appear at velocities $u = \Delta/kn$, where Δ is the detuning between the intense field and the transition frequency, $\mathbf{k}$ is the wave vector, u is the projection of velocity $\mathbf{v}$ on the wave vector, and n is an odd number. In the simplest case of identical relaxation constants and $\Delta = 0$, the velocity distribution reduces to the Bessel function $J_0(G/ku)$ [1], where G is the Rabi frequency. However, HSHs do not affect qualitatively the profile in the case of Lamb dip and only lead to a small quantitative changes on the order of 10% [2]; i.e., the HSH effects level off after averaging over velocities and become practically unobservable.

If a probe field is added at an adjacent transition and one passes to a three-level system, some of the HSH effects become clearly seen in the spectrum [3, 4]. These effects can also be observed if the amplitude of one of the counterpropagating traveling waves is detuned. Experiment in this scheme shows that a singularity appears in the case of close wave amplitudes [5, 6]. The experiment in the scheme with a probe field at the Ar⁺ ions [7, 8] shows that, if the probe field couples a two-level system to a metastable state, HSHs show up

in the resonance case as a dip in the center of a nonlinear transmission contour. Upon detuning from the resonance, the dip transforms into a peak, whose position is independent of detuning. The calculation by the Feldman–Feld formula [3] without inclusion of velocity-changing collisions yielded the proper positions for the dip and peak. However, experimentally, the resonance proved to be broader than in the theory. It was suggested in [7] that the observed broadening results from the velocity-changing ion–ion Coulomb scattering. However, the theory of collision effect in the field of standing wave was lacking because of the complexity of this problem. In the scheme with a probe field in the Λ configuration, the collision effects with changing velocity were calculated only recently even for an intense traveling wave [9, 10].

It is the purpose of this work to calculate the HSH-resonance broadening effects induced by Coulomb collisions. The latter can be taken into account in the weak-collision model, because ion small-angle scattering dominates plasma. Below, we discuss how the nonlinear resonance profile can be represented in the form of a matrix continued fraction, present the results of numerical calculation, and offer a qualitative explanation of the observed broadening.

Let us consider a three-level system $n - m - l$ (Fig. 1) with the fields of an intense standing wave $E(\mathbf{r}, t) = 2Ee^{-i\omega t}\cos\mathbf{kr} + \text{c.c}$ and of a probe traveling wave $E_\mu(\mathbf{r}, t) = E_\mu e^{-i\omega_\mu t + i\mathbf{k}_\mu \mathbf{r}} + \text{c.c.}$ applied at its transitions. The coherences $\rho_{ml} = \rho_a e^{-i\Delta_\mu t}$ of the allowed and
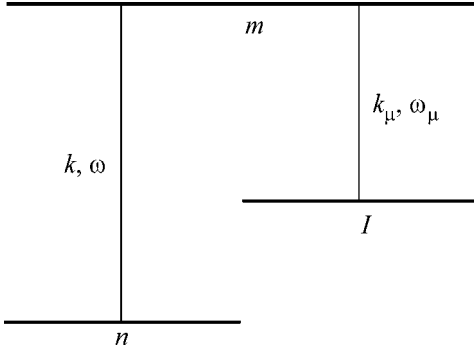
Fig. 1. Three-level system.

$\rho_{nl} = \rho_f e^{-i(\Delta_\mu - \Delta)t}$ of the forbidden transitions obey the system of two coupled equations

$$(\Gamma + u\partial_x)\rho_a + iG\cos kx\rho_f = \hat{S}\rho_a + iG_\mu N_l(u),$$
$$iG\cos kx\rho_a + (\gamma + u\partial_x)\rho_f = \hat{S}\rho_f, \tag{1}$$

where $u = \mathbf{kv}/k$; $x = \mathbf{kr}/k$; $\Delta = \omega - \omega_{mn}$ and $\Delta_\mu = \omega_\mu - \omega_{ml}$ are, respectively, the intense- and probe-field detuning from the frequency of the corresponding transition; N_l is the population of level l; $\Gamma = \Gamma_{ml} - i\Delta_\mu$; $\gamma = \Gamma_{nl} + i(\Delta - \Delta_\mu)$; and the Rabi frequencies $G = Ed_{mn}/2\hbar$ and $G_\mu = E_\mu d_{ml}/2\hbar$ are proportional to the field amplitudes, which are chosen to be real. The Coulomb collisions are described by the Fokker–Planck operator [11]

$$\hat{S} = \nu\left(\frac{v_T^2}{2}\partial_u^2 + \partial_u u\right), \tag{2}$$

where ν is the effective ion–ion collision frequency and v_T is the ion thermal velocity. The wave vectors of the intense and probe waves are chosen to be collinear. On the right-hand side of the second equation in (1), the term with ρ_{mn} that accounts for the nonlinear interference effects is omitted. This simplifies the formulas and corresponds to the experimental situation, where the populations of levels m and n are much lower than the population of the metastable level l.

By applying Fourier-series expansion in spatial harmonics to the unknown coherences ρ_a and ρ_f as periodic functions of x, one can see from Eq. (1) that only the coefficients of even harmonics $n = 2l$ are nonzero for the coherence of allowed transition and only the coefficients of odd harmonics $n = 2l + 1$ are nonzero for the coherence of the forbidden transition,

$$\rho_a = e^{ik_\mu x}\sum_{l=-\infty}^{\infty} a_{2l}\exp(i2lkx),$$

$$\rho_f = e^{ik_\mu x}\sum_{l=-\infty}^{\infty} f_{2l+1}\exp(i(2l+1)kx). \tag{3}$$

Let us introduce new set of functions $x_n(u)$ coinciding with a_n for even n and with f_n for odd n. Then, we obtain from Eq. (1) the infinite chain of coupled Fokker–Planck equations

$$A_n x_n + \frac{iG}{2}(x_{n+1} + x_{n-1}) = \delta_{n0}W_M(u) + \hat{S}x_n,$$
$$n = 0, \pm 1, \ldots, \tag{4}$$

where δ_{mn} is the Kronecker delta and $W_M(u) = \exp(-u^2/v_T^2)v_T\sqrt{\pi}$ is a one-dimensional Maxwellian velocity distribution. Here,

$$A_n = \Gamma_n + i(k_\mu + kn)u, \quad \Gamma_n = \begin{cases} \Gamma, & n = 2l, \\ \gamma, & n = 2l+1, \end{cases} \tag{5}$$

and the probe-field absorption is determined by the zeroth coefficient $\mathscr{P}_\mu(\Delta_\mu) \propto G_\mu^2 \operatorname{Re}\int a_0\, du$ integrated over velocities. To pass from the system of differential equations to a difference equation, we expand x_n in a complete set of normalized eigenfunctions

$$x_n(u) = \sum_{m=0}^{\infty} a_{nm}\psi_m(u),$$

$$\psi_m(u) = \frac{H_m(u/v_T)\exp(-u^2/v_T^2)}{\sqrt{2^m m!}} \tag{6}$$

of the collision operator $\hat{S}\psi_m = m\psi_m$, where $m = 0, 1, \ldots$. Here, H_m are the Hermitian polynomials. This gives the following linear difference equation:

$$i(k_\mu + kn)v_T\left[\sqrt{\frac{m}{2}}a_{n,m-1} + \sqrt{\frac{m+1}{2}}a_{n,m+1}\right]$$
$$+ (\Gamma_n + \nu m)a_{nm} + i\frac{G}{2}(a_{n+1,m} + a_{n-1,m}) = \frac{\delta_{n0}\delta_{m0}}{\sqrt{\pi}}. \tag{7}$$

Now, one needs to find the coefficient a_{00}, through which the field work $\mathscr{P}_\mu \propto G_\mu^2 \operatorname{Re} a_{00}$ is expressed. Equation (7) relates the expansion coefficient a_{nm} to the two neighboring coefficients for index m and two neighboring coefficients for n. In other words, we arrive at an infinite system of linear equations with a block-tridiagonal matrix, each block also being a tridiagonal matrix. Using this matrix structure, one can write the solution in the form of an infinite matrix continued fraction

$$\mathscr{P}_\mu(\Delta_\mu) \propto \operatorname{Re} x_0, \quad x_0 = \frac{1}{\sqrt{\pi}}(UR_0^{-1} + V)_{00}^{-1}, \tag{8}$$

$$R_{m-1} = \alpha_m R_m^{-1} + \beta_m,$$

where

$$(\alpha_m)_{lj} = -\sqrt{\frac{m+1}{m}}\delta_{lj},$$

$$(\beta_m)_{lj} = -\sqrt{\frac{2}{m}}\frac{\dfrac{G}{2}(\delta_{j,l-1}+\delta_{j,l+1})-i(\Gamma_m+m\nu)\delta_{lj}}{k_\mu+lk}, \quad (9)$$

$$U_{nj} = \frac{i}{\sqrt{2}}(k_\mu+kn)\delta_{nj},$$

$$V_{nj} = \Gamma_n\delta_{nj}+i\frac{G}{2}(\delta_{j,n+1}+\delta_{j,n-1}), \quad (10)$$

and $(\ldots)_{ij}$ stands for the ijth matrix element. The matrices α_m and β_m prove to be diagonal and tridiagonal, respectively.

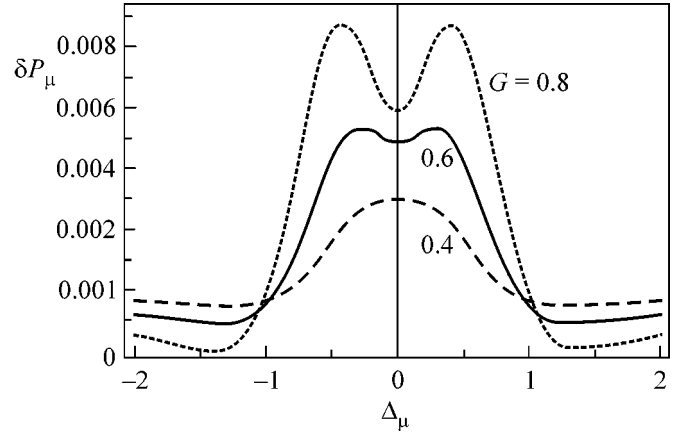The nonlinear correction to the probe-field work

$$\delta\mathscr{P}_\mu = \mathscr{P}_\mu|_{G=0} - \mathscr{P}_\mu \quad (11)$$

was found numerically. It is presented in Figs. 2–4 in arbitrary units as a function of probe-field detuning. The matrices R_m in Eq. (8) were inverted at each step by the rotation method, whose optimal properties are considered in [12]. The maximal values $M = \max m$ and $N = \max|n|$ were doubled until the prescribed relative error was achieved; in Figs. 2–4, it is equal to 10^{-4}. The number N of important spatial harmonics increased with increasing Rabi frequency G of intense field, while the number M of Hermitian polynomials necessary for providing the required accuracy decreased with increasing collision frequency ν. For the parameters used in calculations, the boundary values were $N \sim 10^2$ and $M \sim 10^4$. Such a behavior is in agreement with the qualitative picture of the phenomenon. After substituting in Eq. (1) ρ_a in the form of a series in powers of G, $\cos 2kx$ will appear as a coefficient of G^2, $\cos 4kx$ as a coefficient of G^4, and so on. Hence, as G decreases, the number of harmonics contributing to the field work becomes progressively smaller. The diffusion in the velocity space, which is described by the Fokker–Planck operator, primarily smooths out the irregular functions corresponding to the Hermitian polynomials with large m.

The dependence of the nonlinear addition on the effective collision frequency is shown in Fig. 2, where the curve number multiplied by 10^{-3} gives the ν/Γ_{nl} value. Hereafter, all quantities of frequency dimension are given in units of Γ_{nl}. One can see that the HSH dip in the center of the contour broadens as the frequency ν increases. At $\nu/\Gamma_{nl} > 4 \times 10^{-3}$, the dip is completely blurred. The parameters chosen for numerical calculation were close to their experimental values. In Figs. 3 and 4, the spectra are shown for several values of Rabi frequency and intense-field detuning, respectively. One
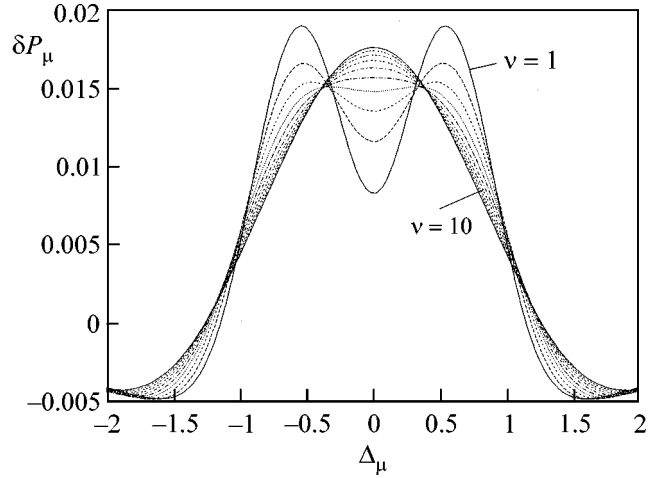
Fig. 2. Nonlinear addition to the probe-field spectrum for $\Delta = 0$, $k = 16.6$, $k_\mu = 11.8$, $G = 1.2$, $\Gamma_{ml} = 0.09$, and various $\nu = (1-10) \times 10^{-3}$.

Fig. 3. Nonlinear addition to the probe-field work for $\Gamma_{ml} = 0.06$, $G = 0.8$, $kv_T = 18$, $k_\mu v_T = 13$, $\nu = 10^{-3}$, and $\Delta = 0$. The G values are indicated near the curves.
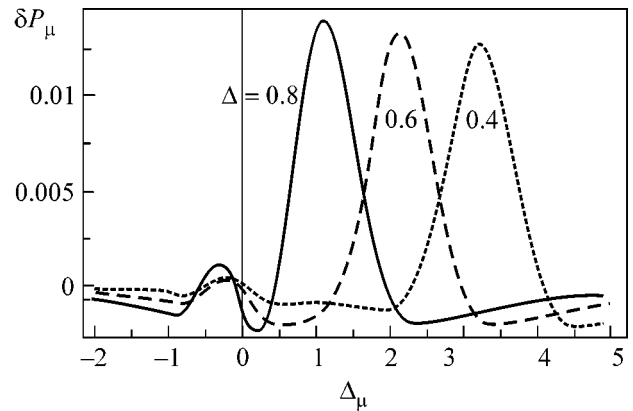
Fig. 4. The same as in Fig. 3 but for $G = 0.8$ and three different Δ values (indicated near the curves).
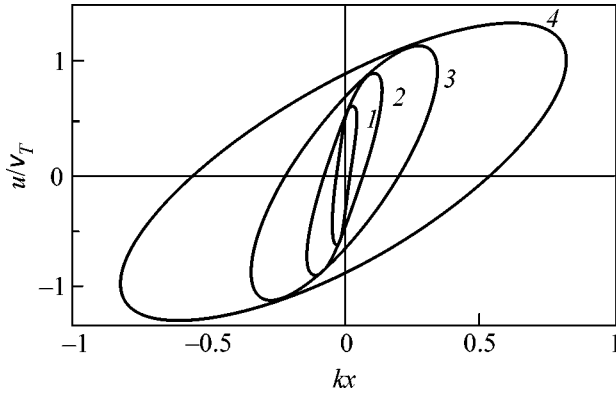
Fig. 5. Shape of the particle cloud in the phase plane for $\nu t = 0.1, 0.25, 0.5$, and 1.0 (curves *1–4*, respectively).

can see in Fig. 3 that, in the resonance case, the dip in the center of the contour becomes deeper with an increase in the amplitude of intense field. Figure 4 demonstrates how the dip transforms into a peak, whose position ceases to depend on Δ as the intense-field detuning increases. Contrary to the calculation [7] by the Feldman–Feld formula, the HSH resonance proved to be broadened.

The observed broadening can be qualitatively explained by the Coulomb dephasing, which was briefly discussed in [9, 11]. Let us consider a group of ions with zero velocity projection u onto the wave-vector direction and map it onto the phase plane $(kx, u/v_T)$. After some time, ions will acquire positive or negative velocities because of the Coulomb diffusion in the velocity space, and the point at the origin of coordinates of the phase plane will turn to a segment extended along the u axis. Ions with positive velocity will shift to the right in the phase plane, and ions with negative velocity, to the left. The segment will transform into an ellipse with increasing sizes. It rotates clockwise and is shown for several instants of time t in Fig. 5. Mathematically, these ellipses are isolines of the nondiagonal Green's function in the weak-collision model [13]:

$$\Phi(x, u, t) = \exp\left(-\frac{c\tilde{x}^2 - 2b\tilde{x}\tilde{u} + a\tilde{u}^2}{2(ac - b^2)}\right),$$

$$\tilde{x} = kx, \quad \tilde{u} = \frac{u}{v_T}, \quad a = 2\left(\nu t - h - \frac{h^2}{2}\right), \quad (12)$$

$$b = h^2, \quad c = 1 - e^{-2\nu t}, \quad h = 1 - e^{-\nu t}.$$

When the horizontal size of the ellipse exceeds λ/n, where $\lambda = 2\pi/k$ is the wavelength and n is the spatial-harmonic number, the effect of this harmonic will be blurred out. At $\nu t \ll 1$, the broadening in the vertical direction follows the diffusional law $\delta u/v_T = (\nu t)^{1/2}$. By equating the motional broadening along the horizontal $\delta x = \delta u t = \nu^{1/2}t^{3/2}v_T$ and the wavelength λ/n of the nth

spatial harmonic, we estimate the broadening by $\delta\omega \sim (\nu\, v_T^2 k^2)^{1/3}n^{2/3}$. For the experimental parameters $\nu = 2 \times 10^7$ s^{-1}, $v_T = 2 \times 10^5$ cm/s, $k = 10^5$ cm^{-1}, and $n \sim 2$, we have $\delta\omega \sim 2 \times 10^9$ s^{-1}, or 300 MHz.

In the experiment on the electromagnetically induced transparency with Λ configuration [7], the metastable ArII $|l\rangle = 3d^2P_{3/2}$ state was chosen as the final state, and the broader states $|n\rangle = 4s^2P_{3/2}$ and $|m\rangle = 4p^2S_{1/2}$ were chosen as the initial and intermediate states, respectively. The measured dip width in the center of the contour was equal to 150–200 MHz for the standing wave tuned to the resonance with the n–m transition, whereas the theory of perturbation gives $2\Gamma_{ml}^0$. The unperturbed resonance width is $\Gamma_{ml}^0 = \frac{1}{2}(\Gamma_m + \Gamma_l) = 20$ MHz. Although the Stark broadening of the m–l transition is unknown, its upper estimate can be derived from other analogous lines, to give $\Delta\Gamma_{ml} \lesssim 30$ MHz; then, $2\Gamma_{ml} \lesssim 100$ MHz. Hence, the experimental broadening is at least 1.5–2 times greater than the broadening given by the theory disregarding the velocity-changing collisions. If the standing wave was detuned from the resonance, a broadened peak, instead of a dip, was observed in the center of the probe-field spectrum. As compared to the theory of perturbations and the Feldman–Feld formula, the broadening was also greater by a factor of 1.5–2. The estimate presented above for the Coulomb-dephasing broadening is in agreement, in the order of magnitude, with the experimental value both for the central dip in the resonance case (Fig. 3) and for the broadened peak (Fig. 4) far from resonance.

Thus, numerical calculation of the matrix continued fraction has shown that the HSH-resonance contrast increases with increasing amplitude G and decreases with an increase in the intense-field detuning Δ. It has been found that the broadening of the HSH resonance is caused by the Coulomb dephasing and the quantitative results are in agreement, in the order of magnitude, with the experiment.

REFERENCES

1. S. G. Rautian and I. I. Sobel'man, Zh. Éksp. Teor. Fiz. **44**, 934 (1963) [Sov. Phys. JETP **17**, 635 (1963)].

2. S. G. Rautian, G. I. Smirnov, and A. M. Shalagin, *Nonlinear Resonances in Atomic and Molecular Spectra* (Nauka, Novosibirsk, 1979).

3. B. J. Feldman and M. S. Feld, Phys. Rev. A **5**, 899 (1972).

4. S. Stenholm, Phys. Rep. **43**, 151 (1978).

5. A. M. Bonch-Bruevich, T. A. Vartanyan, and N. A. Chigir', Zh. Éksp. Teor. Fiz. **77**, 1899 (1979) [Sov. Phys. JETP **50**, 901 (1979)].

6. A. M. Mak, S. G. Przhibel'skiǐ, and N. A. Chigir', Izv. Akad. Nauk SSSR, Ser. Fiz. **47**, 1976 (1983).

7. S. A. Babin, E. V. Podivilov, V. V. Potapov, *et al.*, Zh. Éksp. Teor. Fiz. **121**, 807 (2002) [JETP **94**, 694 (2002)].

8. S. A. Babin, D. V. Churkin, E. V. Podivilov, *et al.*, Phys. Rev. A **67**, 043808 (2003).

9. M. G. Stepanov and D. A. Shapiro, Pis'ma Zh. Éksp. Teor. Fiz. **68**, 27 (1998) [JETP Lett. **68**, 29 (1998)].

10. Yu. I. Belousov and D. A. Shapiro, J. Phys. B: At. Mol. Opt. Phys. **36**, 1495 (2003).

11. S. A. Babin and D. A. Shapiro, Phys. Rep. **241**, 119 (1994).

12. S. K. Godunov, *Modern Aspects of Linear Algebra* (Nauchnaya Kniga, Novosibirsk, 1997).

13. S. G. Rautian and I. I. Sobel'man, Usp. Fiz. Nauk **90**, 209 (1966) [Sov. Phys. Usp. **9**, 701 (1967)].

Translated by V. Sakun

Self-Compression and Catastrophic Collapse
of Photon Bullets in Vacuum¶

M. Marklund[1], *, B. Eliasson[2], and P. K. Shukla[2, 3]

[1] Department of Electromagnetics, Chalmers University of Technology, SE-41296 Göteborg, Sweden
[2] Fakultät für Physik und Astronomie, Ruhr-Universität Bochum, D-44780 Bochum, Germany
[3] Department of Physics, Umeå University, SE-90187 Umeå, Sweden
*e-mail: marklund@elmagn.chalmers.se
Received January 5, 2004

Photon–photon scattering, due to photons interacting with virtual electron–positron pairs, is an intriguing deviation from classical electromagnetism predicted by quantum electrodynamics (QED). Apart from being of fundamental interest in itself, collisions between photons are believed to be of importance in the vicinity of magnetars, in the present generation intense lasers, and in intense laser-plasma/matter interactions, the latter recreating astrophysical conditions in the laboratory. We show that an intense photon pulse propagating through a radiation gas can self-focus and, under certain circumstances, collapse. This is due to the response of the radiation background, creating a potential well in which the pulse gets trapped, giving rise to photonic solitary structures. When the radiation gas intensity has reached its peak values, the gas releases part of its energy into "photon wedges," similar to Cherenkov radiation. The results should be of importance for the present generation of intense lasers and for the understanding of localized gamma-ray bursts in astrophysical environments. They could furthermore test the predictions of QED and give means to create ultraintense photonic pulses. © 2004 MAIK "Nauka/Interperiodica".

PACS numbers: 12.20.Ds; 95.30.Cq

In classical electrodynamics, as described by the Maxwell equations, photons do not interact as long as there is no material medium present. However, due to the interaction of photons with virtual electron–positron pairs, quantum electrodynamics (QED) predicts photon–photon scattering in vacuum [1]. This is commonly modeled by the Heisenberg–Euler (H–E) Lagrangian, which neglects dispersive effects. The H–E Lagrangian gives rise to cubic nonlinear corrections to Maxwell's vacuum equations, similar to the self-interaction terms encountered in optics of Kerr media [2]. The H–E corrections give rise to both single particle effects, such as photon splitting [3, 4], lensing effects in strong magnetic fields [5], like the ones in magnetar environments [6], and to coherent field effects such as harmonic generation [7] and self-focusing of photon beams [8]. Efforts to detect these collisions are being made by using state-of-the-art superconducting microwave facilities [9]. Recently, it has been shown theoretically that QED effects can give rise to two-dimensional collapsing photonic structures in a radiation gas [10], which could be of importance for photon propagation in stellar atmospheres and in the early Universe. Studies of photon pulses in a radiation background and of optical pulses in nonlinear media reveal that they share common features which can be described mathematically by a Schrödinger equation with a nonlinear potential [8, 9].

Dispersive effects can play an important role for short optical pulses when the spatial gradients and time variations become large. One of the most important generic effects of the dispersion is to permit pulse splitting along the direction of propagation [11, 12], which has also been experimentally verified [13]. The pulse splitting is of great interest in applications to normal dispersive media, where the collapse of light pulses can be arrested (which is not possible in anomalous dispersive media [14]), giving rise to a train of high-intensity pulses; these pulses may then work as a source of white light generation [15]. The quantum vacuum also possesses such dispersive effects [8], which can be of importance in the present generation intense lasers [16] where ultrashort high-intensity photon pulses will be produced. Rapidly varying fields are also of interest for the frequency up-shift of photons in photon acceleration [17–19], which is an important ingredient in studies of plasma-based charged particle accelerators and laser-plasma/matter interactions [20], where ultrastrong fields [21–23] are expected to reach from peta- to zeta-watt powers [24]. In this letter, we present for the first time results dealing with the nonlinear propagation of *three-dimensional intense photon pulses* in vacuum where QED effects play a major role. Specifically, we report on new features of nonlinear propagation of a linearly polarized intense photon pulse on a radiation

---

¶ This article was submitted by the authors in English.

gas background, assuming that there is no pair creation and that the field strength E is below the critical Schwinger field, i.e., $\omega \ll m_e c^2/\hbar \simeq 8 \times 10^{20}$ rad s^{-1} and $|E| \ll m_e c^2/e\lambda_c \simeq 10^{18}$ V/m, respectively, where ω is the photon frequency, m_e is the electron mass, e is the magnitude of the electron charge, and λ_c is the Compton wavelength. The derivative corrections to the H–E Lagrangian give rise to a nonlinear dependence of the photon frequency on the wave number, which is shown to permit three-dimensional self-focusing. For moderate intensities of the photon pulse, the self-focusing will be followed by pulse splitting and the formation of stable photonic solitary pulses. However, for high initial powers of the photon pulse, the latter undergoes catastrophic collapse, giving rise to field amplitudes exceeding the Schwinger limit 10^{29} W/cm^2. At these intensities, our theory breaks down and one must consider higher-order nonlinear effects and pair productions. It is argued that higher-order nonlinear effects become important before the Schwinger limit is reached, arresting the collapse and giving rise to ultra-high intensity three-dimensional solitary photonic pulses. Thus, the results presented here give, apart from its immediate fundamental interest and astrophysical applications, a mechanism for creating ultrahigh intensity photon pulses.

The evolution of an intense short photon pulse and the radiation background is governed by the Karpman-like system of equations [8, 10, 25, 26]

$$i\left(\frac{\partial}{\partial t} + v_g \frac{\partial}{\partial z}\right)E + \frac{v_g}{2k_0}\left[\frac{1}{r}\frac{\partial}{\partial r}\left(r\frac{\partial E}{\partial r}\right) - \beta_z \frac{\partial^2 E}{\partial z^2}\right]$$
$$+ \kappa \mathcal{E} E = 0, \qquad (1a)$$

and

$$\left(\frac{\partial^2}{\partial t^2} - \frac{c^2}{3}\nabla^2\right)\mathcal{E} + \mu\epsilon_0\left(\frac{\partial^2}{\partial t^2} + c^2\nabla^2\right)|E|^2 = 0, \qquad (1b)$$

where $\mathcal{E}_0$ and $\mathcal{E}$ are the background and perturbation of the radiation energy density, respectively; $v_g = c(1 - \mu - \mu^2\delta)$ is the group velocity; $\beta_z \simeq 2\mu^2\delta$ is the vacuum dispersion coefficient; and $\kappa \simeq ck_0(1 + \mu\delta)/\mathcal{E}_c$ is the vacuum nonlinear refraction parameter [10]. Here, $\delta \equiv k_0^2/k_c^2$ and $\mu \equiv \mathcal{E}_0/\mathcal{E}_c$, and the critical parameters $k_c^{-1} \sim 10^{-13}$ m, the Compton wavelength divided by 2π, and $\mathcal{E}_c \sim 10^{27}$ J/m^3 are defined by the QED properties of the vacuum.
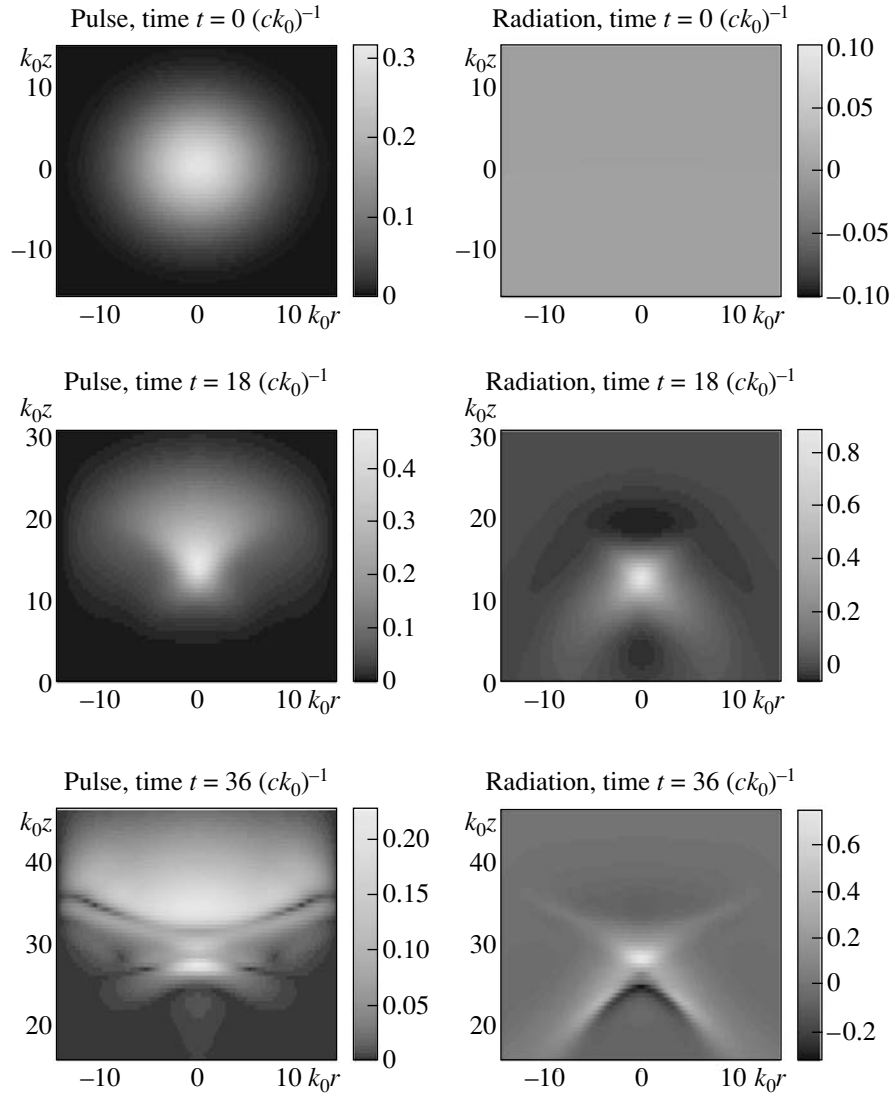
If the time response of the radiation background is slow, then Eq. (1b) may be integrated to yield $\mathcal{E} \simeq 3\mu\epsilon_0|E|^2$ and, from Eq. (1a), we obtain the standard equation for analyzing ultrashort intense pulses in normal dispersive media (see [2, 11, 12] and references therein). It is well known that the evolution of a pulse within this equation is modulationally unstable [2] and

displays first self-focusing and then pulse splitting along the direction of the pulse propagation [11, 12].

We have analyzed system (1) numerically and analytically; in the figure, we display the intensity of the electric field E in the left panels and the perturbation $\mathcal{E}$ of the background radiation in the right panels. As an initial condition, we use a Gaussian pulse for the electric field envelope, $E = E_0 \exp\{-[r^2 + (z + z_0)^2]/a_0^2\}$, while the radiation perturbation is initially set to zero, and $v_g \simeq c$ together with $\beta_z = 10^{-7}$ (relevant to astrophysical applications) (see the upper panels of the figure). The z derivatives in Eqs. (1) are calculated numerically with a pseudospectral method; the r derivatives, with a second-order difference scheme; and the system is advanced in time with a fourth-order Runge–Kutta scheme.

Displayed in the middle panels of the figure is the initial pulse, which is moving in the z direction with a speed close to the speed of light. The pulse is self-focused and exhibits a structure stretched along the z direction. The self-focusing can be understood in the framework of the two-dimensional nonlinear Schrödinger equation; during the initial phase of the pulse propagation, the dispersive term plays a minor dynamical role. If the t and z variations are neglected in Eq. (1b), we obtain $\mathcal{E} \simeq 3\mu\epsilon_0|E|^2$. Thus, Eq. (1b) becomes the standard nonlinear Schrödinger equation in which the cubic nonlinear potential has the same sign as the diffraction term, supporting two-dimensional collapse of the pulse [2]. The time for *complete* two-dimensional collapse of a pulse can be estimated by means of Rayleigh–Ritz optimization. Using normalized units (see the figure), two-dimensional collapse will occur when the intensity and pulse width satisfy the inequality $|E_0|^2 \gtrsim 1.3 a_0^{-2}$. The resulting collapse time $t_c \simeq 4.3 a_0^2 (E_0^2 a_0^2 - 1.3)^{-1/2}$. In the figure, pulse splitting occurs after $\sim t_c/3$, thus well before field strengths reaches critical levels.

However, here, the collapse of the pulse is arrested due to the backscattering from the background; the core of the pulse slows down because of the nonlinear interaction with the background, while the flanks of the pulse continue to propagate with the speed of light, creating a fanlike structure in front of the slower moving pulse (see the middle left panel of the figure). The pulse then splits into several parts with local maxima: one wider pulse which can be seen at $k_0 z = 35$ in the lower left panel followed by two smaller, narrower pulses at $k_0 z \approx 27$. We have carried out simulations with different values of β_z which reveal that the flattening of the leading edge pulse is less pronounced for smaller values of β_z. The wider pulse is correlated with a slight depletion of the radiation energy density. Letting the pulse propagate further, the transverse variation for the wide pulse will become much smaller than the longitudinal variation, leading to an almost one-dimensional struc-

Pulse, time $t = 0$ $(ck_0)^{-1}$

Radiation, time $t = 0$ $(ck_0)^{-1}$

Pulse, time $t = 18$ $(ck_0)^{-1}$

Radiation, time $t = 18$ $(ck_0)^{-1}$

Pulse, time $t = 36$ $(ck_0)^{-1}$

Radiation, time $t = 36$ $(ck_0)^{-1}$

The collapse of the pulse and radiation gas disturbance displayed using normalized electric field intensity $|E|^2$ (left panels) and energy densities $\mathcal{E}$ (right panels). We have scaled the pulse electric field E by $2(3\sqrt{\mu\epsilon_0/\mathcal{E}_c})^{-1}$ and the radiation background $\mathcal{E}$ by $2\mathcal{E}_c/3$, while the time scale is normalized by $(ck_0)^{-1}$, and the length scale, by k_0^{-1}. The initially Gaussian pulse has the amplitude $E_0 = 0.64(3\sqrt{\mu\epsilon_0/\mathcal{E}_c})^{-1}$ and width $a_0^2 = 50/k_0^2$. The upper panels show the initial configuration, while the middle panels give the system after 18 time units, and the lower panels, after 36 time units. The initial photonic pulse in the upper left panel self-focuses and then splits into two pulses, as can be seen in the left middle and lower panels. The energy background emanates Cherenkov-like radiation, clearly seen in the lower right panel as two yellow bands created behind the pulse.

ture (depending weakly on the transverse coordinate r), thus making the nonzero dispersive term essential. This pulse moves with a supersonic speed ($> c/\sqrt{3}$). For these broad supersonic pulses, we may solve Eqs. (1) for the stationary state. The acoustic equation (1b) gives $\mathcal{E} = -3\mu(v_g^2 + c^2)/(3v_g^2 - c^2)\epsilon_0|E|^2$. We note that the pulse will experience resonance phenomena as the group velocity approaches the sound speed. With the solution to Eq. (1b), one can describe the localized stationary solitary solutions for a pulse moving close to the speed of

light according to [2] $|E| \simeq E_0 \text{sech}[(3\varepsilon/\delta)^{1/2}k_0(z - v_g t)]$, where E_0 is the constant amplitude of the pulse and $\varepsilon = \epsilon_0 E_0^2/\mathcal{E}_0$ is the relative energy density of the pulse. We point out that these pulses are not necessarily of extremely high amplitudes. The remnants of radially collapsing pulse asymptotically form a train of low-amplitude axially modulated solitary pulses. Moreover, the pulses show a parabolic self-compression, which will compensate for the small, but nonzero, diffraction of the pulse, making the one-dimensional approxima-

tion valid over a longer period of time. In the final stage, we can see the formation of a "photon wedge" (seen in the lower right panel), which is due to the pulse propagation with a supersonic speed, so that part of the energy of the pulse is released into Cherenkov-like radiation behind the pulse, analogous to the sonic shocks created behind supersonic flights in air. Thus, the dynamics of the photonic pulse is surprisingly complex, exhibiting a multitude of nonlinear phenomena.

Simulations with higher initial amplitudes of the pulse show that the pulse again experiences two-dimensional collapse in which the intensity may grow above the Schwinger limit before photon pulse splitting occurs. Because of the nonlinear dominance, the speed of the pulse decreases below the sound speed of the background, and the Cherenkov energy loss through the photon wedges will therefore be small, reinforcing the photon pulse collapse. This mechanism leads to amplitudes where our model breaks down; thus, the photon collapse becomes catastrophic close to the Schwinger limit [15]. However, before the Schwinger limit is reached, higher-order nonlinear effects are likely to arrest the collapse [27]. This effect is similar to ultrashort intense laser pulses in air, where the formation of a plasma due to self-focusing gives rise to filamentation and halted collapse [28]. The plasma formation gives rise to a significantly longer propagation range for laser pulses in air, a behavior which the QED pulse propagation presented here is expected to share, but with the plasma formation replaced by higher-order QED effects and the pair creation.

Astrophysical environments can be of a very extreme nature, exhibiting the largest energy levels known to man. In the case of regular neutron stars, the surface magnetic field strengths reach 10^{10}–10^{13} G, while in magnetars, they can reach 10^{14}–10^{15} G, the latter being close to the Schwinger limit. An interesting possibility arises in the context of neutron star and magnetar quakes, in which magnetic fields build up tensions in the star crust over long periods of time, and sudden bursts of energy are released from the star during the quakes. There, it is expected that large quantities of low-frequency photons would be ejected, forming an almost incoherent spectrum of waves [29]. This photon gas could reach energy densities of $\mathscr{E}_0 \sim 10^{17}$–$10^{26}$ J/m^3, corresponding to $\mu \sim 10^{-10}$–10^{-1}. A short high-intensity electromagnetic pulse, with wavelengths from the UV to gamma range (corresponding to $\delta \sim 10^{-10}$–10^{-2}), with its evolution modeled by the nonlinear Schrödinger Eq. (1a), passing through this low-frequency photon gas dynamically governed by the acoustic-like wave Eq. (1b), could be a source for gamma-ray bursts. The latter are short (tens of seconds) emissions of photons in the gamma range [30]. Apart from the pulse collapse described by system (1), there will also be a significant blueshift of the photon pulse, due to the formation of steep intensity gradients in the system [15], which we can see in the numerical results of the figure. We note

that the timescales for these events could be extremely short, depending on the frequency of the photons. One can therefore expect the formation of intense photon pulses with frequencies up to the gamma regime, within the incoherent photon gas created by magnetar quakes, possibly giving insight into the dynamics of gamma-ray bursts, since we here have a mechanism both for blue shifting pulse compression and high intensity field generation. However, we note that, in accordance with the standard relativistic fireball model, it would be more appropriate to model incoherent photons by a wave kinetic equation instead of a Schrödinger equation.

To summarize, we have considered the implications of the dispersive properties of the quantum vacuum for the case of intense photon pulses propagating on a radiation background. In the slowly varying acoustic wave limit, the pulse evolves similar to an ultrashort high-intensity pulse in nonlinear, normal dispersive media, with pulse collapse and splitting as a result. The analysis of the full system of equations shows that the slowly varying acoustic limit is far from generic and that the response of the radiation gas can have the same timescale as the pulse evolution. It is due to the self-generation of potential wells, giving an attractive force between the photonic pulse peak and the acoustic disturbance. This can give rise to three-dimensional catastrophic photonic pulse collapse, where the pulse and radiation gas power increases towards the Schwinger limit. Moreover, given suitable initial conditions, the photonic pulses can evolve into a stable localized structure with high field strengths. The application of our work to astrophysical settings has been discussed. Specifically, the present investigation sheds light on gamma-ray burst dynamics and gives a means for obtaining pulse intensities surpassing the ones achievable by known mechanisms.

REFERENCES

1. J. Schwinger, Phys. Rev. **82**, 664 (1951).
2. Y. S. Kivshar and G. P. Agrawal, *Optical Solitons* (Academic, San Diego, 2003).
3. S. L. Adler, J. N. Bahcall, C. G. Callan, and M. N. Rosenbluth, Phys. Rev. Lett. **25**, 1061 (1970).
4. M. G. Baring and A. K. Harding, Astrophys. J. **507**, L55 (1998).
5. A. K. Harding, Science **251**, 1033 (1991).
6. C. Kouveliotou, S. Dieters, T. Strohmayer, *et al.*, Nature **393**, 235 (1998).

7. Y. J. Ding and A. E. Kaplan, Phys. Rev. Lett. **63**, 2725 (1989).

8. N. N. Rozanov, Zh. Éksp. Teor. Fiz. **113**, 513 (1998) [JETP **86**, 284 (1998)].

9. G. Brodin, M. Marklund, and L. Stenflo, Phys. Rev. Lett. **87**, 171801 (2001).

10. M. Marklund, G. Brodin, and L. Stenflo, Phys. Rev. Lett. **91**, 163601 (2003).

11. P. Chernev and V. Petrov, Opt. Lett. **17**, 172 (1992).

12. J. E. Rothenberg, Opt. Lett. **17**, 583 (1992).

13. J. K. Ranka, R. W. Schirmer, and A. L. Gaeta, Phys. Rev. Lett. **77**, 3783 (1996).

14. Y. Silberberg, Opt. Lett. **15**, 1282 (1990).

15. A. L. Gaeta, Phys. Rev. Lett. **84**, 3582 (2000).

16. G. A. Mourou, C. P. J. Barty, and M. D. Perry, Phys. Today **51**, 22 (1998).

17. S. C. Wilks, J. M. Dawson, W. B. Mori, *et al.*, Phys. Rev. Lett. **62**, 2600 (1989).

18. N. L. Tsintsadze, J. T. Mendonça, and L. O. Silva, Phys. Rev. E **58**, 4890 (1998).

19. J. T. Mendonça, *Photon Acceleration* (Inst. of Physics, Bristol, 2001).

20. A. Pukhov, Rep. Prog. Phys. **66**, 47 (2003).

21. V. Malka, S. Fritzler, E. Lefebvre, *et al.*, Science **298**, 1596 (2002).

22. A. Pukhov, S. Gordienko, and T. Baeva, Phys. Rev. Lett. **91**, 173002 (2003).

23. R. Bingham, Nature **424**, 258 (2003).

24. S. V. Bulanov, T. Esirkepov, and T. Tajima, Phys. Rev. Lett. **91**, 085001 (2003).

25. V. I. Karpman, Plasma Phys. **13**, 477 (1971).

26. V. I. Karpman, *Non-Linear Waves in Dispersive Media* (Nauka, Moscow, 1973; Pergamon Press, Oxford, 1975).

27. D. D. Tskhakaia, Phys. Rev. Lett. **48**, 484 (1982).

28. S. Tzortzakis, L. Sudrie, M. Franco, *et al.*, Phys. Rev. Lett. **87**, 213902 (2001).

29. V. N. Kondratyev, Phys. Rev. Lett. **88**, 221101 (2002).

30. T. Piran, Phys. Rep. **314**, 575 (1999).

Numerical Investigation of Logarithmic Corrections in Two-Dimensional Spin Models[¶]

B. Berche[1] and L. N. Shchur[1, 2]

[1] Laboratoire de Physique des Matériaux, UMR CNRS 7556, Université Henri Poincaré,
F-54506 Vandoeuvre les Nancy Cedex, France
[2] Landau Institute for Theoretical Physics, Russian Academy of Sciences,
Chernogolovka, Moscow region, 142432 Russia
Received January 20, 2004

The analysis of correlation function data obtained by Monte Carlo simulations of the two-dimensional four-state Potts model, *XY* model, and self-dual disordered Ising model at criticality are presented. We study the logarithmic corrections to the algebraic decay exhibited in these models. A conformal mapping is used to relate the finite-geometry information to that of the infinite plane. Extraction of the leading singularity is altered by the expected logarithmic corrections, and we show numerically that both leading and correction terms are mutually consistent. © 2004 MAIK "Nauka/Interperiodica".

PACS numbers: 05.50.+q; 75.10.Hk

A second-order phase transition occurs at very special points in the parameter space of a model, i.e., at a fixed point of the renormalization equations. The eigenvalues of the linearized renormalization equations define the scaling dimensions of the corresponding directions related to the scaling fields. Positive eigenvalues are associated to relevant scaling fields, while negative ones correspond to irrelevant fields. In some cases, there may exist a line of fixed points along which critical exponents are varying. This occurs when a marginal field (with vanishing scaling dimension) is identified in the model. The scaling dimensions completely characterize the critical properties of the model, e.g., the power laws of the physical quantities. As an example, the correlation functions exhibit an algebraic decay at the fixed point, e.g., for a scaling field density $\phi(\mathbf{r})$,

$$G_\phi(\mathbf{r}_1, \mathbf{r}_2) = \langle \phi(\mathbf{r}_1)\phi(\mathbf{r}_2) \rangle \sim |\mathbf{r}_1 - \mathbf{r}_2|^{-\eta_\phi} \qquad (1)$$

in two dimensions (η_ϕ should be replaced by $d - 2 + \eta_\phi$ in arbitrary dimension). In some special cases, this simple behavior is modified by multiplicative logarithmic terms,

$$G_\phi(\mathbf{r}_1, \mathbf{r}_2) \sim |\mathbf{r}_1 - \mathbf{r}_2|^{-\eta_\phi} \times \ln^{\theta_\phi} |\mathbf{r}_1 - \mathbf{r}_2|. \qquad (2)$$

This situation occurs at the end of a line of fixed points or when the system is perturbed by a marginally irrelevant operator. Examples in two dimensions are given by a four-state Potts model, *XY* model, or disordered Ising model.

[¶] This article was submitted by the authors in English.

In the case of the *q*-state Potts model (from now on, we consider the case of the two-dimensional problem only), discrete spin variables $\sigma_w = 1, 2\ldots q$ are located at the sites *w* of a square lattice (μ specifies the unit lattice vector in the two directions) and interact with nearest neighbors,

$$-\frac{H_q}{k_B T} = K \sum_w \sum_\mu \delta_{\sigma_w, \sigma_{w+\mu}}. \qquad (3)$$

The value of the number of states per spin, *q*, can be seen as a parameter of the model. The special case $q \longrightarrow 1$ corresponds to the percolation problem and exhibits a second-order phase transition. The value $q = 2$ corresponds to the Ising model, so when *q* varies, the universality class changes. The transition is of second order as long as $q \leq 4$, and the value $q = 4$ coincides with the end of the line of fixed points. Along this line, the exponent of the *order parameter correlation function* varies, according to [1],

$$\eta_\sigma = \frac{(m + 3)(m - 1)}{4m(m + 1)}, \qquad (4)$$

where the value of $m = \pi / \cos^{-1}\left(\frac{1}{2}\sqrt{q}\right) - 1$ parametrizes the number of states. At $q = 4$, the correlation function exponent takes the value $\eta_\sigma(q = 4) = 1/4$. Above $q = 4$, the transition becomes of first order. The transition temperature of the 2D Potts model is exactly known from duality requirements [2], $K_c = \ln(1 + \sqrt{q})$.

The two-dimensional classical *XY* model is another example of such a scenario, although the transition is in its very nature quite different. The Hamiltonian now

describes the interaction of classical two-dimensional unit spins, $\sigma_w = (\cos\theta_w,\ \sin\theta_w)$,

$$-\frac{H_{XY}}{k_B T} = K \sum_w \sum_\mu \sigma_w \sigma_{w+\mu}. \tag{5}$$

At low temperature, as a consequence of the Mermin–Wagner–Hohenberg theorem [3], there is no finite macroscopic magnetization, but the spin–spin correlation function decays algebraically in the so-called quasi-long-range-ordered phase. The temperature plays the role of a marginal field, and the decay exponent η_σ continuously increases up to a limiting value $\eta_\sigma(XY) = 1/4$ at a transition temperature named after Berezinskii–Kosterlitz–Thouless (BKT) [4]. In this low-temperature critical phase, ordering is prevented by collective excitations, spin waves, and localized excitations, vortices, which appear in increasing number as the temperature is increased. These latter topological defects are bounded in pairs, and the transition to a completely disordered phase with exponential decay of the correlations is reached at the BKT temperature when unbinding of the pairs occurs [5]. The BKT transition thus corresponds to the end of a continuous line of fixed points in the low-temperature phase. The transition temperature $K_c \simeq 0.893$, as well as the expression of the temperature dependence of the exponent η_σ, is not known exactly. The mechanism of the transition may also be understood from the role of the vortex chemical potential. It is a relevant variable in the low-temperature phase, which becomes marginally irrelevant at the BKT transition, thus producing the essential singularities and the logarithmic corrections.

A third example is provided by the random bond Ising model in two dimensions. According to Harris criterion [6], quenched disorder is a relevant variable when the specific heat exponent of the pure system under consideration is positive. In this case, a new fixed point leading to a new universality class is expected. In the case of the 2D Ising model, since $\alpha = 0$ in the pure model, randomness is only a marginal variable which could either produce a continuous variation of the exponents with the amplitude of disorder or logarithmic corrections to the unchanged leading critical behavior if the disorder is eventually marginally irrelevant. After an interesting debate in the 1980s [7], the second scenario has been recognized to be correct [8] and the correlation function exponent keeps its value $\eta_\sigma(\text{RBIM}) = 1/4$. The Hamiltonian is the one given in Eq. (3), with $q = 2$ and with random nearest neighbor interactions $K_{w,\mu}$ along the bonds between sites w and $w + \mu$. When these couplings are taken from a binary probability distribution with equal probabilities for both strengths,

$$\mathcal{P}[K_{w,\mu}] = \frac{1}{2} \prod_{w,\mu} [\delta(K_{w,\mu} - K_1) + \delta(K_{w,\mu} - K_2)],$$ the

critical temperature follows from duality, $(\exp(K_1^c) - 1)(\exp(K_2^c) - 1) = q\ (= 2\ \text{here})$.

All these models have the common property that the order parameter correlation function G_σ is expected, from renormalization group arguments, to behave, according to Eq. (2), with $\theta_\sigma = 1/8$ (XY model) and $-1/8$ (Potts model and RBIM) [8–10]. One may then define a local effective exponent $\eta_{\text{eff}}(r)$ ($r = |\mathbf{r}_1 - \mathbf{r}_2|$),

$$\eta_{\text{eff}}(r) = -\frac{d\ln G_\sigma(r)}{d\ln r} = \eta_\sigma - \frac{\theta_\sigma}{\ln r}. \tag{6}$$

To make this formula more explicit, let us set some typical numbers. Suppose that we want to produce numerical simulations in order to check Eq. (2) with, let us say, a relative accuracy of $\Delta\eta/\eta_\sigma = |\theta_\sigma|/\eta_\sigma \ln r = 10^{-2}$. The exponent $|\theta_\sigma|$ might be estimated to be of the order of the value of η_σ, so that one has to reach values of r as large as $r \simeq \exp((\Delta\eta/\eta_\sigma)^{-1}) \simeq 10^{43}$! Even with a value of $|\theta_\sigma| = 1/8$, one still needs a sample much larger than $L > 10^{21}$ in order to reach distances between spins which are large enough to become sensitive to the presence of the log in Eq. (2). This is definitely not possible, and that might be the reason why it was almost impossible to produce reliable data[1] to corroborate Eq. (2). The strategy is thus to accept the leading behavior (the value of η_σ as predicted by RG) and to extract the value of θ_σ. This is also a difficult route, and contradictory results were reported in the literature. In the case of the XY model for example, fixing $\eta_\sigma = 1/4$ and using Monte Carlo simulations (susceptibility and correlation length data), Kenna and Irving [11] reported a value close to $\theta_\sigma \simeq 0.046(20)$, Janke [12] obtained $\theta_\sigma \simeq 0.054(2)$ from data at criticality, or $\theta_\sigma \simeq -0.112(4)$ using high-temperature data. Also with high-temperature data, Patrascioiu and Seiler [13] obtained $\theta_\sigma \simeq -0.154(92)$ and, from strong coupling expansion, Campostrini *et al.* [14] had results depending on the lattice symmetry, $\theta_\sigma \simeq -0.090(6)$ to $-0.084(12)$.[2] There are even more controversial results reported by Balog *et al.* [15], who suggest $\theta_\sigma = 0$ plus additive corrections, or Kim [16], who is in favor of ordinary scaling rather than essential singularities. We are not aware of any direct verification of the presence of logarithmic terms directly in the correlation function in the case of the four-state Potts model or disordered Ising model, but logarithmic terms have been found to be compatible with finite-size scaling data of susceptibility and specific heat [17] in the four-state Potts model and in the random bond Ising model [18].

There are conceptual difficulties with the above-mentioned approach applied to numerical simulations. First, the maximum available linear extent of a lattice is of the order of $L = 10^3$, and due to boundary effects, only a fraction (let us say, one-fourth of the lattice) can be used. As a consequence, the value of η_σ is strongly

---

[1] Both by simulations and by series expansions.
[2] In the literature, θ_σ is often referred to as $-2r$.

altered by the log correction in Eq. (6).[3] Keeping a fixed $\eta_\sigma = 1/4$ means that we attribute all the deviation of numerical data to the existence of θ_σ, but again, this correction is only an effective one, since the log term in the correlation function (2) is only the first of a series and the next term (see, e.g., [10, 17]) will affect in a similar manner the value of θ_σ and make it an effective one.[4] A second objection comes from the appearance of a typical length scale, which has a strong influence on the correction to scale-invariant behavior. Usually, one does not have to take into account the unit length, since the physical quantities exhibit scale invariance at criticality. Strictly speaking, this is no longer true when a correction to scaling (e.g., a logarithm) is present, and the above expressions for the correlation functions should be rewritten with respect to some scale factor a. This factor is related to the lattice spacing, but as to some physics of the problem, like the size of vortex pairs in the *XY* model or the typical disorder length in the RBIM, it is thus nonuniversal and depends on the model. The local exponent becomes

$$\eta_{\text{eff}}(r) = \eta_\sigma - \frac{\theta_\sigma}{\ln r/a}. \quad (7)$$

What is important to notice here is the fact that the value of a determines the amplitude of variations of the effective exponent $\eta_{\text{eff}}(r)$. According to these observations, it is probably already a good result to only predict a correct sign for the correction exponent θ_σ, and we have no stronger ambition in this paper.

We propose a different approach, which is almost free from boundary effects and enables us to work with the asymptotic expression of the correlation function in the infinite plane. The simulations[5] are performed inside a finite system, but the functional expression of the correlation function inside such a system is predicted by a convenient conformal mapping. This method has been applied with success to magnetization profiles in the case of the pure *XY* model [19] and was extensively used in the case of disordered Potts models [20] in two dimensions, where it was shown to provide quite accurate results. More problematic is the fact that we apply a method which is known to be valid at a really scale-invariant fixed point, i.e., in the absence of corrections to scaling which break (at the correction level) dilatation symmetry. In the following, we consider systems of reasonable sizes (L up to 256); the asymptotic regime $r \longrightarrow \infty$, $G_\sigma(r) \sim r^{-\eta_\sigma}$, is thus far

---

[3] With $\theta_\sigma = \pm 1/8$ and simulations available up to relative distances as large as $r = 500$, one can at most reach values of η_σ in the range 0.23–0.27.

[4] Using the expression $G(r) \times r^{1/4} \sim \ln^{1/8} r \times \left(1 + \frac{1}{16}\frac{\ln \ln r}{\ln r}\right)$ given in [10] for the BKT transition and again with $r \simeq 500$, we get $\theta_\sigma(r) = \theta_\sigma + \frac{1}{16}\frac{1 - \ln \ln r}{\ln r + (\ln \ln r)/16} \simeq 0.117$.

[5] Standard Wolff cluster algorithms.
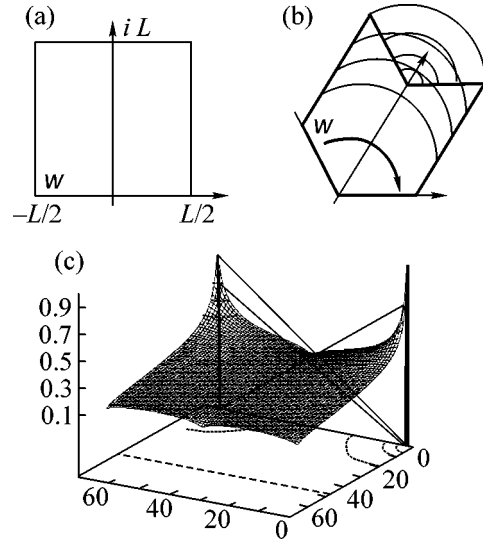
Fig. 1. (a) Conformal mapping of the infinite complex plane inside a square w; (b) sketch which shows how the boundary conditions (BCs) follow from the folding ("pillow" geometry); (c) example of the profile of the correlation function between the upper right corner and other points in the square with these particular BCs.

from being reached and the variable $\ln r$ only varies within a narrow range. Accordingly, Eq. (2) might be replaced by an algebraic decay with an effective exponent, $G_\sigma(r) \sim r^{-\eta_{\text{eff}}}$, and displays scale invariance, at least in the range of distances under consideration.

The upper complex plane $\Im m\,\zeta \geq 0$ is mapped inside a square $-L/2 \leq \Re e\,w \leq L$, $0 \leq \Im m\,w \leq L$ through the Schwarz–Christoffel conformal mapping $\zeta = \text{sn}(2Kw/L)$.

In order to relate this finite geometry to an original infinite plane (with complex variable z), one may use the Schwarz transformation $\zeta = z^{1/2}$, which has the effect of a folding of opposite edges of the square 2×2 [21], as shown in Fig. 1.
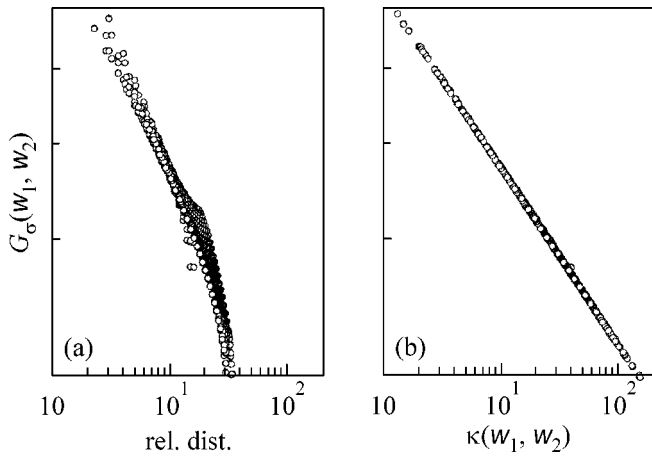
There, the effect of the conformal mapping,

$$G_\sigma(w_1, w_2) \sim |w'(z_1)|^{-\frac{1}{2}\eta_\sigma}|w'(z_2)|^{-\frac{1}{2}\eta_\sigma} G_\sigma(z_1, z_2), \quad (8)$$

is just to define a rescaled distance variable, called $\kappa(w_1, w_2)$, in terms of which one recovers inside the square with these special boundary conditions a simple power law for the correlation function:

$$G_\sigma(w_1, w_2) \sim [\kappa(w_1, w_2)]^{-\eta_{\text{eff}}}, \quad (9)$$

$$\kappa(w_1, w_2) = |w'(z_1)|^{\frac{1}{2}}|w'(z_2)|^{\frac{1}{2}}|z_1 - z_2|, \quad (10)$$

Fig. 2. (a) Log–log plot of the correlation function $G_\sigma(w_1, w_2)$ of the *XY* model vs. the relative distance in the original square geometry for a system of size 32^2; (b) the same data plotted now vs. the rescaled relative distance $\kappa(w_1, w_2)$.

Fig. 3. Log–log plot of the correlation function inside the square, $G_\sigma(w_1, w_2)$ as a function of the convenient rescaled variable $\kappa(w_1, w_2)$ (for sizes from $L = 32$ to $L = 256$ for the three models under consideration).
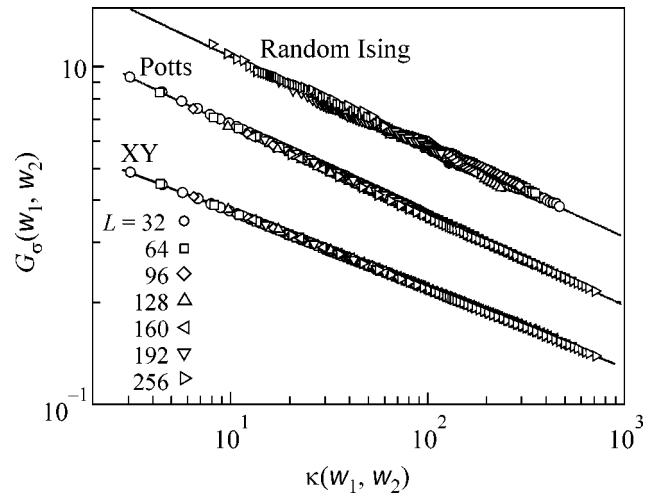
where

$$|w'(z)| = \frac{L}{4K}|\text{cn}(3Kw/L)\text{dn}(2Kw/L)\text{sn}(3Kw/L)|^{-1}$$

and $G_\sigma(z_1, z_2)$ is the correlation function in the plane (with $z = \text{sn}^2(2Kw/L)$). Here, cn$x$, dn$x$, and sn$x$ are the Jacobi elliptic functions, L is the linear size of the lattice, and $K \simeq 1.58255$ is a constant related to the aspect ratio of the system.

The main advantage of this technique is that one lattice size L is, in principle, sufficient (provided it is large enough), since the shape effects are included in the conformal mapping and the method is not very sensitive to finite-size effects. The effect of discretization of the lattice is only apparent at the scale of a few lattice spacings. One more advantage is the fact that all the information encoded in the correlation function is used, since *all* the points w inside the square enter the fit (see Fig. 2). Now, as we noticed above, it is necessary to take into account the existence of the logarithmic term if we want to understand the leading singularity. In order to emphasize this comment, let us discuss briefly

Values of the effective exponents deduced from fits of the curves shown in Figs. 3 and 4. In the case of the RBIM, the value of B_1/B_0 is roughly three times larger than for the Potts model (same sign) but strongly fluctuating

L	η_{eff}			$\theta_\sigma/\ln(a^{-1})$	
	XY	Potts	RBIM	*XY*	Potts
64	0.231	0.268	0.259	0.0087	–0.0075
128	0.233	0.266	0.287	0.0077	–0.0081
256	0.234	0.260	0.255	0.0072	–0.0074

the results presented in Fig. 3 for $L = 32$ to 256 in the case of *XY*, four-state Potts, and random bond Ising models. We show the log–log plot of $G_\sigma(w_1, w_2)$ with respect to the rescaled distance $\kappa(w_1, w_2)$ for the three models under consideration. One observes the remarkable linear regime (on this log–log scale) over the whole range of variables and, in particular, no boundary effects, as these were included in the conformal mapping. Nevertheless, while the expected slopes should all be equal to the same $\eta_\sigma = 1/4$, a deviation from this value is suspected. Then, a power law fit leads to leading singularities with exponents[6] $\eta_{\text{eff}}(XY) \simeq 0.233(3)$, $\eta_{\text{eff}}(PM) \simeq 0.264(6)$, and $\eta_{\text{eff}}(RBIM) \simeq 0.265(14)$ (there is a slight variation, depending on the size). All these results are in poor agreement with the exact result 1/4. This is clear evidence that the logarithmic correction has to be taken into account.

Figure 4 shows a semilog plot of the *rescaled* correlation function $f(|z_{12}|) = G_\sigma(w_1, w_2) \times [\kappa(w_1, w_2)]^{\eta_\sigma}$ against the relative distance $|z_2 - z_1|$ in the infinite plane geometry. One observes empirically that the expected behavior $f(|z_{12}|) \sim A(\ln(|z_{12}|/a))^{\theta_\sigma}$ according to Eq. (2) is in fact linear in this scale; that is,

$$f(|z_{12}|) \sim B_0 + B_1 \ln|z_{12}|. \tag{11}$$

This is coherent with the logarithmic correction provided that the dimensionless inverse typical length scale a^{-1} is larger than any of the accessible relative dimensionless distances at the sizes available, $a^{-1} \gg$

---

[6] Statistics over the seven values of size L for each model.
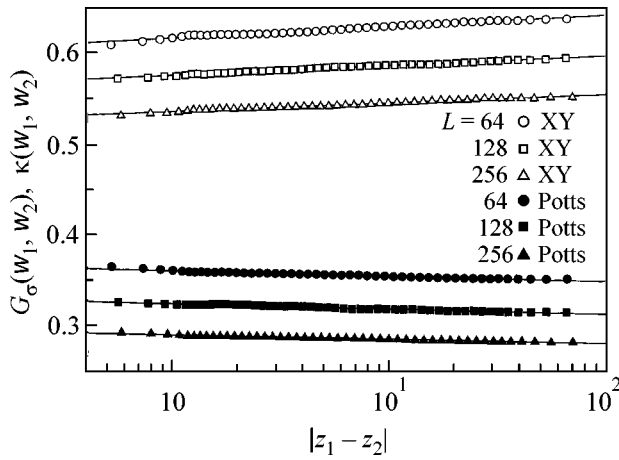
Fig. 4. Semilog plot of the rescaled correlation function for *XY* and Potts models vs. relative distance in the plane geometry ($L = 256$). The slope B_1 is positive for *XY* model and negative in the four-state Potts model.

max$|z_{12}|$. Under these conditions, the logarithmic correction yields

$$f(|z_{12}|) \sim A(\ln(a^{-1}))^{\theta_\sigma}\left(1 + \frac{\theta_\sigma}{\ln(a^{-1})}\ln|z_{12}|\right), \quad (12)$$

i.e., θ_σ appears in the ratio $B_1/B_0 = \theta_\sigma/\ln(a^{-1})$. The slope B_1 in Eq. (11) is positive if $\theta_\sigma > 0$ and negative otherwise.

As we have mentioned previously, the accessible lattice sizes are too small, so that we do not expect any precise determination of the correction exponent θ_σ. More dramatic is the fact that the θ_σ exponent appears in our expressions mixed with the nonuniversal length scale a from which a reliable value would hardly be extracted. Nevertheless, what is shown in Fig. 4 is that a logarithmic correction is consistent with the data for both *XY* and four-state Potts models, that the signs of the exponents of the log terms are opposite for both models, and that their absolute values are quite close to each other (see the table). In the case of the disordered Ising model, a quantitative analysis is made difficult due to the fluctuations introduced by the disorder average, but the leading exponent η_{eff} was compatible with a negative correction exponent θ_σ, as expected.

REFERENCES

1. M. P. M. den Nijs, J. Phys. A **12**, 1857 (1979); B. Nienhuis, J. Phys. A **15**, 199 (1982); Vl. S. Dotsenko and V. A. Fateev, Nucl. Phys. B **240** (12), 312 (1984).

2. F. Y. Wu, Rev. Mod. Phys. **54**, 235 (1982).

3. N. D. Mermin and H. Wagner, Phys. Rev. Lett. **22**, 1133 (1966); P. C. Hohenberg, Phys. Rev. **158**, 383 (1967).

4. V. L. Berezinskiĭ, Zh. Éksp. Teor. Fiz. **59**, 907 (1970) [Sov. Phys. JETP **32**, 493 (1971)]; J. M. Kosterlitz and D. J. Thouless, J. Phys. C **6**, 1181 (1973); J. M. Kosterlitz, J. Phys. C **7**, 1046 (1974).

5. J. Villain, J. Phys. (Paris) **36**, 581 (1975); J. M. Kosterlitz and D. J. Thouless, Prog. Low Temp. Phys. **78**, 371 (1978); C. Itzykson and J. M. Drouffe, *Statistical Field Theory* (Cambridge Univ. Press, Cambridge, 1989), Vol. 1; J. L. Cardy, *Scaling and Renormalization in Statistical Physics* (Cambridge Univ. Press, Cambridge, 1996).

6. A. B. Harris, J. Phys. C **7**, 1671 (1974).

7. Vl. S. Dotsenko and Vik. S. Dotsenko, Adv. Phys. **32**, 129 (1983).

8. R. Shankar, Phys. Rev. Lett. **58**, 2466 (1987); **61**, 2390 (1988); A. W. W. Ludwig, Phys. Rev. Lett. **61**, 2388 (1988); B. N. Shalaev, Phys. Rep. **237**, 129 (1994).

9. J. L. Cardy, M. Nauenberg, and D. J. Scalapino, Phys. Rev. B **22**, 2560 (1980).

10. D. J. Amit, Y. Y. Goldschmidt, and G. Grinstein, J. Phys. A: Math. Gen. **13**, 585 (1980).

11. R. Kenna and A. C. Irving, Phys. Lett. B **351**, 273 (1995); A. C. Irving and R. Kenna, Phys. Rev. B **53**, 11568 (1996).

12. W. Janke, Phys. Rev. B **55**, 3580 (1997).

13. A. Patrascioiu and E. Seiler, Phys. Rev. B **54**, 7177 (1996).

14. M. Campostrini, A. Pelissetto, P. Rossi, and E. Vicari, Phys. Rev. B **54**, 7301 (1996).

15. J. Balog, J. Phys. A **34**, 5237 (2001); J. Balog, M. Niedermeier, F. Niedermeyer, *et al.*, Nucl. Phys. B **618**, 315 (2001).

16. J. K. Kim, Phys. Lett. A **223**, 621 (1996).

17. J. Salas and A. D. Sokal, J. Stat. Phys. **88**, 567 (1997).

18. J. S. Wang, W. Selke, Vl. S. Dotsenko, and V. B. Andreichenko, Europhys. Lett. **11**, 301 (1990).

19. I. Reš and J. Straley, Phys. Rev. B **61**, 14425 (2000); B. Berche, Phys. Lett. A **302**, 336 (2002); B. Berche, A. I. Fariñas Sanchez, and V. R. Paredes, Europhys. Lett. **60**, 539 (2002); B. Berche, J. Phys. A **36**, 585 (2003).

20. B. Berche and C. Chatelain, cond-mat/0207421.

21. T. W. Burkhardt and B. Derrida, Phys. Rev. B **32**, 7273 (1985).

Anomalous Character of the Interaction of C_{60} Molecules with the Sulfur-Saturated Ta(100) Surface

N. R. Gall'*, E. V. Rut'kov, and A. Ya. Tontegode

Ioffe Physicotechnical Institute, Russian Academy of Sciences, St. Petersburg, 194021 Russia
*e-mail: gall@ms.ioffe.rssi.ru
Received January 30, 2004

It is shown that, contrary to all previously studied systems, heating to ~800 K in the C_{60}–TaS_2 monolayer–Ta(100) adsorption system leads to the complete removal of the deposited fullerene molecules. A model is proposed that explains the observed phenomenon by a very weak nonchemisorption interaction between the C_{60} molecules and the valence-saturated surface of tantalum disulfide that forms layered crystals with van der Waals interaction between layers. © *2004 MAIK "Nauka/Interperiodica"*.

PACS numbers: 68.43.Fg; 61.46.+w

Fullerenes are high-symmetry, pure carbon molecules of composition C_{60}, C_{70}, etc. The best known representative of this class—C_{60} molecule—has a spherical form. Along with nanotubes and two-dimensional graphite films, fullerenes are the most important representatives of the family of low-dimensional carbon nanomaterials, which are considered to be highly promising, in particular, as materials for nanoelectronics [1]. Even nowadays, fullerenes have highly diversified actual or potential applications, from medicines to the components of nuclear explosive devices [2, 3].

The use of fullerenes in virtually any sorts of physical technologies implies their interaction with solids, and any such process starts with the surface. By now, the interaction of C_{60} molecules with atomically pure surfaces of many metals (W, Ir, Re, Mo, Ag, Cu, …) [4–11] and semiconductors (Si, SiC) [12] has been studied and described. However, very little is known about their adsorption on film systems. In all previously studied systems, C_{60} molecules of the second and subsequent monolayers leave the surface upon heating at temperatures of 700–850 K. However, molecules of the first adsorption monolayer remain on the surface at such heating. They undergo fragmentation upon further rise in temperature and, next, dissociate into atoms in the temperature range 1000–1300 K because of the catalytic action of the metal or semiconductor surface, contaminating the surface and bulk of the sample with carbon. From both scientific and practical points of view, it is of interest to seek out a system that permits its surface to be completely cleaned of fullerenes.

Experiments were performed on a high-resolution Auger spectrometer, described in [13], under ultrahigh vacuum (UHV) conditions (p ~ 10^{-10} Torr). There was a possibility of recording Auger peaks directly from heated samples in the range 300–2100 K. The samples were directly heated tantalum strips $(0.05 \times 1 \times 40)$ mm in size with the (100) face on the surface. These strips were cleaned successively by heating in oxygen (P_{O2} ~ 10^{-6} Torr, t ~ 3 h) and heating at T ~ 2500 K in UHV for several hours. After cleaning, only the tantalum Auger peaks were observed on the surface, and the surface was uniform in work function. The Auger signals of sulfur with $E = 150$ eV, silicon with $E = 92$ eV, carbon with $E = 269$ eV, and tantalum (triplet) with $E = 160$–170 eV were used.

Fullerenes were deposited on the entire strip surface from a Knudsen cell, as described in [14]. After pretreatment, the cell provided a stable and easily controlled flow of fullerene molecules with a density of $\nu = 10^{10}$–10^{13} cm^{-2} s^{-1}. The determination of the absolute amount of adsorbed fullerenes was carried out by the method described in the same work. In order to distinguish between the fullerenes adsorbed on the surface and other possible carbon states and to determine the chemical state of the adsorbed C_{60} molecules, we used the specific C_{KVV} shape of the Auger peak with $E = 269$ eV, as we proposed in [5]. Sulfur was deposited onto the tantalum surface by the chemical vapor deposition (CVD) technique from H_2S molecules. At $T > 600$ K, hydrogen sulfide molecules dissociate, hydrogen is desorbed, and sulfur remains in the adsorption layer [15].

The interaction of C_{60} molecules with pure tantalum was preliminarily studied. The processes proceeding in this case are similar to those described in [5] for the W(100) surface: the fullerenes adsorbed on the pure surface undergo transformation already at room temperature, as is seen from the essentially nonfullerene shape of their C_{KVV} Auger spectrum (Fig. 1, spectrum *1*). However, the molecules of the second and subsequent layers retain their electronic structure. This fact, evi-

dently, indicates that these molecules also retain their structure in the adsorption layer (Fig. 1, spectrum *2*). The fullerite film grows according to a layer-by-layer mechanism. The C_{60} molecules of the first layer screen the substrate Auger signal by a factor of ~2.7, and the molecules of the second and subsequent layers screen it by a factor of ~3. Using the data [7] for fullerene adsorption on Mo(100) and considering that the screening conditions for the Auger signals from the tantalum and molybdenum substrates are close to each other (the energies of the corresponding Auger electrons differ by less than 5%), we can estimate the concentration of the adsorbed molecules: it is N_{c60} ~ 1.5×10^{14} cm^{-2} in the first layer and ~1.6×10^{14} cm^{-2} in the second and subsequent layers. Heating to 700 K leads to the removal of all the deposited molecules from the surface, apart from those in the first and partially second layers. By estimate, the total amount of molecules remaining on the surface equals ~6×10^{14} cm^{-2}. Upon further heating, these molecules dissociate into carbon atoms, which dissolve in the sample bulk at T ~ 900 K, and only surface carbide remains on the surface with the concentration of carbon atoms N_C ~ 3×10^{14} cm^{-2} [16] (Fig. 3, spectrum *3*).

Doping the surface with atoms of three nonmetals (carbon, silicon, and sulfur) up to the formation of the corresponding surface compounds, having concentrations of N_S ~ 9×10^{14} cm^{-2} and N_{Si} ~ 9×10^{14} cm^{-2} for the two latter adsorbates [17], does not lead to any noticeable changes in the adsorption properties of the surface. However, as the exposure of the sample to hydrogen sulfide vapor increases (T ~ 1100 K, P_{H2S} ~ 10^{-7} Torr, and $t > 120$ s), a new stable coating is formed. This coating is characterized by the ratio $I_S/I_{Ta} = 4.2$ of sulfur Auger peak to tantalum Auger peak, and this ratio remains unchanged under further holding in H_2S vapor. The interaction of fullerene molecules with this coating changes drastically and becomes unusual in character. First, even at the very early adsorption stages, the C_{60} molecules on the obtained coating retain their primordially inherent shape of carbon Auger line, indicating that they retain their fullerene nature (Fig. 1, spectrum *4*). Second, the regularities of the initial stages of fullerite-film growth change radically. An analysis of the variation of the adsorbate (carbon) and substrate (tantalum and sulfur) Auger intensities performed according to the procedure proposed in [18] indicates that the layer-by-layer film-growth mechanism transforms to a rather uncommon Volmer–Weber mechanism, that is, to the formation of fullerite islands directly on the substrate without an intermediate adsorbate monolayer.

Figure 2a presents the variation of the adsorbate and substrate Auger signals upon heating a fullerite film grown on this film system. It is seen that heating to 800 K leads to a drop in the carbon Auger signal to zero, while the sulfur and tantalum Auger signals are
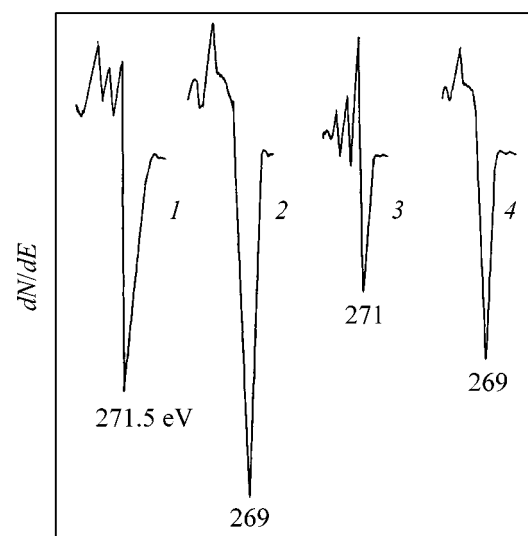
Fig. 1. Carbon Auger spectra from various adsorption states of C_{60} molecules on tantalum and on a TaS_2 monolayer: (*1*) approximately one fullerene monolayer on Ta(100), (*2*) ~ four fullerene monolayers on Ta(100), (*3*) surface carbide, (*4*) fullerenes deposited up to a concentration of ~1.5×10^{14} on TaS_2 (the spectrum intensity is doubled).
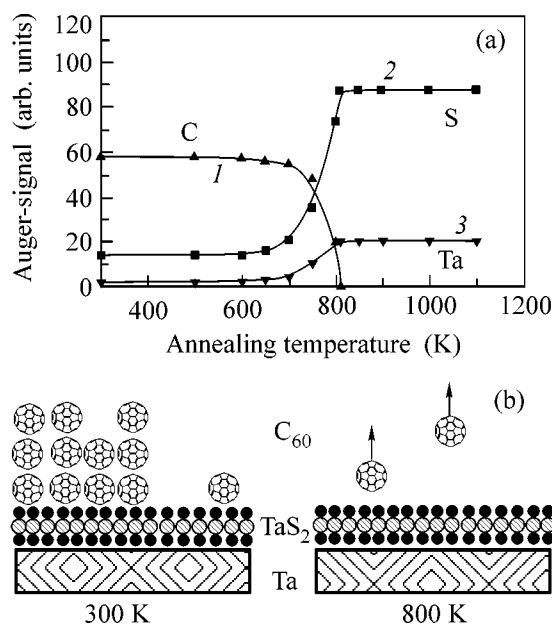
Fig. 2. Transformation of a fullerite film deposited at room temperature over a TaS_2 monolayer grown on Ta(100) upon stepped film annealing with a step of 50 K. The time of annealing at each temperature point was 15 s. (a) Variations of the (*1*) carbon, (*2*) sulfur, and (*3*) tantalum Auger signals; (b) the scheme of the process. The curve for carbon is given on the scale extended two times along the vertical axis.

restored to their initial values. This means that the *complete* desorption of C_{60} molecules occurs at this temperature, whereas the surface remains unchanged after the

fullerene adsorption–desorption procedure. It is worth noting that this is the only system that we know at present in which the complete desorption of fullerenes has been reliably validated.

A conjectural scheme of the processes that proceed upon heating the system under consideration is shown in Fig. 2b. The adsorption of hydrogen sulfide at $T = 1100$ K likely leads to the formation of a valence-saturated monolayer of the layered TaS_2 compound, which has a structure similar to that presented in the figure and characteristic of all the transition-metal dichalcogenides [19]. In this structure, tantalum atoms are located almost in the same plane to form a one-atom-thick layer and sulfur atoms cover this layer on both sides. The intensities of the sulfur and tantalum Auger signals calculated within the framework of this model coincide very well (to an accuracy of ~15%) with the values measured experimentally. The fact that the intensities of the sulfur and tantalum Auger signals do not vary with a further increase in the exposure of the tantalum sample to hydrogen sulfide presumably indicates that the newly adsorbed hydrogen sulfide molecules cease to dissociate on the valence-saturated disulfide surface and sulfur ceases to enter the adsorption layer. The fullerene molecules also retain their structure on such a layer, because it protects them against the catalytic action of the metal surface, while these molecules themselves are bound to the disulfide surface by weak intermolecular forces. This also explains the possibility of complete desorption of fullerenes: the molecules of even the top monolayer do not form strong chemisorption bonds with the substrate, which could prevent their thermal desorption.

Thus, contrary to all earlier observations, an adsorption system has been found that allows the complete removal of C_{60} molecules from the surface by thermal desorption. This system is a tantalum disulfide monolayer film grown on Ta(100). Apparently, this valence-saturated film protects the adsorbed fullerene molecules against the catalytic action of the metal surface. The C_{60} molecules do not form strong chemisorption bonds with this surface, as a result of which these molecules do not decompose upon heating but thermally desorb from the surface.

REFERENCES

1. Yu. E. Lozovik and A. M. Popov, Usp. Fiz. Nauk **167**, 751 (1997) [Phys. Usp. **40**, 717 (1997)].

2. P. Trouillas, B. Ratier, A. Moliton, and J. L. Duroux, Fullerene Sci. Technol. **4**, 1299 (1996).

3. N. R. Gall, Phys. Lett. B **560**, 161 (2003).

4. Hang Xu, D. M. Chen, and W. N. Creager, Phys. Rev. Lett. **70**, 1850 (1993).

5. N. R. Gall, E. V. Rut'kov, and A. Ya. Tontegode, Fullerene Sci. Technol. **9**, 111 (2001).

6. N. R. Gall, E. V. Rut'kov, A. Ya. Tontegode, and M. M. Usufov, Mol. Mater. **7**, 187 (1996).

7. N. R. Gall', E. V. Rut'kov, A. Ya. Tontegode, and M. M. Usufov, Zh. Tekh. Fiz. **69** (11), 117 (1999) [Tech. Phys. **44**, 1371 (1999)].

8. Y. Z. Li, M. Chander, J. C. Partin, and J. H. Weaver, Phys. Rev. B **45**, 13837 (1992).

9. E. V. Rut'kov, A. Ya. Tontegode, and M. M. Usufov, Phys. Rev. Lett. **74**, 758 (1995).

10. P. M. Beton, A. W. Dunn, and P. Moriarty, Surf. Sci. **361–362**, 878 (1996).

11. O. K. Kin, Y. D. Suh, K. H. Park, *et al.*, J. Vac. Sci. Technol. A **11**, 1675 (1993).

12. N. R. Gall', E. V. Rut'kov, and A. Ya. Tontegode, Fiz. Tekh. Poluprovodn. (St. Petersburg) **36**, 1084 (2002) [Semiconductors **36**, 1008 (2002)].

13. N. R. Gall', E. V. Rut'kov, A. Ya. Tontegode, and M. M. Usufov, Pis'ma Zh. Tekh. Fiz. **23** (23), 26 (1997) [Tech. Phys. Lett. **23**, 911 (1997)].

14. Z. Vakar, N. R. Gall', I. V. Makarenko, *et al.*, Pis'ma Zh. Éksp. Teor. Fiz. **67**, 969 (1998) [JETP Lett. **67**, 1024 (1998)].

15. V. Maurice, J. Oudar, and M. Huber, Surf. Sci. **219**, L628 (1989).

16. N. R. Gall, E. V. Rut'kov, and A. Ya. Tontegode, Surf. Sci. **472**, 187 (2001).

17. N. R. Gall, E. V. Rut'kov, A. Ya. Tontegode, and M. M. Usufov, Phys. Low-Dimens. Semicond. Struct. **4–5**, 75 (1996).

18. C. Argile and G. E. Rhead, Surf. Sci. Rep. **10** (6/7), 277 (1989).

19. C. A. Papogorpoals, Solid State Commun. **84**, 921 (1992).

Translated by A. Bagatur'yants

Double-Peak Specific Heat Feature in Frustrated Antiferromagnetic Clusters[¶]

A. V. Syromyatnikov* and S. V. Maleyev

St. Petersburg Nuclear Physics Institute, Russian Academy of Sciences, Gatchina, 188300 Russia
*e-mail: syromyat@thd.pnpi.spb.ru
Received December 11, 2003; in final form, February 2, 2004

We study the nature of a double-peak specific heat structure in kagome clusters. A cluster containing 12 spins is considered thoroughly by means of numerical diagonalization. On the basis of analysis of exact spectra, simple models are proposed to explain the nature of the low-T peak at $T_l < \Delta$ (Δ is the spin gap) in this case and in those of larger clusters studied so far. Using these models, we show that the rapid increase in density of states just above the spin gap gives rise to the peak and clarify the weak magnetic field sensitivity of the peak. Spin susceptibility and entropy are considered as well. Our approach could be appropriate for other frustrated antiferromagnetic systems. © 2004 MAIK "Nauka/Interperiodica".

PACS numbers: 75.10.Jm; 75.40.Cx; 75.50.Ee

INTRODUCTION

A lot of both experimental and theoretical attention has been attracted to kagome and pyrochlore frustrated magnets during the last decade (see [1–14]). The specific heat C measurements in spin-3/2 kagome compound SrCrGaO revealed a peak at $T \approx 5$ K, which was almost independent of the magnetic field H up to 12 T, and $C \propto T^2$ behavior at lower T [1]. Furthermore, the uniform susceptibility χ was found to deviate from Curie–Weis law at much smaller temperatures than in nonfrustrated materials.

In order to understand qualitatively the peculiarities of these systems, a number of finite cluster diagonalization studies have been carried out [2, 4–12]. The main finding of [4–8] on kagome Heisenberg spin-1/2 clusters (the number of sites $N \leq 36$) with periodic boundary conditions is the observation of a spin gap Δ separating the singlet ground state from the upper triplet levels, a band of nonmagnetic singlet excitations being inside the gap. The number of states in the singlet band increases exponentially with the number of sites. A similar picture with many singlets inside the spin gap has been found for pyrochlore clusters [2].

Specific heat calculations of kagome clusters with $N = 12$, 18, 24, and 36 revealed two peaks, with the low-T one at temperature $T_l \lesssim \Delta$ [8–11]. At $N = 18$, 36, the low-T peak was found to be weakly H-dependent, and $C \propto T^2$ in a narrow interval below T_l [11]. It is widely accepted now that the wealth of low-lying singlet excitations is responsible for the low-T peak [10, 11] and for its weak field dependence [1, 11]. At the same time, it has been pointed out that upper triplet levels contribute to the peak as well [9, 11].

The double-peak specific heat structure is a general feature of many frustrated antiferromagnetic systems. It was observed numerically in Heisenberg spin-1/2 pyrochlore slab [12], in Δ chain [15], and in clusters of triangular lattice within the model with multispin exchange [16, 17].

In the present paper, we elaborate on the nature of the double-peak specific heat structure in Heisenberg spin-1/2 kagome antiferromagnetic clusters.

Firstly, we perform numerical diagonalization of the kagome Heisenberg spin-1/2 starlike cluster (see inset of Fig. 1). The star has the doubly degenerate singlet ground state separated from the lower triplet level by the gap Δ [14]. As is shown in [14], the lower singlet band of a kagome antiferromagnet appears naturally
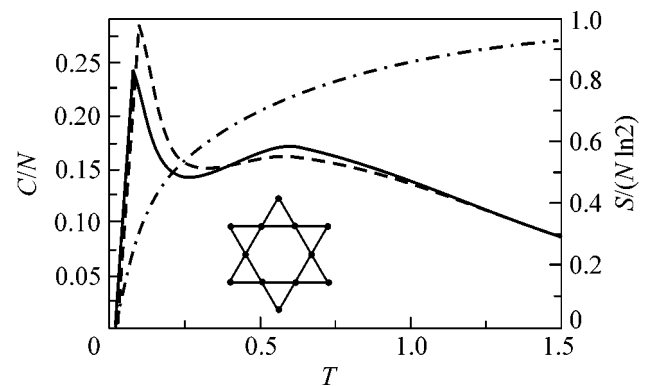
Fig. 1. Specific heat $C(T)$ per spin (solid line) and entropy $\mathcal{S}(T)$ normalized by $\mathcal{S}(\infty) = N\ln 2$ (dashed–dotted line) of the antiferromagnetic cluster with $N = 12$ shown below the curves (star). The specific heat calculated with Eq. (3) is shown by dashed line.

[¶] This article was submitted by the authors in English.

Low-lying levels of the star; they are classified by S

Energies	Number of levels		
	$S = 0$	$S = 1$	$S = 2$
–4.500000	2	0	0
–4.240331	0	1	0
–4.236220	0	2	0
–4.232400	0	2	0
–4.202448	0	1	0
–4.183814	1	0	0
–4.182320	2	0	0
–4.141850	2	0	0
–4.077928	0	1	0
–4.068850	0	2	0
–4.056472	1	0	0
–4.010310	0	2	0
–3.913465	0	1	0
–3.865010	2	0	0
–3.832691	0	1	0
–3.829460	0	0	1

from the star's degenerate ground states as a result of interstar interaction (cf. [4–8]).

Unlike clusters with periodic boundary conditions [4–11], no singlet states appear inside the spin gap in the star cluster. Nevertheless, we observe a double-peak structure of C with the low-T peak at $T_l \ll \Delta$ which possesses weak field sensitivity.

Secondly, on the basis of analysis of exact spectra obtained numerically, we propose simple models revealing the low-T peak for both star and other larger kagome antiferromagnetic clusters. All these models share the common feature of rapid increase in the density of states (DS) just above the gap. We argue that this feature is responsible for the appearance of the low-T peak. The weak magnetic field sensitivity of the peak can be understood within the framework of these models as well.

It should be stressed that our conclusions concerning the origin of the low-T peak contradict those proposed in previous works [10, 11].

We also investigate how such a behavior of the DS affects the entropy and spin susceptibility of the system.

We believe that the double-peak structure in other frustrated antiferromagnetic systems can have the same origin as the one proposed in this paper. We hope our analysis will stimulate corresponding studies.

ANALYSIS OF THE STAR

We begin with consideration of the Heisenberg spin-1/2 antiferromagnetic cluster shown in the inset of Fig. 1. The Hamiltonian has the form

$$\mathcal{H} = \sum_{\langle i, j \rangle} \mathbf{S}_i \mathbf{S}_j - H \sum_i S_i^z, \qquad (1)$$

where $\langle i, j \rangle$ denote nearest neighbors and the value of exchange constant is chosen to be unity, so the temperature T and the magnetic field H are measured in coupling constant units. We start with $H = 0$ in Eq. (1). As the Hamiltonian commutes with all projections of the total spin operator, the star levels are classified by the values of S, irreducible representations (IRs) of its symmetry group C_{6v}, and are degenerated with respect to S^z. In the basis of IRs, the matrix of the Hamiltonian has a block structure. Each block has been diagonalized numerically. Low-lying levels are presented in the table.

As is seen from the table, the star has a doubly degenerate singlet ground state separated from the lower triplet level by the spin gap $\Delta \approx 0.26$ [14]. Energies of the ground state and the upper level are –4.5 and 4.5, respectively. Importantly, within the range –4.5 + $\Delta < E \leq 4.5$, the levels are very close to each other: the distances between them are of order of 0.1–0.01 $\ll \Delta$. A part of the spectrum shown in the table reflects this feature. As is demonstrated below, this peculiarity plays the crucial role for the low-T properties of the star cluster.

Specific heat C calculated numerically with this spectrum is shown in Fig. 1. It has a double-peak structure with the low-T peak at $T_l \approx 0.085$ and high-T one at $T_h \approx 0.6$. The most intriguing feature of C is the fact that $T_l \ll \Delta$. Indeed, according to the common point of view, the specific heat of a fully gaped system should decrease exponentially with T at $T < \Delta$. Meanwhile, the exponential decay for the star cluster occurs at $T < T_l \approx \Delta/3$ only. As is demonstrated below, the low-T peak is not associated with any peak in the DS. Instead, the extremely high DS just above the gap is the origin of this behavior.

A plot of the integrated density of states (IDS) $\mathcal{N}(E)$ (the number of states with energies lower than E) is presented in Fig. 2. It is well fitted by the function $\mathcal{N}(E) = 2200 \tanh(0.39E) + 2060$. Since the distances between levels at –4.5 + $\Delta < E < 4.5$ are of the order of 0.1–0.01, one can use this function as the IDS above the gap to model the specific heat at $T \gg 0.01$. Then, the DS given by $\rho(E) = d\mathcal{N}(E)/dE$ can be approximated within the interval –4.5 + $\Delta < E < 4.5$ as follows:

$$\rho(E) = \frac{w}{\cosh^2(gE)}, \qquad (2)$$

with $w = 858$ and $g = 0.39$. In this model, C has the form

$$C = \frac{d\bar{E}}{dT} = \frac{d}{dT}\left(\frac{\int\limits_{\Delta}^{9} dE e^{-E/T} E \rho(E - 4.5)}{d + \int\limits_{\Delta}^{9} dE e^{-E/T} \rho(E - 4.5)}\right), \qquad (3)$$

where $\rho(E)$ is given by Eq. (2) and d is the degeneracy of the ground state ($d = 2$ for the star cluster). For the sake of convenience, in Eq. (3) and below, we shifted the energy scale, so the ground-state energy is equal to 0. Specific heat calculated from Eqs. (2) and (3) by numerical integration is also presented in Fig. 1. It has a double-peak structure and coincides well with that obtained with the real spectrum. Let us mention the excellent agreement between real- and model-spectrum calculations at high temperatures and the good agreement around the low-T peak. The latter appearing at $T_l \approx 0.1$ is 15% higher for the model spectrum than for the real one. This pretty good coincidence encourages us to use our model in further analysis.
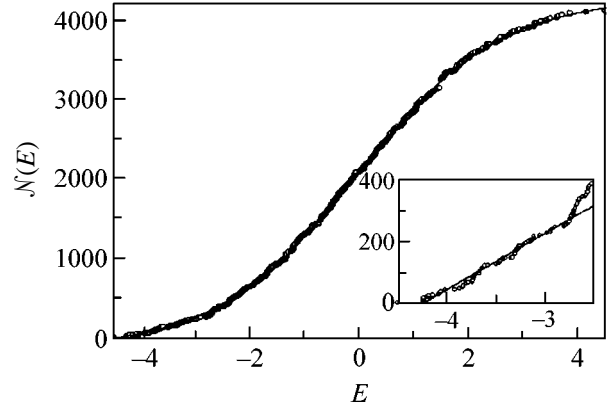
LOW-T PEAK

Let us consider in detail the specific heat at $T \lesssim \Delta$. We derive now an analytic expression for C on the assumption that $1/\Delta \gg g$, which is held for the star ($1/\Delta \approx 4$ and $g \approx 0.4$). It is easy to show using Eq. (2) that, under these conditions, one can replace $\rho(E - 4.5)$ in Eq. (3) by the constant $W \approx \rho(\Delta - 4.5) \approx 117$. Unfortunately, at low energies, Eq. (2) is not very good. As is shown in Fig. 2, the precise value of W is 180, because the real $\mathcal{N}(E)$ is well fitted by $180(E + 4.24)$ in the range $\Delta - 4.5 < E < -2.7$. As a result, at $T \lesssim \Delta$, we have from Eq. (3)

$$C = \frac{1 + Zxe^x(x^2 + 2x + 2)}{(1 + Zxe^x)^2}, \qquad (4)$$

where $x = \Delta/T$ and $Z = d/(W\Delta)$. The position of the peak T_l is determined by the condition $dC/dx = 0$, which has the form

$$Ze^x = \frac{x + 4}{x^2 + 2}. \qquad (5)$$

As follows from Eq. (5), the peak appears if $Z < Z_c \approx 2$. For the star, $Z \approx 0.04$ and numerical solution of Eq. (5) gives $T_l \approx 0.093$, which is very close to its real value, 0.085. Analysis of Eqs. (4) and (5) shows that the peak becomes smaller and T_l tends to zero as Δ decreases. At the same time, T_l becomes larger as W decreases. It can even exceed the value of Δ when W is small enough. Anyway, the peak disappears as soon as Z amounts to Z_c. Therefore, we conclude that Δ and W play the role of driving parameters responsible for the peculiar low-T behavior of the star.

Fig. 2. Integrated density of states of the star $\mathcal{N}(E)$, which is the number of states with energies lower than E. The fit is by $2200\tanh(0.39E) + 2060$. The inset shows the low-energy sector where $\mathcal{N}(E)$ is fitted by $180(E + 4.24)$.
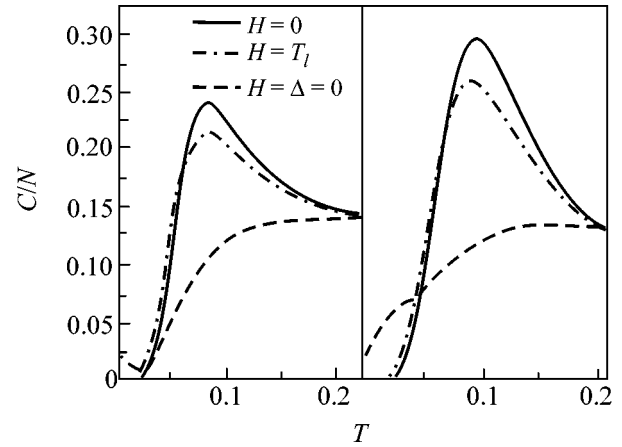
Fig. 3. Low-T peak evolution for the star in the magnetic field H obtained by numerical diagonalization of the Hamiltonian Eq. (1) (left) and by the model discussed in the text (right). In both cases, $T_l \approx \Delta/3$.

FIELD DEPENDENCE

We turn now to the discussion of how the external magnetic field H affects the low-T behavior of the specific heat C. In isotropic unfrustrated antiferromagnet, a finite-T peak in C implies the transition to the long-range ordered state. This peak could be shifted to zero and suppressed by applying external magnetic field of order of the peak temperature. In this respect, the field dependence of the star cluster at low T is also unusual. The results of our calculations of C using the exact spectrum of Hamiltonian Eq. (1) obtained numerically are presented in the left panel of Fig. 3. At $H = T_l \approx 0.085$, the peak height is reduced by only 11% and T_l is diminished negligibly. The field equal to the value of the spin gap is needed to smear out the peak.

The low-T peak evolution at $H \neq 0$ can be understood within the scheme described above. We apply the same scheme to explain the nature of the weak H sensitivity of the peak. The magnetic field splits levels with $S \neq 0$. It is clear from the table that the low-energy sector above the gap is represented mostly by triplets. So, the DS at $H < \Delta$ can be modeled as follows: it is 0 at $0 < E < \Delta - H$, the DS is $W/3$ at $\Delta - H < E < \Delta$, it is $2W/3$ at $\Delta < E < \Delta + H$, and the DS is W at $E > \Delta + H$. The corresponding results of the peak evolution with H are presented in the right panel of Fig. 3. Surprisingly, this model reproduces even quantitatively the main tendencies of the evolution (cf. left panel of Fig. 3). The field broadens the area where the drop in the DS takes place and, in so doing, it causes the peak reduction. For the change in the peak to be significant, $H \approx \Delta$ is needed. Therefore, the reason for the weak field sensitivity of the low-T peak in the star cluster is $T_l \approx \Delta/3$.

LARGER KAGOME CLUSTERS

As was mentioned above, the double-peak specific heat structure in kagome clusters with even N has been found in many previous numerical works [5, 8–11]. The height and the position of the high-T peak obtained by high-temperature expansion [10] and by finite cluster diagonalization [8–11] coincide with each other and with our results. The low-T peak at $T_l \lesssim \Delta$ was obtained in [8–11], but its position and height depended on N, the cluster form, and the calculation technique. We show now that the reason for the low-T peak appearance in those cases is similar: it is the rapid increase in the DS just above the spin gap. It will be argued that the weak field sensitivity of the low-T peak reported in [11] has the same origin as in our case.

We focus here on the largest cluster with $N = 36$ studied before. Its low-energy spectrum was obtained in [7, 8] and thermodynamic properties were discussed in [11]. Similarly to the star case, the spectrum above Δ is nearly continuous [7]. In contrast, the spin gap there is filled with singlets separated from the nondegenerate singlet ground state by a very small gap $\Delta_s \ll \Delta$. According to [7], these singlets are distributed quite uniformly and the DS is of the order of 1000. The DS above the gap is much larger than that inside it.

The nature of the low-T peak can be understood qualitatively within the model similar to that proposed above for the star. Let us assume that the DS is W' at $E < \Delta'$, where $\Delta' \gtrsim \Delta$, and there is a jump in the DS at $E = \Delta'$, so it is equal to $W \gg W'$ above Δ'. Specific heat calculation based on the analogue of Eq. (3) gives, in the interval of interest $\Delta_s \ll T \lesssim \Delta'$, the following expression:

$$
\frac{C}{=} \frac{(1 + re^x)^2 + rx^2 e^x + 2rZxe^{2x} + Zxe^x(x^2 + 2x + 2)}{(1 + re^x + Zxe^x)^2},
$$
(6)

where, now, $x = \Delta'/T$, $Z = 1/(\Delta'W)$, and $r = W'/W$. We have made an effort to reproduce the low-T peak in C/N obtained in [11] with the height of approximately 0.152 and $T_l \approx 0.05 < \Delta \approx 0.074$. Specific heat calculated with the use of Eq. (6) at $\Delta' = 0.23$, $W = 43000$, and $W' = 1000$ reveals a peak with these parameters. However, the approach is too rough to get T^2 behavior of C at $T < T_l$. Since $Z\Delta'/T_l \ll r$, the terms in Eq. (6) containing Z do not affect the low-T peak. As a result, T_l is given by the equation

$$
re^x = \frac{1}{x - 1}.
$$
(7)

It is seen from Eqs. (6) and (7) that the parameter Δ' does not affect the peak height, but it determines T_l. Evidently, T_l decreases as Δ' tends to zero. Simultaneously, the parameter r determines both the peak position and its height: the peak becomes smaller and T_l increases as r becomes larger. We conclude that the driving parameters for this model are Δ' and r. Furthermore, the states lying both above and below Δ' contribute to the low-T peak. This finding is in accordance with [11].

One can show that no other sets of parameters exist in this model which could describe the peak discussed in [11]. Indeed, since, according to [7], the DS below Δ' is equal to 1000 and $W' \ll W$, the values of Δ' and W are determined unambiguously by the low-T peak obtained in [11].

Using this model, it is easy to understand qualitatively the weak sensitivity of C to the magnetic field discussed in [11]. It has been demonstrated that, at $H = T_l \approx 0.05$, the peak height is decreased by only 10% and T_l is also decreased negligibly. It resembles the star case considered above. As the magnetic field splits levels with $S \neq 0$, the DS in the field $H < \Delta'$ will be as follows: the DS at $0 < E < \Delta' - H$ remains W', it is $W' + W/3$ at $\Delta' - H < E < \Delta'$, the DS is $2W/3$ at $\Delta' < E < \Delta' + H$, and the DS is W above $\Delta' + H$. We also assume here that the spectrum above Δ' at $H = 0$ is formed mostly by triplets. As a result of calculations of the specific heat in our model, we find that the field $H = T_l \approx 0.05$ reduces the low-T peak by 8% and slightly diminishes T_l. These findings are even in *quantitative* agreement with [11]. Furthermore, the reduction of the peak at $H = \Delta'/2$ calculated in our model is about 28%. So, we see that a field as large as $H \sim \Delta' \gg T_l$ is needed to change the low-T peak significantly.

We turn now to a brief discussion of entropy $\mathcal{S}(T)$ and spin susceptibility (SS) $\chi(T)$ of kagome clusters and sketch what peculiarities in their behavior the considered feature of the spectrum leads to.

ENTROPY

Entropy of the star cluster is presented in Fig. 1. Its temperature dependence reproduces the most charac-

teristic feature of those of larger clusters: in all cases, there is 50% of the total entropy in the low-T peak of the specific heat at $T < 0.2$ [10, 11]. It is seen from the above consideration that this peculiarity in kagome clusters stems from the rapid increase in the DS and states above Δ', which give the main contribution to $\mathcal{S}$ at $T < 0.2$. Such an entropy feature has been obtained in other models of frustrated antiferromagnets mentioned above which possessed the double-peak structure of C [16, 17].

SPIN SUSCEPTIBILITY

SS of clusters with $N = 12$ and 18 studied in [10] has one maximum at quite low temperature $T_\chi \approx 0.14 \approx \Delta/2$ and weakly depends on N. SS of the star cluster deviates slightly from those reported in [10]. As was obtained in [13], $\chi(T)$ of cluster with $N = 36$ differs significantly from $\chi(T)$ of smaller ones ($T_\chi \approx 0.045$ and the peak 50% higher). The authors of [13] attributed this effect to the increase in the DS above the gap. One can come to the same conclusion modeling $\chi(T)$ as we did above for the specific heat. Within the same approximations, we get the following expressions for SS of the star χ_s and of the cluster with $N = 36$ χ_{36}:

$$\chi_s = \frac{2}{3}\frac{1}{\Delta}\frac{x}{Zxe^x + 1} \quad \chi_{36} = \frac{2}{3}\frac{1}{\Delta'}x\frac{re^{x(1-\alpha)} + 1}{re^x + 1}, \quad (8)$$

where $\alpha = \Delta/\Delta'$. Our analysis shows that χ_s reproduces the peak nicely, whereas χ_{36} calculated with $\Delta = 0.074$ gives a peak of the right height but with $T_\chi \approx 0.065$. In both cases, the models demonstrate a stronger decrease of SS at $T \gtrsim T_\chi$ than in real-spectrum calculations. Meanwhile, they correctly pick up the interrelation between the peak characteristics and the DS properties just above the gap mentioned in [13]: the peak becomes higher and T_χ becomes smaller as Z and r decrease.

CONCLUSIONS

In this paper, we study the nature of the double-peak structure of the specific heat in kagome clusters. The starlike cluster containing 12 spins (see inset of Fig. 1) is considered thoroughly by numerical diagonalization. Simple models are proposed to explain properties of the low-T peak at $T_l < \Delta$ (Δ is the spin gap) in this case and in those of larger clusters studied so far numerically [8–

11]. We show that the rapid increase in the density of states just above the gap gives rise to the peak and explain its weak sensitivity to the magnetic field. Our consideration could be appropriate for other frustrated antiferromagnetic systems.

REFERENCES

1. A. P. Ramirez, B. Hessen, and M. Winclemann, Phys. Rev. Lett. **84**, 2957 (2000).
2. B. Canals and C. Lacroix, Phys. Rev. Lett. **80**, 2933 (1998).
3. Z. Hiroi, M. Hanawa, N. Kobayashi, *et al.*, J. Phys. Soc. Jpn. **70**, 3377 (2000).
4. P. Lecheminant, B. Bernu, C. Lhuillier, *et al.*, Phys. Rev. B **56**, 2521 (1997).
5. C. Zeng and V. Elser, Phys. Rev. B **42**, 8436 (1990).
6. P. W. Leung and V. Elser, Phys. Rev. B **47**, 5459 (1993).
7. Ch. Waldtmann, H. U. Everts, B. Bernu, *et al.*, Eur. Phys. J. B **2**, 501 (1998).
8. C. Zeng and V. Elser, Phys. Rev. B **51**, 8318 (1995).
9. V. Elser, Phys. Rev. Lett. **62**, 2405 (1989).
10. N. Elstner and A. P. Young, Phys. Rev. B **50**, 6871 (1994).
11. P. Sindzingre, G. Misquich, C. Lhuillier, *et al.*, Phys. Rev. Lett. **84**, 2953 (2000).
12. H. Kawamura and T. Arimori, Phys. Rev. Lett. **88**, 077202 (2002).
13. C. Lhuillier and P. Sindzingre, *Quantum Properties of Low-Dimensional Antiferromagnets*, Ed. by Y. Ajiro and J.-P. Boucher (Univ. Press, Kyushu, 2002), p. 111.
14. A. V. Syromyatnikov and S. V. Maleyev, Phys. Rev. B **66**, 132408 (2002); Zh. Éksp. Teor. Fiz. **125** (3), 609 (2004) [JETP **98** (3), 538 (2004)].
15. K. Kubo, Phys. Rev. B **48**, 10552 (1993); T. Nakamura and K. Kubo, Phys. Rev. B **53**, 6393 (1996); H. Otsuka, Phys. Rev. B **51**, 305 (1995).
16. G. Misguich, B. Bernu, C. Lhuillier, and C. Waldtmann, Phys. Rev. Lett. **81**, 1098 (1998).
17. M. Roger, Phys. Rev. Lett. **64**, 297 (1990).

Thermally Stable Hydrogen Compounds Obtained under High Pressure on the Basis of Carbon Nanotubes and Nanofibers

I. O. Bashkin[1], *, V. E. Antonov[1], A. V. Bazhenov[1], I. K. Bdikin[1], D. N. Borisenko[1], E. P. Krinichnaya[2], A. P. Moravsky[2], A. I. Harkunov[1], Yu. M. Shul'ga[2], Yu. A. Ossipyan[1], and E. G. Ponyatovsky[1]

[1] *Institute of Solid-State Physics, Russian Academy of Sciences, Chernogolovka, Moscow region, 142432 Russia*
e-mail: bashkin@issp.ac.ru
[2] *Institute of Problems of Chemical Physics, Russian Academy of Sciences, Chernogolovka, Moscow region, 142432 Russia*
Received February 3, 2004

Compounds containing 6.3–6.5 wt % H and thermally stable in vacuum up to 500°C were obtained by annealing graphite nanofibers and single-walled carbon nanotubes in hydrogen atmosphere under a pressure of 9 GPa at temperatures up to 450°C. A change in the X-ray diffraction patterns indicates that the crystal lattice of graphite nanofibers swells upon hydrogenation and that the structure is recovered after the removal of hydrogen. It was established by IR spectroscopy that hydrogenation enhances light transmission by nanomaterials in the energy range studied (400–5000 cm^{-1}) and results in the appearance of absorption bands at 2860–2920 cm^{-1} that are characteristic of the C–H stretching vibrations. The removal of about 40% of hydrogen absorbed under pressure fully suppresses the C–H vibrational peaks. The experimental results are evidence of two hydrogen states in the materials at room temperature; a noticeable portion of hydrogen forms C–H bonds, but the most of the hydrogen is situated between the graphene layers or inside the nanotubes. © 2004 MAIK "Nauka/Interperiodica".

PACS numbers: 61.46.+w; 61.48.+c; 62.50.+p; 78.30.Na

The interaction of carbon nanostructural materials with gaseous hydrogen has been intensively studied over the last five years. The developed surface of these materials causes a considerable applied interest aimed at producing hydrogen accumulators and reducing the consumption of organic fuel in modern industry. For the academic studies, of interest is the character of hydrogen interaction with carbon nanotubes and nanofibers. In the published works, the saturation of nanostructures with hydrogen was carried out under relatively mild conditions; the hydrogen pressure did not exceed 100–120 atm (10–12 MPa) at liquid nitrogen or room temperature (see, e.g., review [1]). The data of different authors on the maximal amount of accumulated hydrogen show a scatter of two orders of magnitude, from several tenths to several tens of H wt %. As the general rule, the processes of hydrogen absorption and release in the cycles of pressure buildup and reduction were found to be reproducible at both room and nitrogen temperatures. Based on the data on the hydrogen absorption and release as functions of pressure or temperature, most authors assume that physisorption of H_2 molecules on the graphene layers is the dominating mechanism of hydrogen absorption. The studies of physical properties are few in number. The results of recent measurements of electronic transport properties and Raman spectra of single-walled nanotubes during the course of hydrogen adsorption and desorption at pressures up to 8 atm and temperatures from 4 to 500 K [2] are in accordance with the assumption about hydrogen physisorption. The maximal hydrogen content in nanotubes subjected to deep purification exceeded 6 wt % at pressures from 2 to 20 atm and a temperature of 77 K [2].

The chemical potential of hydrogen increases under pressure, and there are many examples of the increase in hydrogen solubility or the formation of hydride phases in the metal–hydrogen systems at high pressures. In this work, the interaction of hydrogen with carbon nanostructures—graphite nanofibers (GNFs) and single-walled carbon nanotubes (SWNTs)—is studied upon the thermal treatment with maximal parameters of 9 GPa and 450°C. The treatment gave samples that contained up to 7 wt % H and differed from the nanostructures hydrogenated under mild conditions by a higher thermal stability: the main hydrogen mass was released at $T \geq 500$°C.

Starting GNFs were synthesized in a direct-flow quartz reactor in a $CO : H_2 = 4 : 1$ gas mixture at 600°C for 6 h using a mixed $Fe : Cu = 7 : 3$ catalyst. Scanning electron microscopy showed that the GNF length was, on the average, 30 μm and the diameter ranged from 100 to 300 nm. The content of graphite nanofiber in the prepared material was about 90%.

Carbon black containing 15–20% SWNT was synthesized by the electric arc method in helium atmosphere at a pressure of 0.86 atm using a metallic Co : Ni = 3 : 1 catalyst [3]. To remove impurities from SWNT, carbon black was subjected to ultrasonic treatment in a concentrated hydrochloric acid, and then to the multistage treatment with hydrochloric acid alternating with oxidation in air at temperatures up to 540°C. The content of single-walled nanotubes in the product was estimated using scanning and transmission electron microscopies and was found to be equal to 50–60%.

In the experiments, a GNF or SWNT sample with a mass of about 60 mg was placed in a high-pressure chamber and saturated with hydrogen obtained by thermal decomposition of AlH_3. The sample was held under a hydrogen pressure of 9 GPa first for 18 h at $T = 350°C$ and then for another 6 h at 450°C. At the end of holding, the chamber was cooled to –140°C and unloaded to atmospheric pressure at this temperature. Then, the hydrogen-saturated material was taken out from the chamber and further held in liquid nitrogen. This technique was described in more detail in [4], where it was used to hydrogenate C_{60} fullerite.

From the hydrogenated GNF and SWNT powders, samples with a mass of several milligrams were chosen to determine their thermal stability and hydrogen content and to study them by X-ray diffraction and IR spectroscopy.

To estimate the thermal stability, the sample in a liquid nitrogen bath was placed in a nonhermetic copper container, while the latter was placed in a quartz ampoule that was cooled from outside by liquid nitrogen. The ampoule was attached to a vacuum system with the calibrated volume, the system was pumped out to a pressure of 10^{-3} mmHg, and the ampoule was heated at a rate of 20 K/min, with simultaneous measurement of the pressure P of a gas released during the course of heating to 600–650°C. The sample mass was determined by weighing after measurements.

The typical manometric curves for GNF–H and SWNT–H are shown in Fig. 1. The right axis of the graph indicates the amount x of liberated hydrogen as calculated under the assumption that the gas consisted only of H_2 molecules. The $x(T)$ dependences for GNF–H and SWNT–H are closely similar to each other. In the interval from 77 K to 0°C, the amount of liberated gas increases with temperature rather slowly, a small jump is observed near 0°C, and the gas release is terminated near room temperature. The total amount of hydrogen released upon heating to room temperature is 0.15–0.5 wt %. Gas is virtually not evolved from the samples upon heating from room temperature to 450°C, but the second stage of intense release begins near 500°C, and about 5 wt % H is collected at 600–650°C, i.e., an order of magnitude greater than upon heating to room temperature. The rate of gas release is low, so that the process is not terminated up to 600–650°C, and, as is shown in Fig. 1 by the example of GNF–H, an addi-
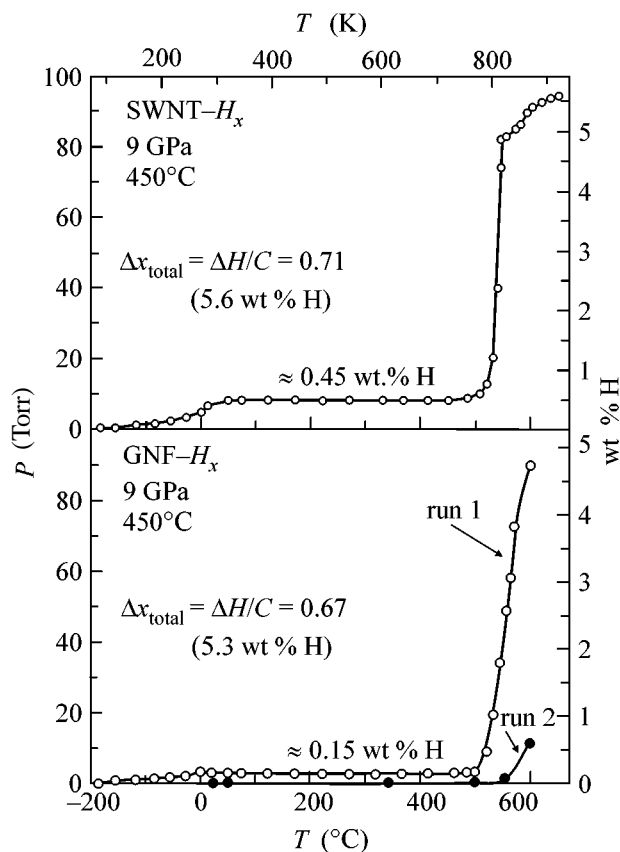
Fig. 1. Temperature dependence of gas pressure in a preliminarily evacuated volume (left vertical scale) and its recalculation into the amount of hydrogen evolved from the sample (right scale) upon heating at a rate of 20 K/min for single-walled carbon nanotubes (SWNT) and graphite nanofibers (GNF; two heating cycles) saturated with hydrogen at a pressure of 9 GPa and temperatures up to 450°C.

tional amount of gas is liberated upon repeated sample heating to 600°C at the same rate.

To determine the total hydrogen content and estimate the composition of liberated gas, the hydrogenated GNF and SWNT samples heated to room temperature were burned out in an oxygen flow at 1400°C and the combustion products H_2O and CO_2 were weighed. These measurements gave $x = 6.3$ wt % H for GNF and $x = 6.8$ wt % H for SWNT (this corresponds to the chemical formulas $CH_{0.81}$ and $CH_{0.88}$, respectively), with a spread in data less than ±0.05 wt %. The data obtained agree satisfactorily with the estimate $x \approx 5$ wt % H derived from the gas release between room temperature and 650°C, if it is considered that the gas release was incomplete. Such an agreement is evidence that hydrogen was liberated predominantly in the form of H_2 molecules rather than of hydrocarbons (e.g., if methane CH_4 were released, the amount of its molecules and, correspondingly, pressure would be twice as low in the gas-release experiments). A comparison of the burning results with the gas-release data allows the con-
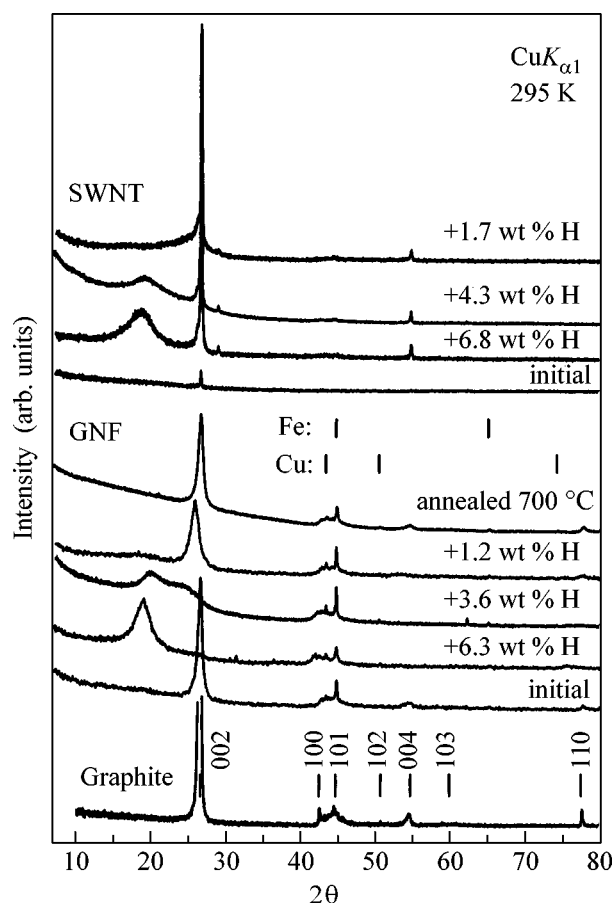
Fig. 2. X-ray diffraction patterns of single-walled carbon nanotubes and graphite nanofibers: in the initial state, after saturation with hydrogen at 9 GPa (6.8 and 6.3 wt % H, respectively), after removal of about 40% of absorbed hydrogen (4.3 and 3.6 wt % H), after degassing annealing to 600–650°C (1.7 and 1.2 wt % H), and after prolonged annealing at 700°C (GNF). For comparison, the diffraction pattern of a GDG-6 graphite powder is also shown. Bar diagrams of Fe and Cu indicate the catalyst admixture in GNF. Room temperature.

clusion to be drawn that, after measurements with heating to 600–650°C presented in Fig. 1, about 1.2 and 1.7 wt % H remained in the GNF and SWNT samples, respectively.

Figure 2 shows the X-ray diffraction patterns of GNFs and SWNTs in the initial and hydrogenated states and after various annealing procedures. Partial annealing with the removal of ~40% of hydrogen absorbed under pressure (the residual contents were 3.6 wt % H in GNF and 4.3 wt % H in SWNT) was carried out by holding the sample in an evacuated volume at a temperature of about 500°C, until the pressure of released gas reached the calculated value. Annealing of a GNF at 700°C was performed in a dynamic vacuum of <10^{-5} mmHg for 6 h. The X-ray diffraction pattern of the ground high-density graphite GDG-6 is presented in Fig. 2 for comparison. Measurements were made at

room temperature on a D500 Siemens diffractometer with the monochromatized Cu$K_{\alpha1}$ radiation.

The diffraction patterns of initial GNFs include a strong reflection near the graphite (002) line at $2\Theta = 26.5°$, a number of weak reflections near the other graphite lines, and the lines of catalyst components. After the saturation of a GNF with hydrogen, a broad intense peak appears near 19° instead of a very strong graphite reflection, while the other graphite reflections undergo a marked shift to small angles, and only the catalyst lines do not change their positions. After two heating cycles to 600°C shown in Fig. 1, the peak at 19° disappears and the diffraction pattern mainly regains its initial shape. Nevertheless, the most intense reflection remains markedly shifted to small angles, in agreement with the fact that hydrogen is removed incompletely. A prolonged vacuum annealing at 700°C results in a complete recovery of the initial diffraction pattern. A comparison of the diffraction pattern of the sample having 3.6 wt % H after partial annealing with the diffraction patterns of the extreme states shows that it represents the diffraction pattern of a two-phase state, in which the strongest reflections are shifted toward each other ($2\Theta \approx 19.9°$ and 24.0°) and are strongly broadened.

In the diffraction pattern of the initial SWNTs, no reflections are seen from the nanotubes (a weak reflection can be, in principle, observed at small angles ($2\Theta \sim 6°$) because of the triangular SWNT packing in beams; see, e.g., [5]). A sharp weak reflection at the position of the graphite (002) line should be caused by the presence of an admixture of graphitized particles in the material. The catalyst reflections are not seen. After the hydrogenation of an SWNT, a broad peak appears near 18.5°, while the narrow graphite (002) and (004) reflections are markedly strengthened. The removal of 2.5 wt % H results in weakening of the broad peak and its shifting by ~0.8° to larger angles, and this peak disappears after heating to 650°. The sharp graphite (002) and (004) reflections are retained and their intensity relative to the background changes only slightly. It was reported in the literature that an SWNT is not destroyed at hydrostatic pressures below 13 GPa [5]. For this reason, a change in the diffraction pattern of an SWNT after the thermal treatment in hydrogen should be assigned to the graphitization of amorphous carbon particles in the initial material and to the hydrogenation and dehydrogenation of a certain fraction of graphitized particles.

Weakly bonded hydrogen, which is released in an amount of less than 0.5 wt % upon heating to room temperature, can reasonably be assigned to physisorption, which is considered to be the dominant mechanism of hydrogen absorption by carbon materials at pressures below 12 MPa and not too high temperatures. To elucidate the nature of the bonded state of the main hydrogen mass that is retained up to high temperatures, the IR diffuse reflection spectra were measured for a GNF and SWNT in the initial state, after the treatment under hydrogen pressure, and after the degassing annealing.

Measurements were performed in the range 400–5000 cm^{-1} at room temperature on a Bruker IFS-113v IR Fourier spectrometer. The results are presented in Fig. 3.

The diffuse reflection carries information primarily about the transmission spectrum of the sample [6]. The spectra of initial GNFs are characterized by a monotonic decrease in transmission with increasing photon energy; such a spectral behavior is typical of the spectra of purified nanotubes [7]. As in the case of nanotubes exhibiting properties of a strongly imperfect metal or semimetal, the light absorption by free charge carriers caused by their high-frequency conductivity is the most probable reason for a decrease in the GNF transmission with increasing photon energy. In the spectra of initial SWNTs, a broad transmission minimum near 2600 cm^{-1} is superposed on the free-carrier absorption. Anomalies of this type were observed earlier and discussed in detail for granulated composite materials consisting of the conducting and nonconducting components (see [8] and references therein).

After the hydrogenation, the GNF transmission increases substantially over the entire range of measurements, and a narrow absorption band at 2860 cm^{-1} with a halfwidth of 38 cm^{-1} and a weaker band at 2920 cm^{-1} appear in the spectrum. These energies are typical of the stretching C–H vibrations. In the spectra of hydrogenated SWNTs, the transmission also increases; an asymmetric band with a maximum at 2860 cm^{-1} and a halfwidth of 95 cm^{-1} appears in the spectrum, while the broad minimum disappears. The asymmetry of the SWNT C–H band can be explained by the overlap between the bands at 2860 and 2920 cm^{-1}. The broad minimum irreversibly disappears in the subsequent annealing. Comparing with the changes in the SWNT diffraction pattern, one can assume that the minimum in the transmission spectrum of the initial SWNT is caused by the electric properties of the impurity amorphous carbon in the material, and the fact that it disappears is associated with the graphitization of carbon nanoparticles during the process of thermal treatment in hydrogen.

The disappearance of the C–H bands is the most pronounced effect in a partial (~40%) degassing of the GNF and SWNT samples. The background transmission is regained in part and occupies the intermediate position between the spectra of the initial and hydrogenated samples. After heating to 600–650 cm^{-1} and removal of the main hydrogen mass, the spectra become somewhat closer to the spectra of initial samples, but no complete recovery occurs; the spectrum of the GNF annealed for 6 h in vacuum at 700°C coincides with the spectrum observed after heating to 600°C (curve 4).

The decrease in the free-carrier absorption upon hydrogenation can be associated with both decrease in the free-carrier concentration and increase in the rate of
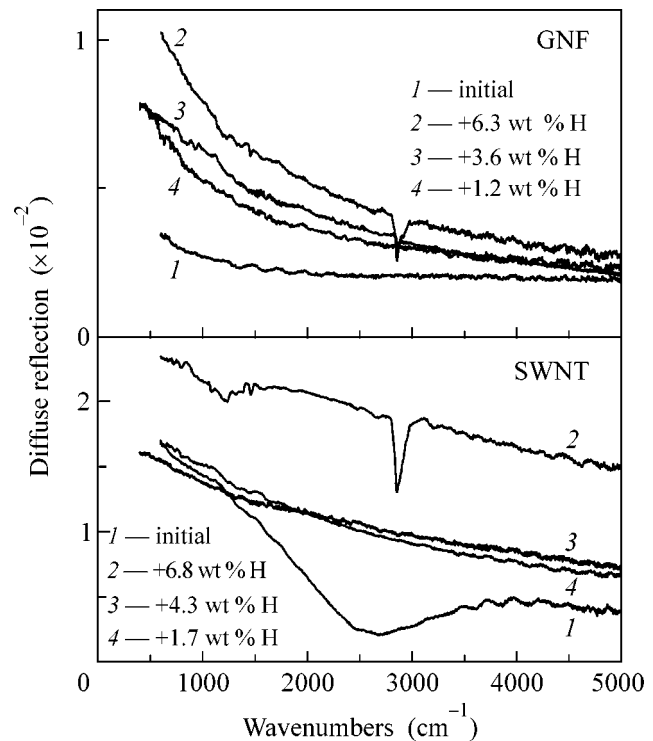
Fig. 3. IR diffuse reflection spectra of graphite nanofibers and single-walled carbon nanotubes: in the initial state, after saturation with hydrogen at 9 GPa, after removal of about 40% of absorbed hydrogen, and after degassing annealing. Room temperature.

their scattering from defects. After the conversion of the diffuse reflection spectra into the absorption spectra, we have found that, in the range of small wavenumbers ν, the absorption changes as $\sqrt{\nu}$, which corresponds to the spectral dependence of free-carrier absorption in the Drude approximation for ν much smaller than the charge-carrier scattering rate. By using the Drude relations, we found that, after the GNF and SWNT hydrogenation, the high-frequency free-carrier conductivity decreased by a factor of 9.

The combination of the experimental data gives evidence that there are three possible hydrogen states in the hydrogenated carbon nanostructures quenched under pressure. A small portion of hydrogen (less than 0.5 wt %) is retained at 77 K in the form of weakly bonded adsorbed molecules that are released below room temperature. About 40% of hydrogen retained up to room temperature forms strong C–H bonds that are thermally stable up to ~500°C. However, 60% or more of the strongly bonded hydrogen occurs in the IR-inactive state. At a temperature of ~500°C, hydrogen in this state is retained longer than the covalently bonded hydrogen. A change in the diffraction pattern of the multilayer GNF structure upon hydrogenation can be considered as being caused mainly by an increase in the lattice parameter c. In this case, the shift in the (002) peak after the absorption of 6.3 wt % H corresponds to

the increase in the interplanar spacing between the graphene layers by approximately 40% from 3.36 to 4.67 Å. The increase in *c* as large as that allows one to assume that the third state is a molecular hydrogen situated between the graphene layers in the nanofiber bulk. This assumption explains the two-phase diffraction pattern of the partially annealed GNF sample containing 3.6 wt % H, which is likely characterized by the presence of concentrational inhomogeneity and microstrains. The idea of accumulation of molecular hydrogen between the graphene layers was put forward earlier when studying the interaction of atomic hydrogen with graphite [9] or in the study of the interaction of hydrogen with graphite during the grinding process in ball mills [10, 11]. However, the diffraction measurements in these works were hampered by the fact that the penetrability of atomic hydrogen was limited by only one carbon layer [9], while the grinding in a mill rapidly brought the sample into the amorphous state [10, 11].

The question of the hydrogen positions in the hydrogenated SWNT product at normal conditions is more complicated. The possibility of hydrogen molecule penetrating through the wall of a closed SWNT was theoretically considered in [12]. However, one should take into account that our product contains from 40 to 50 wt % impurity carbon nanoparticles that crystallize upon thermal treatment and take part in the hydrogenation and dehydrogenation processes. All structure reflections in the SWNT diffraction patterns are likely caused by the presence of such (multilayer) particles in the hydrogenated or nonhydrogenated states. The hydrogen absorption by the SWNT product (6.8 wt % H, as compared to 6.3 wt % H in GNF), nevertheless, cannot be explained by the hydrogenation of impurity carbon particles alone, because they comprise the smaller part of the sample and are hydrogenated incompletely. It is reasonable to assume that the amounts of hydrogen in the carbon nanoparticles and in nanotubes themselves are comparable in the hydrogenated SWNT product. The fact that temperatures and desorption rates of hydrogen from the hydrogenated SWNT and GNF are close to each other allows one to assume that the bonding character between hydrogen and carbon in the SWNT and GNF, as well as the mechanism of hydrogen release, can be similar.

In summary, the interaction of carbon nanomaterials with hydrogen at high pressures and temperatures has given rise to thermally stable compounds containing up to 6.8 wt % of hydrogen, most of which is in the new state characterized by the absence of the C–H bands in the IR spectra.

REFERENCES

1. A. C. Dillon and M. J. Heben, Appl. Phys. A **72**, 133 (2001).

2. B. K. Pradhan, G. U. Sumanasekera, C. K. W. Adu, *et al.*, Physica B (Amsterdam) **323**, 115 (2002).

3. R. O. Loutfy, T. P. Lowe, J. L. Hutchison, *et al.*, in *Abstracts of IV Workshop on Fullerenes and Atomic Clusters (IWFAC'99)* (St. Petersburg, 1999), p. 117.

4. V. E. Antonov, I. O. Bashkin, S. S. Khasanov, *et al.*, J. Alloys Compd. **330–332**, 365 (2002).

5. S. M. Sharma, S. Karmakar, S. K. Sikka, *et al.*, Phys. Rev. B **63**, 205 417 (2001).

6. R. R. Willey, Appl. Spectrosc. **30**, 593 (1976); M. P. Fuller and P. R. Griffiths, Anal. Chem. **50**, 1906 (1978).

7. A. V. Bazhenov, V. V. Kveder, A. A. Maksimov, *et al.*, Zh. Éksp. Teor. Fiz. **113**, 1883 (1998) [JETP **86**, 1030 (1998)].

8. P. Sheng, Phys. Rev. Lett. **45**, 60 (1980).

9. E. A. Denisov, T. N. Kompaniets, I. V. Makarenko, *et al.*, Materialovedenie **2**, 45 (2002).

10. S. Orimo, T. Matsushima, H. Fujii, *et al.*, J. Appl. Phys. **90**, 1545 (2001).

11. T. Fukunaga, K. Itoh, S. Orimo, *et al.*, J. Alloys Compd. **327**, 224 (2001).

12. Y. Ma, Y. Xia, M. Zhao, *et al.*, Phys. Rev. B **63**, 115 422 (2001).

Translated by V. Sakun

Phase Transition in a Self-Repairing Random Network[¶]

A. S. Ioselevich and D. S. Lyubshin

Landau Institute for Theoretical Physics, Russian Academy of Sciences, Moscow, 117940 Russia

Received February 5, 2004

We consider a network the bonds of which are being sequentially removed; this is done at random but conditioned on the system remaining connected (self-repairing bond percolation, SRBP). This model is the simplest representative of a class of random systems for which the formation of isolated clusters is forbidden. It qualitatively describes the process of fabrication of artificial porous materials and degradation of strained polymers. We find a phase transition at a finite concentration of bonds $p = p_c$, at which the backbone of the system vanishes; for all $p < p_c$, the network is a dense fractal. © 2004 MAIK "Nauka/Interperiodica".

PACS numbers: 64.60.Ak; 61.43.Gt; 81.05.Rm; 81.16.Rf

Properties of networks the bonds (or nodes) of which are being removed randomly have been intensively studied for the past 50 years. In the standard formulation of the problem, the bonds (or sites) are removed totally at random, and the percolation transition takes place at a certain concentration p_c of the remaining bonds (or concentration x_c of remaining sites). For $p > p_c$, there exists an "infinite" cluster that contains a finite fraction of all bonds in the system and spans homogeneously through the entire network. At $p < p_c$, the infinite cluster does not exist and only finite ones are present. The percolation phase transition and corresponding critical phenomena are well studied (see, e.g., [1, 2]).

However, there are many physical systems which cannot be described by the standard percolation theory. In particular, there are important cases when finite clusters cannot appear at all. As an example, consider the technologically important process of pore forming (i.e., fabrication of a porous material; see, e.g., [3]). It can be viewed as gradual removal of grains of a pore former (carbon, which can be burned out, or a soluble polymer) from a mixture of the pore former with grains of a matrix material (a metal). Due to mechanical instability of finite clusters, they immediately fall onto the surrounding matrix and stick to it. Thus, at any stage of the process, the remaining grains form a single "infinite cluster" and the percolation transition is impossible. The properties of this single cluster are nontrivial: it appears that there is a topological phase transition at a finite concentration of remaining grains x_c, below which the system becomes "cracked" and its mechanical and conducting properties degrade catastrophically.

In the present paper, we introduce a simple model which possesses the main property of the above systems (existence of only one cluster) and allows rigorous analysis. The model is very similar to the standard bond

percolation: starting from a full lattice, at each step, one of the remaining bonds is randomly chosen for removal. But, after its removal, the system is checked for the existence of finite clusters: if such clusters are present, then the removed bond is restored (i.e., the last removal is cancelled) and the process goes on to the next step. It seems natural to call this model a "self-repairing bond percolation" (SRBP).

Apart from being relevant to pore-forming, the SRBP model may also be viewed as a model for polymer degradation (see, e.g., [4]). Consider a random network consisting of irregularly cross-linked polymer chains. Suppose that this system is subjected to random external perturbation (e.g., UV radiation) that can destroy the cross links. The radiation damage may be repairable: attraction between individual chains tends to reestablish the damaged link. However, sometimes, that appears to be impossible, since internal strains in the chains may drive the two chains apart as soon as the link between them is damaged. Thus, it seems reasonable to assume that all strained links are vulnerable to radiation damage, while unstrained ones are "immune" to it. Of course, finding out which links in a random network are strained and which are not is a formidable task. But, in any case, the links which are the only bridges connecting otherwise isolated clusters are never strained. These links will be repaired after possible removal, in accordance with the definition of the SRBP model.

Our model is also relevant to river network formation. In two dimensions, it is in fact dual to the "loopless percolation" model that was studied numerically in [5].

Let the fraction of the remaining bonds be p. We will be interested in average properties of the system as a function of p. In particular, we will study the conductivity $\sigma(p)$ and the "minimal chemical path" $l(R, p)$, the latter being an ensemble-averaged length of the shortest

---

[¶] This article was submitted by the authors in English.
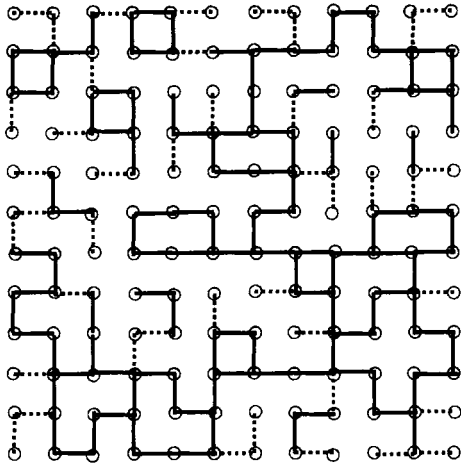
Fig. 1. Typical configuration of black and gray bonds at the critical concentration for 2D square lattice.

path going via bonds and connecting two points separated by Euclidean distance R.

The first obvious observation about the SRBP model is that there exists some minimal possible $p = p_{\text{tree}} \equiv 2/z$ (z being the coordination number of the lattice) at which the process of bond removal stops: for a connected graph, one necessarily has $p \geq p_{\text{tree}}$. At $p = p_{\text{tree}}$, the remaining bonds constitute a spanning tree (ST), a connected graph with no cycles, and all lattice sites as vertices. As is well known, the probability of generating a given ST at the end of our process is related to the minimal spanning tree (MST) problem (see, e.g., [6]). In particular, the minimal chemical path is fractal: $l(R,$ $p = p_{\text{tree}}) \propto R^{d_{\min}^{\text{MST}}}$ with $d_{\min}^{\text{MST}} > 1$. Obviously, for a tree, one has $\sigma(p = p_{\text{tree}}) = 0$.

We will show that actually the minimal chemical path is fractal and the specific conductivity of the system is zero not only at $p = p_{\text{tree}}$ but also within a finite interval $p_{\text{tree}} \leq p \leq p_c$. The corresponding phase we will call the "treelike phase," in contrast to the "solid phase" existing at $p_c \leq p \leq 1$.

To prove the above statement, we use a mapping to the standard percolation. Suppose that initially all the bonds of the system are black. If, at some step, a removal of a certain bond must be cancelled, we restore the bond but change its color to gray. Then, for any fraction p of remaining bonds, we have fractions $b = b(p)$ of black and $g = p - b(p)$ of gray bonds remaining. It is easy to show that $b(p)$ is a monotonically increasing function with the following asymptotics:

$$b(p) \approx \begin{cases} p & \text{for } 1 - p \ll 1, \\ 0 & \text{for } p \longrightarrow p_{\text{tree}}. \end{cases} \quad (1)$$

Clearly, a gray bond may never be removed, and, at $p = p_{\text{tree}}$, all bonds are either removed or gray. It is easy

to see that the backbone of the entire (black and gray) network coincides with the backbone of the black subsystem. Indeed, no gray bond can belong to the backbone: since its removal produces an isolated finite cluster, such a bond belongs to a dangling end. Note that black bonds are removed *totally at random*; hence, the behavior of the black subsystem is identical to that of the standard bond-percolation system. In particular, the backbone vanishes at the percolation point, where $b = p_{\text{perc}}$. It follows that there exists a critical concentration of bonds p_c such that, for $p < p_c$, the remaining bonds all belong to one infinite cluster (which has a finite density), while this cluster *has no backbone*. The critical concentration is determined by the condition

$$b(p_c) = p_{\text{perc}}, \quad (2)$$

where p_{perc} is the percolation threshold for the standard bond percolation problem on the same lattice. On the other hand, the number of gray bonds in the system is equal to the number of finite black clusters: $g = n_{\text{cl}}$ (see Fig. 1). Thus, the critical concentration p_c can be expressed solely through the characteristics of the standard percolation problem:

$$p_c = p_{\text{perc}} + n_{\text{cl}}^*, \quad (3)$$

where n_{cl}^* is the number of finite clusters (per bond of the initial lattice) at the critical point. The latter is known for many lattices; in particular, for the square lattice $n_{\text{cl}}^* = (3\sqrt{3} - 5)/4$ (see [7, 8]) and $p_{\text{perc}} = 1/2$, so

$$p_c = \frac{3\sqrt{3} - 3}{4} \approx 0.54904. \quad (4)$$

In the scaling theory of percolation, the relations between different critical exponents are normally derived from considerations involving distribution function of finite clusters (see, e.g., [2]). In our model, finite clusters do not exist whatsoever, but fortunately one can introduce blocks—alternative objects, which to some extent, play the role of finite clusters and make it possible to develop the scaling theory. By definition, a *block* is a maximal subgraph that cannot be disconnected by deletion of a single vertex [9]. It is not difficult to show that either a block consists of a single bond (and its two ends) or any two bonds belonging to a block lie on a common cycle. Two distinct blocks may have at most one point in common; such a point is called an *articulation point*, and its deletion necessarily disconnects the system. Given a network, one can form a graph with blocks and articulation points of the network as vertices, with two vertices connected if they correspond to an articulation point and a block that contains it. Such a *block graph* is always a tree; an example is shown in Fig. 2.

The backbone that exists in the solid phase constitutes the only infinite block in the system; it has a finite density and contains infinite cycles. The backbone is

linked to an infinite number of branches—dangling ends, each dangling end being a finite tree of finite blocks.

In the treelike phase, the infinite block collapses, so that there are only finite cycles in this phase. The corresponding bond configurations we will call quasitrees.

In the solid phase, the backbone becomes looser as p approaches p_c. The fraction of bonds belonging to it tends to zero:

$$P_B(p) \propto (p - p_c)^{\beta_B}, \qquad (5)$$

where β_B is the index of the backbone density for the standard percolation (in particular, $\beta_B \approx 0.48$ for $d = 2$; see, e.g., [2, 10]).

The total number of dangling ends decreases as $p \longrightarrow p_c$ from above, while the number of blocks in each dangling end and the number of bonds in a typical block increase and diverge as $p \longrightarrow p_c$. It is convenient to introduce the distribution function of finite blocks consisting of l bonds:

$$n_l(p) \sim l^{-\tau} f[l(p - p_c)^{1/\sigma}], \qquad (6)$$

where $f(x)$ is a universal function that decays exponentially at $x \gg 1$. Application of standard scaling arguments [2] to blocks leads to the following relations between the critical exponents:

$$\nu = \frac{\tau - 1}{\sigma d}, \quad \xi(p) \sim (p - p_c)^{-\nu}. \qquad (7)$$

The length $\xi(p)$ characterizes correlations within the backbone, and since the backbone for the SRBP model is the same as for standard percolation, we conclude that the exponent ν for the SRBP model coincides with that for standard percolation.

The exponent γ that characterizes the behavior of the mean size $S(p)$ of finite blocks near p_c is

$$\gamma = \frac{3 - \tau}{\sigma}, \quad S(p) \equiv \frac{\sum_l l^2 n_l(p)}{p - P_B(p)} \propto (p - p_c)^{-\gamma}. \qquad (8)$$
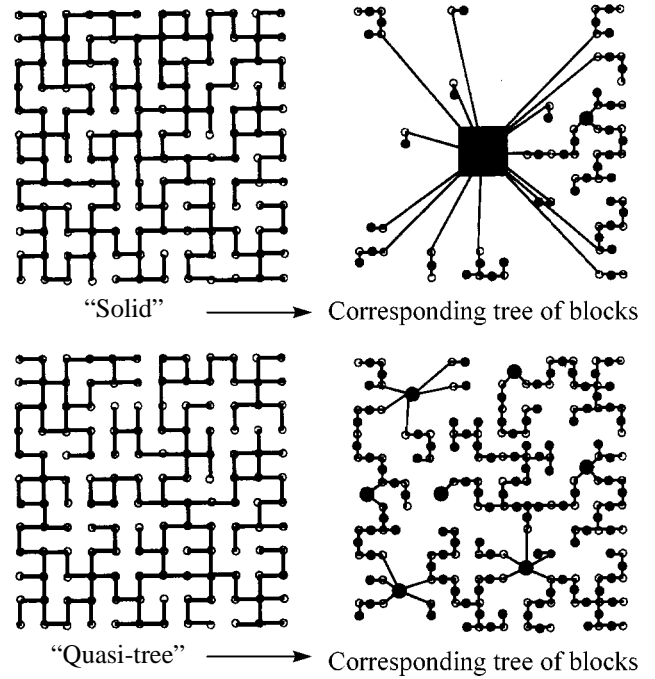
Finally,

$$\beta_B = \frac{\tau - 2}{\sigma}, \quad d_B = \frac{d}{\tau - 1}, \qquad (9)$$

where d_B is the fractal dimension of the backbone at $p = p_c$.

Since the conduction process involves only the backbone, the conductivity of the SRBP model is identical to that of the standard percolation,

$$\sigma_{\text{SRBP}}(p) \equiv \sigma_{\text{perc}}[b(p)] \propto (p - p_c)^{\mu}, \qquad (10)$$

Fig. 2. Typical configurations of bonds in the solid and tree-like phases (we do not distinguish black and gray bonds here), together with corresponding block graphs. Black square, the infinite block (the backbone); large solid circles, finite nontrivial blocks; small solid circles, trivial blocks; small open circles, articulation points.

hence, the critical exponent μ is the standard one. For the minimal path length in the solid phase, one has

$$l(R) = \frac{R}{v(p)}, \qquad (11)$$
$$v(p) \sim \xi(p)^{1 - d_{\min}^{\text{perc}}} \sim (p - p_c)^{-\nu + \nu d_{\min}^{\text{perc}}},$$

where $d_{\min}^{\text{perc}}$ is the graph dimension for the infinite cluster at the critical point for the standard percolation problem. As usual, formula (11) is valid only for $R \gg \xi(p)$; in the opposite case $R \ll \xi(p)$, it should be substituted by the critical law

$$l(R) \propto R^{d_{\min}^{\text{perc}}}. \qquad (12)$$

For $R \sim \xi(p)$, expressions (11) and (12) match.

At $p = p_{\text{tree}}$, our system is reduced to the MST ensemble. In high dimensions $d > d_c$, a minimal spanning tree on an *infinite* lattice may in fact have many components. It is believed (see [11]) that $d_c = 8$, and in $d < 8$ dimensions for almost all trees of the MST ensemble, there exists a unique finite path $\mathcal{P}(A, B)$ connecting any two given sites A and B. This path is a certain non-self-intersecting random walk with fractal dimension $d_f = d_{\min}$. While this dimension is known exactly for the 2D uniform spanning tree ensemble, only numerical estimates are available for the MST case: $d_{\min} \approx 1.22$ for
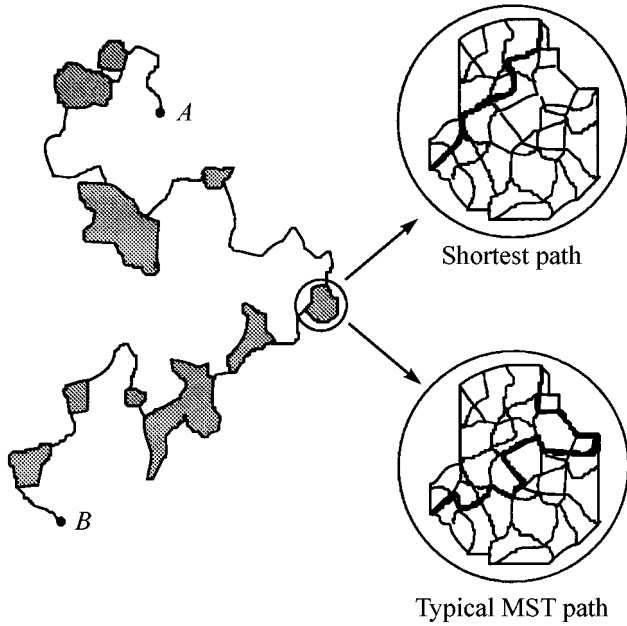
Fig. 3. The path connecting points A and B on the block graph; nontrivial blocks are shown as gray islands. The internal structure of a typical block is shown in the insets: (lower panel) a typical MST path traversing a block and (upper panel) the shortest path across the block.
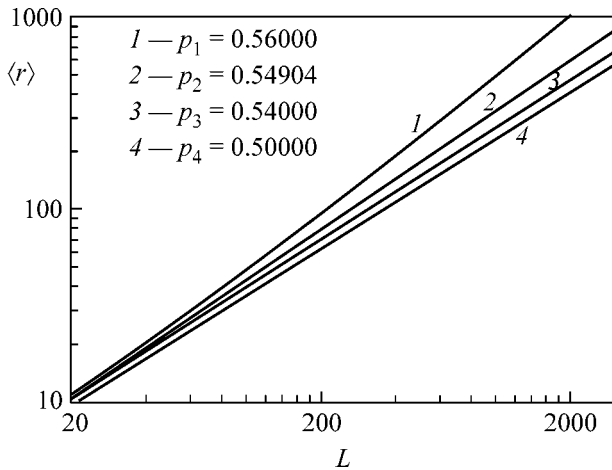
Fig. 4. Root mean square Euclidean displacement vs. chemical distance for different values of p, obtained via averaging over 1600 realizations of a 2048×2048 lattice with periodic boundary conditions. Asymptotic slopes correspond to $d_{min}(p_c) = 1.13(1)$ and $d_{min}(p_c - 0.01 = 0.54) = d_{min}(p_{tree}) = 1.22(1)$, in agreement with known results.

$d = 2$, $d_{min} \approx 1.42$ for $d = 3$, and $d_{min} \approx 1.59$ for $d = 4$ (see [12]). Below, we demonstrate that the graph dimension is the same *throughout the entire treelike phase*:

$$d_{min}(p) = d_{min}^{MST}, \quad \text{for } p_{tree} \leq p < p_c. \tag{13}$$

More precisely,

$$l(R, p) = \frac{R^{d_{min}^{MST}}}{v(p)}, \tag{14}$$

$$v(p) \sim \xi(p)^{d_{min}^{MST} - d_{min}^{perc}} \sim (p_c - p)^{-\nu d_{min}^{MST} + \nu d_{min}^{perc}}.$$

Consider a certain quasitree $\mathcal{Q}$ and the set of trees $\mathcal{T}_i^{(\mathcal{Q})}$ which can originate from $\mathcal{Q}$ in the course of further destruction of bonds. Obviously, $\mathcal{Q}$ is a union of all such trees: $\mathcal{Q} = \bigcup_i \mathcal{T}_i^{(\mathcal{Q})}$. Now, we introduce a graph

$$\overline{\mathcal{P}}(A, B)^{(\mathcal{Q})} = \bigcup_i \mathcal{P}_i(A, B)^{(\mathcal{Q})}, \tag{15}$$

which is the union of all paths $\mathcal{P}_i^{(\mathcal{Q})}$ leading from A to B in all trees $\mathcal{T}_i^{(\mathcal{Q})}$. It is easy to show that $\overline{\mathcal{P}}(A, B)^{(\mathcal{Q})}$ is precisely the path leading from A to B *in the block graph* (see Fig. 3). The minimal (over the entire quasitree) path $\mathcal{P}(A, B)^{(\mathcal{Q})}$ leading from A to B is, obviously, the minimal path over the graph $\overline{\mathcal{P}}(A, B)^{(\mathcal{Q})}$. On nontrivial (containing more than one bond) blocks, the path $\mathcal{P}(A, B)^{(\mathcal{Q})}$ is the shortest path that crosses the block; it may be considerably shorter than any individual MST path. This consideration enables one to estimate the typical ratio of lengths for a piece of the minimal path $\mathcal{P}(A, B)^{(\mathcal{Q})}$ and the corresponding piece of the MST minimal path. We make such an estimate for the case when $p < p_c$ but $p_c - p \ll 1$ (i.e., for the vicinity of the phase transition). Having in mind that the typical block size is $\xi(p) \gg 1$, for a typical length MST path crossing such a block, we get $l_{MST}(\xi) \sim \xi^{d_{min}^{MST}}$, while the *shortest* path traversing the block is the same as for the critical percolation: $l_{short}(\xi) \sim \xi^{d_{min}^{perc}}$. As a result, we arrive at estimate (14), which matches with (12) for the critical case $R \sim \xi$.

Since the above consideration is not quite rigorous, we have also undertaken numerical evaluation of $d_{min}(p)$ in order to check identity (13). Simulations did not show any variation of d_{min} with p for $p < p_c$ (see Fig. 4).

In conclusion, we have demonstrated that the self-repairing bond percolation model undergoes a topological phase transition at a certain concentration p_c of remaining bonds. In the treelike phase (for $p < p_c$), the network, although being fully connected, has *no backbone* and, hence, zero conductivity. The corresponding graphs of bonds are "quasitrees": they contain only finite cycles (even for the infinite lattice). The properties of the statistical ensemble of quasitrees are similar to those of the minimal spanning trees ensemble.

REFERENCES

1. D. Stauffer and A. Aharony, *Introduction to Percolation Theory* (Taylor and Fransis, London, 1994).

2. A. Bunde and S. Havlin, in *Fractals and Disordered Systems*, Ed. by A. Bunde and S. Havlin (Springer, Berlin, 1996).

3. *Disorder and Granular Media*, Ed. by D. Bideau and A. Hansen (North-Holland, Amsterdam, 1993).

4. *Handbook of Material Weathering,* Ed. by G. Wypych, 3rd ed. (William Andrew, Norwich, N.Y., 2003); *The Effect of UV Light and Weather on Plastics and Elastomers* (PDL Staff, Plastics Design Library, 1994).

5. S. S. Manna and B. Subramanian, Phys. Rev. Lett. **76**, 3460 (1996).

6. R. Dobrin and P. M. Duxbury, Phys. Rev. Lett. **86**, 5076 (2001).

7. H. N. V. Temperley and E. H. Lieb, Proc. R. Soc. London, Ser. A **322**, 251 (1971).

8. R. M. Ziff, S. Finch, and V. Adamchik, Phys. Rev. Lett. **79**, 3447 (1997).

9. F. Harary, *Graph Theory* (Addison-Wesley, Reading, Mass., 1969; Mir, Moscow, 1973).

10. P. Grassberger, Physica A (Amsterdam) **262**, 251 (1999).

11. C. M. Newman and D. L. Stein, Phys. Rev. Lett. **72**, 2286 (1994).

12. M. Cieplak, A. Maritan, and J. R. Banavar, Phys. Rev. Lett. **76**, 3754 (1996).

A Small Error-Correction Code for Protecting Three-Qubit Quantum Information[¶]

Chui-Ping Yang[1, 2], Shih-I Chu[2], and Siyuan Han[1]

[1] *Department of Physics and Astronomy, University of Kansas, Lawrence, Kansas 66045, USA*

[2] *Department of Chemistry, University of Kansas, and University of Kansas for Advanced Scientific Computing, Lawrence, Kansas 66045, USA*

Received December 16, 2003

We present a quantum error correction code which protects three quantum bits (qubits) of quantum information against one erasure, i.e., a single-qubit arbitrary error at a known position. The present code has a high encoding efficiency, since only one auxiliary qubit is needed for one message qubit on average. In addition, we note that the code can also work even in a worse case that the interaction with the environment causes a leakage out of the qubit space. The code may have some applications in the storage of quantum information for small-scale quantum computing, quantum information processing, and quantum communication. © 2004 MAIK "Nauka/Interperiodica".

PACS numbers: 03.67.Lx; 03.67.Hk; 03.65.Yz; 89.70.+c

Quantum computing has become an active aspect of current research fields with the discovery of Shor's algorithm for factorizing a large number [1, 2]. It has become clear that a quantum computer is in principle able to solve hard computational problems more efficiently than present classical computers [1–4]. However, the biggest difficulty inhibiting realizations is the fragility of quantum states. Decoherence of qubits caused by the interaction with the environment will collapse the state of the quantum computer and thus lead to the loss of information. To solve this problem, Shor, and independently Stean, inspired by the theory of classical error correction, proposed the first two quantum error correction codes (QECCs), i.e., the nine-qubit code [5] and the seven-qubit code [6], which are able to correct errors that occur during the storage of qubits. Following this work, many new QECCs have been discovered [7–20]. For the most general error model, Laflamme *et al.* have shown that the smallest quantum error correction code, for encoding one qubit of quantum information and correcting a single-qubit arbitrary error at an unknown position, is the five-qubit code [7]. On the other hand, apart from the QECCs, many alternative quantum codes have been proposed, such as the quantum error preventing codes (based on the quantum Zeno effect) [21, 22] and the quantum error-avoiding codes (based on decoherence-free subspaces (DFSs)) [23–25]. Moreover, dynamical suppression of decoherence [26–28] and noiseless subsystems [29–32] have been presented.

In 1997, Grassl *et al.* [33] considered an error model where the position of the erroneous qubits is known. In accordance with classical coding theory, they called this model the quantum erasure channel. Some physical scenarios to determine the position of an error have been given [33]. For instance, if errors are accompanied by the emission of quanta, they can in principle be detected. In their work, they showed that only a four-qubit error correction code is required to encode one qubit and correct one erasure (i.e., a single-qubit arbitrary error for which the position of the "damaged" qubit is known). Also, they showed that two qubits of quantum information could be encoded and one erasure could be corrected by extending such a four-qubit code, in a sense that only one additional qubit is required for encoding one "message" qubit on average. Clearly, this code is a very compact code for protecting one or two qubits of quantum information as long as the position of the "bad" qubit is known. However, at least *eight* qubits are needed in protecting three-qubit quantum information by using such a code (four qubits required for encoding one qubit of quantum information plus another four qubits necessary for encoding the remaining two qubits of quantum information). In this letter, we will present a new error-correction code, which requires only three auxiliary qubits (i.e., a total of six qubits) for protecting three qubits of quantum information against one erasure. We will show how the present code works through the encoding, decoding, and error recovery operations.

The Hilbert space of a three-qubit system is a tensor product of two-dimensional spaces C_2 (qubits), i.e.,

---

[¶] This article was submitted by the authors in English.

$C = C_2^{\otimes 3}$. An arbitrary state of three qubits (labeled 1, 2, and 3) can be expanded as follows:

$$|\psi\rangle_{123} = \alpha_0|000\rangle + \alpha_1|001\rangle + \alpha_2|010\rangle + \alpha_3|011\rangle$$
$$+ \alpha_4|100\rangle + \alpha_5|101\rangle + \alpha_6|110\rangle + \alpha_7|111\rangle, \qquad (1)$$

where $\sum_{i=0}^{7} |\alpha_i|^2 = 1$; $\{|ijk\rangle\}$ forms a set of complete orthogonal states in the eight-dimensional space, $i, j, k \in \{0, 1\}$; and we take the $|0\rangle$ and $|1\rangle$ states of a qubit to correspond to the "down" and "up" states, respectively, of a fictitious spin 1/2 particle. Using three ancillary qubits (1', 2', 3'), we encode the original state into

$$|\psi\rangle_L = \alpha_0|0\rangle_L + \alpha_1|1\rangle_L + \alpha_2|2\rangle_L + \alpha_3|3\rangle_L$$
$$+ \alpha_4|4\rangle_L + \alpha_5|5\rangle_L + \alpha_6|6\rangle_L + \alpha_7|7\rangle_L, \qquad (2)$$

where the eight logical states are

$$|0\rangle_L = (|000\rangle + |111\rangle) \otimes (|000\rangle + |111\rangle),$$

$$|1\rangle_L = (|000\rangle - |111\rangle) \otimes (|000\rangle - |111\rangle),$$

$$|2\rangle_L = (|010\rangle + |101\rangle) \otimes (|010\rangle + |101\rangle),$$

$$|3\rangle_L = (|010\rangle - |101\rangle) \otimes (|010\rangle - |101\rangle),$$

$$|4\rangle_L = (|100\rangle + |011\rangle) \otimes (|100\rangle + |011\rangle), \qquad (3)$$

$$|5\rangle_L = (|100\rangle - |011\rangle) \otimes (|100\rangle - |011\rangle),$$

$$|6\rangle_L = (|110\rangle + |001\rangle) \otimes (|110\rangle + |001\rangle),$$

$$|7\rangle_L = (|110\rangle - |001\rangle) \otimes (|110\rangle - |001\rangle)$$

(here, for every logical state, the left part of the product corresponds to the three "message" qubits, while the right part of the product corresponds to the three ancillary qubits, and the arrangement sequence of the six qubits is 1, 2, 3, 1', 2', and 3' from left to right; to simplify the notation, normalization factors are omitted here and in the remainder of this section).

Let us first briefly review some basics of quantum error correction codes. It has been shown that one can model the errors by the use of error operators A. For the general case, Kill and Laflamme [17] derived the following necessary and sufficient conditions on quantum error correction codes:

$$\langle i_L | A_a^+ A_b | i_L \rangle = \langle j_L | A_a^+ A_b | j_L \rangle, \qquad (4)$$

and

$$\langle i_L | A_a^+ | j_L \rangle = 0 \quad \text{for} \quad \langle i_L | j_L \rangle = 0, \qquad (5)$$

where $|i_L\rangle$ and $|j_L\rangle$ are any two orthonormal basis states of the code (i.e., any two logical states). For the purpose of error correction, it is enough to consider errors of the type σ_x (bit flip), σ_z (phase flip), and σ_y (bit and phase flip), since, by linearity, a code that can correct these errors can correct any arbitrary errors [8]. For an [n, k, t] code, i.e., a code encoding k qubits through n qubits and correcting t errors at most, the error operators $\{A_a\}$

are the tensor product of the identity on $n - t$ qubits and t one-bit error operators on the altered qubits. The one-bit error operators are any linear combinations of the algebra basis $\{1, \sigma_x, \sigma_y, \sigma_z\}$.

The above conditions have been generalized to the quantum erasure channel [33, 34]. Since the positions of the errors are known, it is not necessary to separate the spaces which correspond to errors at different positions. For the case of correcting erasure errors, the error operators A_a and A_b differ from each other by one-bit error operators at the same positions only. Since the product of such t-error operators is also a t-error operator, which can be written as a linear combination of the A_a, it follows from Eqs. (4) and (5) that the necessary and sufficient conditions corresponding to the erasure-correcting case will be [33, 34]

$$\langle i_L | A_a | i_L \rangle = \langle j_L | A_a | j_L \rangle, \qquad (6)$$

$$\langle i_L | A_a | j_L \rangle = 0 \quad \text{for} \quad \langle i_L | j_L \rangle = 0. \qquad (7)$$

Now, we give the interpretations of the encoding (3) in terms of error correction codes. For the case of one erasure, the error operators A_a in Eqs. (6) and (7) are the one-bit error operators for the bad qubit, which are any linear combinations of the algebra basis $\{1, \sigma_x, \sigma_y, \sigma_z\}$. One can easily verify that no matter which qubit goes bad, any two of the eight logical states (3) satisfy the above conditions (6) and (7). Thus, these logical states in (3) can be regarded as an erasure-correcting code: it can, in principle, encode three qubits and correct one erasure. In the following, we will show explicitly how this can be done.

The encoding (3) can be fulfilled by the quantum CNOT (controlled-NOT) operations C_{ij}, where the first subscript of C_{ij} refers to the control bit, and the second, to the target. The three ancillary qubits 1', 2', and 3' are initially in the state $|000\rangle$. Throughout this paper, every joint operation will follow the sequence from right to left. Let a joint encoding operation on the six qubits

$$U_e = C_{3'2'}C_{3'1'}C_{32}C_{31}H_{3'}H_3C_{33'}C_{22'}C_{11'}, \qquad (8)$$

where H_i is a Hadamard transformation on the qubit i which sends $|0\rangle \longrightarrow (|0\rangle + |1\rangle)$ and $|1\rangle \longrightarrow (|0\rangle - |1\rangle)$; thus, we have

$$U_e(|\psi\rangle_{123}|000\rangle_{1'2'3'}) = |\psi\rangle_L. \qquad (9)$$

One can certainly envision situations where one might, in fact, know where the error has occurred (by using the methods for determining the position of an error [33]). Let us first consider the case in which qubit 1 undergoes decoherence. Because $|0\rangle$ and $|1\rangle$ form a basis for qubit 1, we need only know what happens to these two states. In general, the decoherence process must be

$$|e_0\rangle|0\rangle \longrightarrow |\epsilon_0\rangle|0\rangle + |\epsilon_1\rangle|1\rangle,$$
$$|e_0\rangle|1\rangle \longrightarrow |\epsilon_0'\rangle|0\rangle + |\epsilon_1'\rangle|1\rangle, \qquad (10)$$

where $|\epsilon_0\rangle$, $|\epsilon_1\rangle$, $|\epsilon_0'\rangle$, and $|\epsilon_1'\rangle$ are appropriate environment states, not necessarily orthogonal or normalized, and $|e_0\rangle$ is the initial state of the environment. As will be shown below, during the restoration operation, there is no need to perform any operations on qubit 1. For simplicity, we can rewrite Eq. (10) as

$$|e_0\rangle|0\rangle \longrightarrow |\tilde{0}\rangle,$$
$$|e_0\rangle|0\rangle \longrightarrow |\tilde{1}\rangle, \tag{11}$$

where the above environment states $|\epsilon_0\rangle$, $|\epsilon_1\rangle$, $|\epsilon_0'\rangle$, and $|\epsilon_1'\rangle$ have been included in $|\tilde{0}\rangle$ and $|\tilde{1}\rangle$. Let us now see what will happen to the encoded state $|\psi\rangle_L$. After decoherence, it goes to

$$|\psi\rangle_L \otimes |e_0\rangle = \alpha_0|\tilde{0}\rangle_L + \alpha_1|\tilde{1}\rangle_L + \alpha_2|\tilde{2}\rangle_L$$
$$+ \alpha_3|\tilde{3}\rangle_L + \alpha_4|\tilde{4}\rangle_L + \alpha_5|\tilde{5}\rangle_L + \alpha_6|\tilde{6}\rangle_L + \alpha_7|\tilde{7}\rangle_L, \tag{12}$$

where

$$|\tilde{0}\rangle_L = (|\tilde{0}00\rangle + |\tilde{1}11\rangle) \otimes (|000\rangle + |111\rangle),$$

$$|\tilde{1}\rangle_L = (|\tilde{0}00\rangle - |\tilde{1}11\rangle) \otimes (|000\rangle - |111\rangle),$$

$$|\tilde{2}\rangle_L = (|\tilde{0}10\rangle + |\tilde{1}01\rangle) \otimes (|010\rangle + |101\rangle),$$

$$|\tilde{3}\rangle_L = (|\tilde{0}10\rangle - |\tilde{1}01\rangle) \otimes (|010\rangle - |101\rangle), \tag{13}$$

$$|\tilde{4}\rangle_L = (|\tilde{1}00\rangle + |\tilde{0}11\rangle) \otimes (|100\rangle + |011\rangle),$$

$$|\tilde{5}\rangle_L = (|\tilde{1}00\rangle - |\tilde{0}11\rangle) \otimes (|100\rangle - |011\rangle),$$

$$|\tilde{6}\rangle_L = (|\tilde{1}10\rangle + |\tilde{0}01\rangle) \otimes (|110\rangle + |001\rangle),$$

$$|\tilde{7}\rangle_L = (|\tilde{1}10\rangle - |\tilde{0}01\rangle) \otimes (|110\rangle - |001\rangle).$$

Comparing Eqs. (13) with Eqs. (3), one can see that, for each bad logical state in (13), the right part of the product, which corresponds to the encoding of the three ancillary qubits, is intact. We can first perform a unitary transformation on the three ancillary qubits, which we regard as the partial decoding operation (since qubits 1, 2, and 3 are not involved in the decoding operation). The decoding operation is shown as follows:

$$U_d = H_{3'}C_{3'2'}C_{3'1'}. \tag{14}$$

After decoding, we have

$$|\tilde{0}\rangle_L \longrightarrow (|\tilde{0}00\rangle + |\tilde{1}11\rangle) \otimes |000\rangle,$$

$$|\tilde{1}\rangle_L \longrightarrow (|\tilde{0}00\rangle - |\tilde{1}11\rangle) \otimes |001\rangle,$$

$$|\tilde{2}\rangle_L \longrightarrow (|\tilde{0}10\rangle + |\tilde{1}01\rangle) \otimes |010\rangle,$$

$$|\tilde{3}\rangle_L \longrightarrow (|\tilde{0}10\rangle - |\tilde{1}01\rangle) \otimes |011\rangle, \tag{15}$$

$$|\tilde{4}\rangle_L \longrightarrow (|\tilde{1}00\rangle + |\tilde{0}11\rangle) \otimes |100\rangle,$$

$$|\tilde{5}\rangle_L \longrightarrow (|\tilde{1}00\rangle - |\tilde{0}11\rangle) \otimes |101\rangle,$$

$$|\tilde{6}\rangle_L \longrightarrow (|\tilde{1}10\rangle + |\tilde{0}01\rangle) \otimes |110\rangle,$$

$$|\tilde{7}\rangle_L \longrightarrow (|\tilde{1}10\rangle - |\tilde{0}01\rangle) \otimes |111\rangle,$$

What we need to do now is to perform an error recovery operation in order to extract the original state (1). It can be done by a unitary transformation on qubits 2, 3, 1', 2', and 3', which is described by

$$U_r = T_{1'3'2}Z_{3'2}T_{1'3'2}C_{2'2}C_{1'2}C_{1'3}, \tag{16}$$

where $T_{1'3'2}$ is a Toffoli gate operation [35] and $Z_{3'2}$ is a controlled Pauli σ_z operation. A Toffoli gate operation T_{ijk} has the two control bits corresponding to the first two subscripts (i, j) and the target bit k. When the two control bits are in the state $|11\rangle$, the state of the target bit will change, following $|0\rangle \longrightarrow |1\rangle$ and $|1\rangle \longrightarrow |0\rangle$, while when the two control bits are in the state $|00\rangle$, $|01\rangle$, or $|10\rangle$, the state of the target bit will be invariant. A controlled Pauli σ_z operation Z_{ij} has the control bit i and the target bit j, which sends the state of the target bit $|0\rangle \longrightarrow |0\rangle$ and $|1\rangle \longrightarrow -|1\rangle$ when the control bit is in the state $|1\rangle$; otherwise, when the control bit is in $|0\rangle$, the state of the target bit will not change. One can easily verify that, after the operation U_r, the system composed of the six qubits and the environment will be in the state

$$(|\tilde{0}00\rangle + |\tilde{1}11\rangle) \otimes |\psi\rangle_{1'2'3'}, \tag{17}$$

where

$$|\psi\rangle_{1'2'3'} = \alpha_0|000\rangle + \alpha_1|001\rangle + \alpha_2|010\rangle + \alpha_3|011\rangle$$
$$+ \alpha_4|100\rangle + \alpha_5|101\rangle + \alpha_6|110\rangle + \alpha_7|111\rangle. \tag{18}$$

From Eqs. (17), (18), one can see that the above restoration operation is actually a disentangling operation, which has made the three qubits 1', 2', and 3' no longer entangled with the remaining system (i.e., the three qubits 1, 2, and 3 and the environment). Even though the three qubits 1, 2, and 3 are entangled with the environment, the information, originally carried by qubits 1, 2, and 3, has been completely transferred into the three qubits 1', 2', and 3', and the original state (1) has been exactly reconstructed through the three qubits 1', 2', and 3'.

It is straightforward to extract the original state when the error occurs on qubit 2 or 3. To simplify our presentation, however, we will not give a detailed discussion. In the case of qubit 2 or qubit 3 going bad, the decoding operation is the same as above. If qubit 2 goes bad, the error recovery operation will be $T_{2'3'1}Z_{3'1}T_{2'3'1}C_{1'1}C_{2'1}C_{2'3}$, while when the qubit 3 goes bad, the error recovery operation is much simpler, i.e., $Z_{3'2}C_{2'2}C_{1'1}$. After performing the error recovery operations, the final state, corresponding to the case when the error occurs on qubit 2 or 3, will be

$$(|0\tilde{0}0\rangle + |1\tilde{1}1\rangle) \otimes |\psi\rangle_{1'2'3'}, \tag{19}$$

or

$$(|00\tilde{0}\rangle + |11\tilde{1}\rangle) \otimes |\psi\rangle_{1'2'3'}. \qquad (20)$$

Above, we discussed how to recover the original state when qubit 1, 2, or 3 undergoes decoherence. From Eq. (3), one can easily see that, for each logical state, qubits 1, 2, and 3 and qubits 1', 2', and 3' are in the same GHZ states, i.e., each logical state is a product of two copies of a three-qubit GHZ state. Thus, the decoding and error recovery operations for the case of qubit 1', 2', or 3' going bad are similar to those, respectively, for the case of qubit 1, 2, or 3 going bad. The only thing to be noted is that, when qubit 1', 2', or 3' goes bad, the subscripts (1', 2', 3', 1, 2, 3), which are involved in the above decoding and error-recovery unitary transformations, need to be permuted into (1, 2, 3, 1', 2', 3'), respectively. Thus, we have (a) when qubit 1', 2', or 3' goes bad, the decoding operation is given by $H_3 C_{32} C_{31}$; (b) for the case of qubit 1', 2', or 3' going bad, the error recovery operation is given by $T_{132'} Z_{32'} T_{132'} C_{22'} C_{12'} C_{13'}$, $T_{231'} Z_{31'} T_{231'} C_{11'} C_{21'} C_{23'}$, or $Z_{32'} C_{22'} C_{11'}$, respectively. After performing the decoding and error recovery operations, the original state will be restored through qubits 1, 2, and 3, while qubits 1', 2', and 3' are entangled with the environment.

It is interesting to note that the present code can also work when error happens out of qubit spaces. The above decoherence process (10), in fact, corresponds to the case when qubits are represented by ideal "two-state" or "two-level" systems. In most cases, physical systems (particles or solid-state devices) may have many levels, such as atoms, ions, and SQUIDs. If a qubit is represented by a two-dimensional (2D) subspace of the Hilbert space of a multilevel physical system, the interaction with environment may lead to the leakage out of the 2D qubit space (i.e., the space spanned by the two states $|0\rangle$ and $|1\rangle$ of a qubit). The decoherence process, therefore, is given by

$$|e_0\rangle|0\rangle \longrightarrow |\epsilon_0\rangle|0\rangle + |\epsilon_1\rangle|1\rangle + \sum_{i \neq 0, 1} |\epsilon_i\rangle|i\rangle,$$

$$|e_0\rangle|1\rangle \longrightarrow |\epsilon_0'\rangle|0\rangle + |\epsilon_1'\rangle|1\rangle + \sum_{i \neq 0, 1} |\epsilon_i'\rangle|i\rangle, \qquad (21)$$

where $\{|i\rangle\}$, together with $|0\rangle$ and $|1\rangle$, forms a complete orthogonal basis of a multilevel system and $|\epsilon_i\rangle$, $|\epsilon_i'\rangle$ are environment states. Note that, during the above restoration operation, there is no need to perform any operations on the bad qubit. Thus, for the case when a qubit is represented by a 2D subspace of a multilevel physical system and decoherence happens like (21), one can still protect an arbitrary state of three qubits against one erasure by using the code and following the restoration operations described above.

Finally, we note that, for some special types of three-qubit state, the protection against one erasure may be done by a code with a smaller number of qubits.

For example, one can show that the following three-qubit states

$$\alpha|001\rangle + \beta|010\rangle + \gamma|100\rangle \qquad (22)$$

(which, in the case of $|\alpha| = |\beta| = |\gamma| = 1/\sqrt{3}$, are called "entangled W states" [36], which have attracted much interest recently) can be protected against one erasure through the following five-qubit code:

$$|001\rangle \longrightarrow |00001\rangle + |11110\rangle,$$

$$|010\rangle \longrightarrow |00100\rangle + |11011\rangle, \qquad (23)$$

$$|100\rangle \longrightarrow |00010\rangle + |11101\rangle.$$

The present code may have some application in protecting a few qubits of quantum information against decoherence. It is presumed that the first prototype quantum computer will be small and quantum information will be stored through only a few qubits. Moreover, there is much interest arising from a quantum computing network which is based on the connection of locally distinct nodes each carrying out a small-scale quantum computation [37]. In addition, as noted in [33], quantum erasure-correcting codes may be applied in *fault tolerant quantum computing*, which was proposed by Shor and permits one to perform quantum computation and error correction with a network of erroneous quantum gates [38]. Thus, the present code may also be useful in a small-scale *fault tolerant* quantum computation or in the demonstration of quantum algorithm of a few qubits. Finally, since the bad qubit is not involved in the above restoration operation (i.e., it does not contain any information, so that it can be "thrown away" without affecting the recovery of the original message), the code is also one for hiding three qubits of quantum information over each qubit. Therefore, the present code may have some other applications in quantum information processing and quantum communication, such as quantum secret sharing [39] and quantum cryptography [40].

In summary, we have proposed a small code for protecting three-qubit quantum information against one erasure. As shown above, the encoding, decoding, and error-recovery operations presented here are straightforward. We believe that the present code is of some interest, especially because of its high encoding efficiency, i.e., only one ancillary qubit being required for one "message" qubit on average, and because of its usefulness in a worse case that the interaction with the environment leads to a leakage out of the qubit space.

REFERENCES

1. P. W. Shor, in *Proceedings of 35th Annual Symposium on Foundations of Computer Science* (IEEE Computer Society Press, New York, 1994), p. 124.

2. I. L. Chuang, R. Laflamme, P. W. Shor, and W. H. Zurek, Science **270**, 1633 (1995).

3. D. Deutsch, Proc. R. Soc. London, Ser. A **400**, 97 (1985); **425**, 73 (1989).

4. L. K. Grover, Phys. Rev. Lett. **79**, 325 (1997).

5. P. W. Shor, Phys. Rev. A **52**, R2493 (1995).

6. A. M. Steane, Phys. Rev. Lett. **77**, 793 (1996).

7. R. Laflamme, C. Miquel, J. P. Paz, and W. H. Zurek, Phys. Rev. Lett. **77**, 198 (1996).

8. A. Ekert and C. Macchiavello, Phys. Rev. Lett. **77**, 2585 (1996).

9. D. Gottesman, Phys. Rev. A **54**, 1862 (1996).

10. C. H. Bennett, D. P. DiVincenzo, J. A. Smolin, and W. K. Wootters, Phys. Rev. A **54**, 3824 (1996).

11. A. M. Steane, Phys. Rev. A **54**, 4741 (1996); Proc. R. Soc. London, Ser. A **452**, 2551 (1996).

12. P. W. Shor, quant-ph/9605011; P. Shor and R. Laflamme, Phys. Rev. Lett. **78**, 1600 (1997).

13. D. P. DiVincenzo and P. W. Shor, Phys. Rev. Lett. **77**, 3260 (1996).

14. W. H. Zurek and R. Laflamme, Phys. Rev. Lett. **77**, 4683 (1996).

15. M. B. Plenio, V. Vedral, and P. L. Knight, Phys. Rev. A **55**, 67 (1997).

16. A. R. Calderbank, E. M. Rains, P. W. Shor, and N. J. A. Sloane, Phys. Rev. Lett. **78**, 405 (1997).

17. E. Knill and R. Laflamme, Phys. Rev. A **55**, 900 (1997).

18. D. W. Leung, M. A. Nielsen, I. L. Chuang, and Y. Yamamoto, Phys. Rev. A **56**, 2567 (1997).

19. J. Preskill, quant-ph/9705031.

20. C. H. Bennett and P. W. Shor, IEEE Trans. Inf. Theory **44**, 2724 (1998).

21. L. Vaidman, L. Goldenberg, and S. Wiesner, Phys. Rev. A **54**, R1745 (1996).

22. L. M. Duan and G. C. Guo, Phys. Rev. A **57**, 2399 (1998).

23. L. M. Duan and G. C. Guo, Phys. Rev. Lett. **79**, 1953 (1997).

24. P. Zanardi and M. Rasetti, Phys. Rev. Lett. **79**, 3306 (1997); P. Zanardi, Phys. Rev. A **57**, 3276 (1998).

25. D. A. Lidar, D. Bacon, and K. B. Whaley, Phys. Rev. Lett. **82**, 4556 (1999); D. A. Lidar, I. L. Chuang, and K. B. Whaley, Phys. Rev. Lett. **81**, 2594 (1998).

26. L. Viola and S. Lloyd, Phys. Rev. A **58**, 2733 (1998); L. Viola, E. Knill, and S. Lloyd, Phys. Rev. Lett. **82**, 2417 (1999); L. Viola, S. Lloyd, and E. Knill, Phys. Rev. Lett. **83**, 4888 (1999).

27. D. Vitali and P. Tombesi, Phys. Rev. A **59**, 4178 (1999).

28. G. S. Agarwal, Phys. Rev. A **61**, 013809 (2000).

29. E. Knill, R. Laflamme, and L. Viola, Phys. Rev. Lett. **84**, 2525 (2000); L. Viola, E. Knill, and S. Lloyd, Phys. Rev. Lett. **85**, 3520 (2000).

30. S. De Filippo, Phys. Rev. A **62**, 052307 (2000).

31. P. Zanardi, Phys. Rev. A **63**, 12301 (2001).

32. C. P. Yang and J. Gea-Banacloche, Phys. Rev. A **63**, 022311 (2001).

33. M. Grassl, Th. Beth, and T. Pellizzari, Phys. Rev. A **56**, 33 (1997).

34. N. J. Cerf and R. Cleve, Phys. Rev. A **56**, 1721 (1997).

35. M. A. Nielsen and I. L. Chuang, *Quantum Computation and Quantum Information* (Cambridge Univ. Press, Cambridge, 2001).

36. W. Dür, G. Vidal, and J. I. Cirac, Phys. Rev. A **62**, 062314 (2000).

37. T. Pellizzari, Phys. Rev. Lett. **79**, 5242 (1997).

38. P. W. Shor, in *Proceedings of the 37th Symposium on Foundations of Computer Science* (IEEE, Los Alamitos, 1996), p. 56.

39. M. Hillery, V. Buzek, and A. Berthiaume, Phys. Rev. A **59**, 1829 (1999).

40. C. H. Bennett and G. Brassard, in *Proceedings of IEEE International Conference on Computers, Systems, and Signal Processing, Bangalore, India* (IEEE, New York, 1984); C. H. Bennett, G. Brassard, and N. D. Mermin, Phys. Rev. Lett. **68**, 557 (1992).